Cell

Article

The immunoproteasome disturbs neuronal metabolism and drives neurodegeneration in multiple sclerosis

Graphical abstract

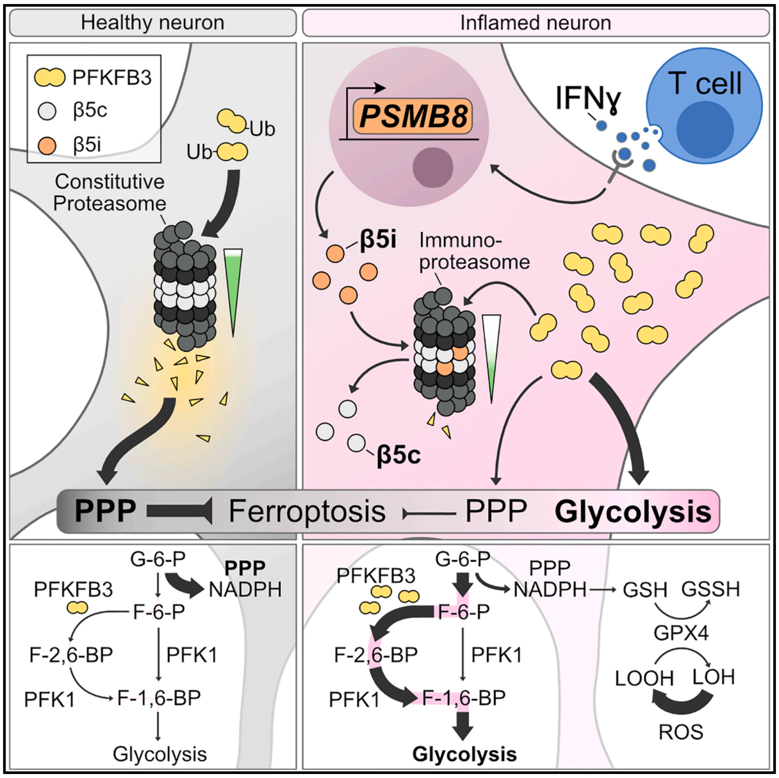

Highlights

- PSMB8 is induced in neurons under inflammatory conditions, such as multiple sclerosis
- The integration of PSMB8 into the proteasome reduces proteasome activity in neurons
- This causes the accumulation of PFKFB3, triggering a metabolic switch and ferroptosis
- Targeting PSMB8 or its downstream pathways provides neuroprotection *in vivo*

Authors

Marcel S. Woo, Johannes Brand, Lukas C. Bal, ..., Doron Merkler, Catherine Meyer-Schwesinger, Manuel A. Friese

Correspondence

manuel.friese@zmnh.uni-hamburg.de

In brief

Neuronal proteasomal dysfunction is a hallmark of neuroinflammatory and neurodegenerative diseases. This study reveals that the interferon-induced immunoproteasome drastically decreases proteasomal activity in neurons, leading to a switch in neuronal metabolism with increased oxidative injury and ferroptosis.

Woo et al., 2025, Cell *188*, 4567–4585
August 21, 2025 © 2025 The Authors. Published by Elsevier Inc.
https://doi.org/10.1016/j.cell.2025.05.029

CellPress

Cell

CellPress
OPEN ACCESS

Article

The immunoproteasome disturbs neuronal metabolism and drives neurodegeneration in multiple sclerosis

Marcel S. Woo,[1] Johannes Brand,[2] Lukas C. Bal,[1] Manuela Moritz,[3] Mark Walkenhorst,[1] Vanessa Vieira,[1] Inbal Ipenberg,[1] Nicola Rothammer,[1] Man Wang,[2] Batuhan Dogan,[2] Desirée Loreth,[2] Christina Mayer,[1] Darwin Nagel,[1] Ingrid Wagner,[4] Lena Kristina Pfeffer,[1] Peter Landgraf,[5] Marco van Ham,[6] Kuno M.-J. Mattern,[1] Ingo Winschel,[1] Noah Frantz,[7] Jana K. Sonner,[1] Henrike K. Grosshans,[1] Albert Miguela,[1,8] Simone Bauer,[1] Nina Meurs,[1] Anke Müller,[5] Lars Binkle-Ladisch,[1] Gabriela Salinas,[9] Lothar Jänsch,[6] Daniela C. Dieterich,[5]

(Author list continued on next page)

[1]Institute of Neuroimmunology and Multiple Sclerosis, University Medical Center Hamburg-Eppendorf, Hamburg, Germany
[2]Institute of Cellular and Integrative Physiology, University Medical Center Hamburg-Eppendorf, Hamburg, Germany
[3]Section/Core Facility Mass Spectrometry and Proteomics, Center for Diagnostics, University Medical Center Hamburg-Eppendorf, Hamburg, Germany
[4]Department of Pathology and Immunology, Division of Clinical Pathology, Faculty of Medicine, University and University Hospital of Geneva, Geneva, Switzerland
[5]Institute for Pharmacology and Toxicology, Medical Faculty, Otto-von-Guericke University Magdeburg, Magdeburg, Germany
[6]Cellular Proteome Research Group, Helmholtz Centre for Infection Research, Braunschweig, Germany
[7]Center of Hybrid Nanostructures, University of Hamburg, Hamburg, Germany
[8]Neurodegeneration and Neuroinflammation Group, Girona Biomedical Research Institute (IDIBGI), Girona, Spain
[9]NGS Integrative Genomics Core Unit, University Medical Center Göttingen, Göttingen, Germany
[10]Technology Platform Mass Spectrometry, University of Hamburg, Hamburg, Germany
[11]Institute of Medical Biochemistry and Molecular Biology, University Medicine Greifswald, Greifswald, Germany
[12]Department of Neuropathology, Charité – Universitätsmedizin Berlin, Freie Universität Berlin and Humboldt-Universität zu Berlin, Berlin, Germany
[13]Cluster of Excellence, NeuroCure, Charitéplatz 1, Berlin, Germany
[14]German Center for Neurodegenerative Diseases (DZNE), Berlin, Germany
[15]Institute of Neuropathology, University Medical Center Hamburg-Eppendorf, Hamburg, Germany
[16]III. Department of Medicine, University Medical Center Hamburg-Eppendorf, Hamburg, Germany
[17]Hamburg Center for Kidney Health (HCKH), University Medical Center Hamburg-Eppendorf, Hamburg, Germany

(Affiliations continued on next page)

SUMMARY

Inflammation, aberrant proteostasis, and energy depletion are hallmarks of neurodegenerative diseases such as multiple sclerosis (MS). However, the interplay between inflammation, proteasomal dysfunction in neurons, and its consequences for neuronal integrity remains unclear. Using transcriptional, proteomic, and functional analyses of proteasomal subunits in inflamed neurons, we found that interferon-γ-mediated induction of the immunoproteasome subunit, proteasome 20S beta 8 (PSMB8) impairs the proteasomal balance, resulting in reduced proteasome activity. This reduction causes the accumulation of phosphofructo-2-kinase/fructose-2,6-bisphosphatase 3 (PFKFB3), a key metabolic regulator, leading to enhanced neuronal glycolysis, reduced pentose phosphate pathway activity, oxidative injury, and ferroptosis. Neuron-specific genetic and systemic pharmacological targeting of PSMB8 or PFKFB3 protected neurons *in vitro* and in a mouse model of MS. Our findings provide a unifying explanation for proteasomal dysfunction in MS and possibly other neurodegenerative diseases, linking inflammation to metabolic disruption, and presenting an opportunity for targeted neuroprotective therapies.

INTRODUCTION

Multiple sclerosis (MS) is the most frequent inflammatory and neurodegenerative disease of the central nervous system (CNS) affecting young adults. It is thought to be driven by autoreactive T cells that infiltrate the CNS, initiating persistent low-grade inflammation that leads to progressive neurodegeneration.[1,2] While this interplay between inflammation and neurodegeneration is paradigmatic in MS, neuroinflammation is also a hallmark of other neurodegenerative diseases (NDDs) and aging.[3,4] Biomarker and

Cell *188*, 4567–4585, August 21, 2025

Maria Riedner,[10] Elke Krüger,[11] Frank L. Heppner,[12,13,14] Markus Glatzel,[15] Victor G. Puelles,[16,17,18,19] Jan Broder Engler,[1] Jens Randel Nyengaard,[19,20] Thomas Misgeld,[21,22,23] Martin Kerschensteiner,[23,24,25] Doron Merkler,[4] Catherine Meyer-Schwesinger,[2,26] and Manuel A. Friese[1,26,27,*]

[18]Department of Clinical Medicine, Aarhus University, Aarhus, Denmark
[19]Department of Pathology, Aarhus University Hospital, Aarhus, Denmark
[20]Core Center for Molecular Morphology, Department of Clinical Medicine, Aarhus University, Aarhus, Denmark
[21]Institute of Neuronal Cell Biology, Technical University of Munich, Munich, Germany
[22]German Center for Neurodegenerative Diseases (DZNE), Munich, Germany
[23]Munich Cluster of Systems Neurology (SyNergy), Munich, Germany
[24]Institute of Clinical Neuroimmunology, University Hospital, Ludwig-Maximilians-Universität München, Munich, Germany
[25]Biomedical Center, Medical Faculty, Ludwig-Maximilians-Universität München, Munich, Germany
[26]These authors contributed equally
[27]Lead contact
*Correspondence: manuel.friese@zmnh.uni-hamburg.de
https://doi.org/10.1016/j.cell.2025.05.029

imaging studies show that neuroinflammation arises early in various NDDs, even before symptoms appear.[5–7] In particular, the interferon (IFN)γ-mediated type II IFN response exacerbates neurodegeneration in models of MS,[8] viral encephalitis,[9] Alzheimer's disease (AD),[10] Parkinson's disease (PD),[11] and aging.[12] Although immunomodulatory therapies suppress the peripheral immune system in MS[2] and are being explored in other NDDs,[13] no treatments specifically target CNS-intrinsic inflammation or enhance neuronal resilience to inflammatory stress.

In addition to persistent neuroinflammation, MS shares several neuronal features with other NDDs and aging,[3,4] including glutamate excitotoxicity[14] and intracellular accumulation of neuron-specific proteins.[3,15] During CNS inflammation, neurons also suffer from energy depeletion,[16] which can activate cell death pathways[17–19] and contributes to neurodegeneration. In the MS model, experimental autoimmune encephalomyelitis (EAE), energy depletion partly results from impaired mitochondrial transport in axons.[20] However, recent studies show that sustained glycolysis also impairs neuronal function.[21,22] Unlike dividing cells, neurons rely on the proteasome to continuously degrade phosphofructo-2-kinase/fructose-2,6-bisphosphatase 3 (PFKFB3),[23] a key glycolytic regulator. This degradation suppresses glycolysis while favoring the pentose phosphate pathway (PPP), which supports antioxidative defenses. Proteasomal dysfunction or glutamate excitotoxicity stabilizes PFKFB3 and thereby increases glycolysis in neurons.[24,25] Additionally, defective proteasomes can result in the accumulation of enzymes or signaling molecules,[26] such as PFKFB3, that are normally degraded. Inflammation further alters proteasome isoforms, particularly by inducing the immunoproteasome. This raises the possibility that inflammation-induced proteasomal alterations may contribute to metabolic dysregulation.

Neurons depend on tight protein homeostasis (proteostasis) due to their long lifespan, complex architecture, and specialized protein demands. The proteasome includes a 20S core with proteolytically active β subunits and a 19S regulatory particle.[27] Under basal conditions, the 20S core particle comprises subunits β5c (proteasome 20S beta [PSMB]5), β2c (PSMB7), and β1c (PSMB6). Upon IFNγ signaling, these subunits can be replaced by immunoproteasome subunits β5i (PSMB8), β2i (PSMB10), and β1i (PSMB9).[27] While this replacement occurs in many cell types, immune and endothelial cells constitutively express the immunoproteasome[28,29] to present an extended repertoire of major histocompatibility complex (MHC) class I epitopes. Additionally, its induction leads to higher proteasomal activity in these dividing cells.[28,29] Accordingly, global *Psmb8* deficiency impairs immune responses. Similarly, the immunoproteasome is essential for maintaining proteostasis in fibroblasts, astrocytes and microglia under inflammatory conditions, with its absence leading to increased oxidative stress.[30–32] Although IFNγ induces a neuronal inflammatory stress response (NISR) that regulates redox homeostasis during CNS inflammation,[8] the inflammation-induced changes of the ubiquitin-proteasome system (UPS) and proteasomal activity in neurons remain poorly understood. Given the post-mitotic and specialized nature, neurons may use the immunoproteasome differently, as suggested by unique roles of the 19S regulatory particle in synaptic receptor recycling.[33]

Understanding how proteasome regulation changes during the NISR could reveal neuroprotective strategies. Here, we used neuron-specific transcriptional and proteomic profiling as well as proteasome activity analyses in EAE and cultured neurons to show that IFNγ-induced PSMB8 reduces proteasomal activity, drives metabolic reprogramming, and leads to neuronal damage. These findings provide a framework for targeting inflammation-induced proteostasis disruption with pharmacological interventions that could protect neurons in MS and other NDDs.

RESULTS

PSMB8 is expressed in inflamed neurons

To explore inflammation-induced changes of the neuronal proteasome, we examined the neuronal transcriptional regulation of proteasomal subunits during CNS inflammation. We used the EAE model in C57BL/6 mice, characterized by CNS-infiltrating immune cells that trigger a cascade of glia and myeloid-cell-driven inflammation and neurodegeneration.[34–36] RNA sequencing of spinal cord neuronal nuclei revealed significant induction of immunoproteasome subunits *Psmb8* and *Psmb9* during acute EAE (Figures 1A and S1A).

To confirm protein expression, we crossed neuron-specific *Snap25*-Cre mice with *LSL-R26-MetRS**,[37] mice, enabling *in vivo* labeling of neuronal proteins during EAE. Analysis of the neuronal

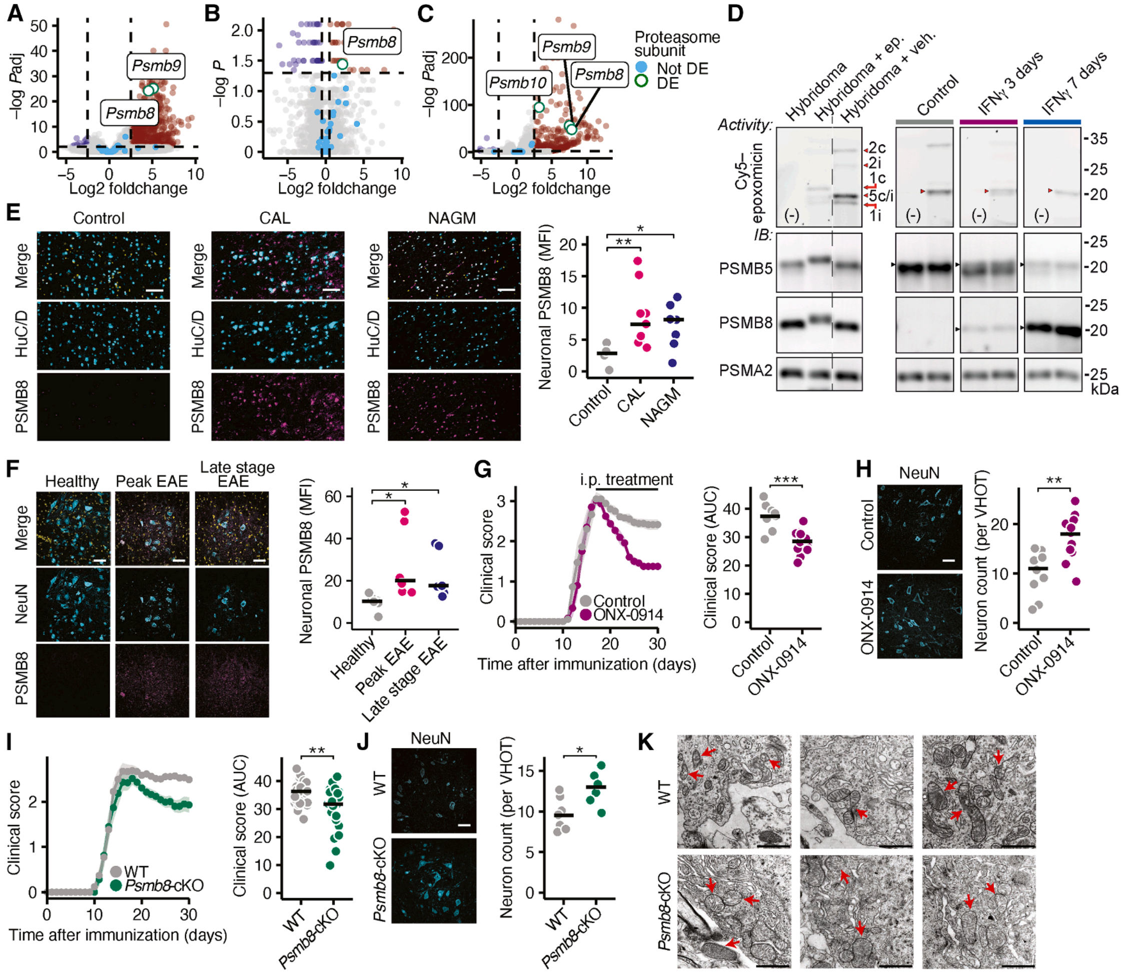

Figure 1. The immunoproteasome accelerates inflammation-induced neurodegeneration

(A) Volcano plot of genes detected by RNA sequencing of neuronal nuclei in healthy and peak EAE mice, (15 days post-immunization [p.i.]; $n = 5$). Differentially expressed (DE) genes with $\log_2$ fold change > 2 or < −2 and a false discovery rate [FDR]-adjusted p value < 0.05 are labeled in red or blue, respectively. DE and non-regulated proteasomal subunits are labeled separately.

(B) Volcano plot of proteins detected by neuron-specific proteomics in *Snap25*-Cre × LSL-R26-MetRS* healthy and peak EAE mice (15 days p.i.; $n = 5$). Differentially abundant proteins with a $\log_2$ fold change > 0.5 or < −0.5 and a p value < 0.05 are labeled in red or blue, respectively. DE and non-regulated proteasomal subunits are labeled separately.

(C) Volcano plot of genes detected by RNA sequencing of neuronal cultures exposed to IFNγ for 7 days or control neurons ($n = 6$). DE genes with a $\log_2$ fold change > 2 or < −2 and an FDR-adjusted p value < 0.05 are labeled in red or blue, respectively. DE and non-regulated proteasomal subunits are labeled separately.

(D) Proteasomal subunit activity in unstimulated neurons (control), neurons stimulated with 100 ng mL^{-1} IFNγ for 3 or 7 days. A lane without activity probe served as negative control (labeled with "(–)"). Hybridoma cells, either untreated (veh.) or treated with the proteasome inhibitor epoxomicin (ep.) were used as positive or negative controls, respectively, for the different catalytic β subunits separated by size. Representative activities and the corresponding immunoblots (IBs) of PSMB5, PSMB8, and PSMA2 as 20S loading control under all conditions are shown. Red arrowheads indicate PSMB5/PSMB8 activity, black arrowheads the respective proteins. In total four replicates were performed; the statistical analysis is provided in Figure S1D.

(E) Mean fluorescence intensity (MFI) of PSMB8 per neuron, visualized by HuC/D, in postmortem cortices of controls ($n = 4$), chronic active lesions (CALs) of people with relapsing MS ($n = 10$), and normal-appearing gray matter (NAGM) of people with progressive MS ($n = 7$). DAPI was stained to visualize nuclei (yellow). Scale bar, 200 μm.

(F) MFI of neuronal PSMB8 in the spinal cord ventral horn outflow tract (VHOT) of healthy ($n = 5$), peak EAE (15 days p.i.; $n = 6$), and late-stage EAE (30 days p.i.; $n = 7$) mice. DAPI (yellow) was used to stain nuclei. Scale bar, 50 μm.

(G) EAE disease course in mice treated daily with either vehicle ($n = 9$) or 10 mg kg^{-1} body weight ONX-0914 ($n = 12$) intraperitoneally (i.p.) starting at the acute EAE stage (14 days p.i.). A Mann-Whitney U test was performed on the area under the curve (AUC) during the peak and chronic disease stage (15–30 days p.i.) for statistical comparisons.

(H) Quantification of neuron counts in the spinal cord VHOT of late-stage EAE mice (30 days p.i.) treated with vehicle ($n = 9$) or 10 mg kg^{-1} body weight ONX-0914 ($n = 11$) i.p. Scale bar, 50 μm.

(I) EAE disease course of wild-type (WT; $n = 34$) and neuron-specific *Psmb8* knockout (*Psmb8*-cKO; $n = 24$) EAE mice. A Mann-Whitney U test was performed on the AUC during the peak and chronic disease stage (15–30 days p.i.) for statistical comparison.

(legend continued on next page)

proteome (Figures S1B and S1C) during acute EAE revealed a significant upregulation of PSMB8, but not PSMB9 (Figure 1B). Transcriptional profiling of IFNγ-exposed neuronal cultures also confirmed immunoproteasome subunit induction (Figure 1C).

To address whether expression changes result in altered proteasomal activity, we used the pan-proteasome-activity-based probe Cy5-epoxomicin.[38] At baseline, neurons showed prominent β5c (PSMB5) and modest β2c (PSMB7) activity, without detectable β5i (PSMB8) protein expression (Figure 1D). However, IFNγ exposure increased β5i (PSMB8) protein levels and reduced β5c (PSMB5). In contrast, β1i (PSMB9) activity remained undetectable, supporting that PSMB8 is the primary immunoproteasome subunit induced in inflamed neurons. Despite higher PSMB8 protein, the specific activity of β5c/β5i decreased (Figures 1D and S1D), implicating these proteasome subunits as key modulators of neuronal catalytic activity.

Next, we sought to confirm the induction of PSMB8 in people with MS (pwMS). Immunohistochemistry performed on brain biopsies (Figure S1E) and autopsies (Figure 1E) from pwMS revealed that PSMB8 was expressed in neurons of active cortical lesions and normal-appearing gray matter, but not in control tissue. Similarly, we detected neuronal PSMB8 expression in peak and late-stage C57BL/6 EAE mice, but not in healthy control mice (Figure 1F). Confirming that this is a general neuronal response pattern across different MS models, we detected neuronal PSMB8 expression during EAE relapses in SJL mice (Figure S1F), a model of relapsing-remitting MS, as well as during acute and late-stage EAE in Biozzi ABH mice, a model of progressive MS (Figure S1G). In contrast, neuronal PSMB5 levels remained unchanged during C57BL/6 EAE (Figure S1D). In the same model, PSMB8 expression was higher in spinal cord neurons of late-stage EAE mice with progressive disease compared with those that recovered (Figures S1H and S1I). This was associated with elevated IFNγ levels (Figure S1J), increased T cell infiltration (Figure S1K), and more IFNγ$^+$ CD8$^+$ T cells (Figure S1L). Consistent with the increased expression of *Psmb8* in non-neuronal nuclei in peak EAE mice (Figure S1M), we detected elevated PSMB8 protein levels also in astrocytes, microglia, Quaking 7 protein (CC1)+ (pre-)myelinating oligodendrocytes, nerve/glial-antigen 2 (NG2)+ oligodendrocyte precursor cells, and endothelial cells, followed by a subsequent reduction in late-stage EAE mice (Figure S1N). These findings suggest persistent neuronal PSMB8 expression during EAE and MS, potentially contributing to inflammation-induced neurodegeneration.

Neuronal PSMB8 drives neurodegeneration in EAE

To test the hypothesis that neuronal PSMB8 is involved in neurodegeneration, we treated EAE mice by daily intraperitoneal (i.p.) injections of the immunoproteasome inhibitor ONX-0914,[39] starting from the acute EAE stage. This treatment reduced EAE disease severity (Figures 1G and S2A) and protected against neuronal loss (Figure 1H), synaptic loss in the spinal cord ventral horn (but not in the dorsal horns), and reduced axonal degeneration in dorsal columns (Figures S2B–S2D). Given that systemically applied ONX-0914 exerts immunomodulatory effects,[39,40] we generated neuron-specific *Psmb8* conditional knockout mice (*Psmb8*-cKO) by crossing *Snap25*-Cre with *Psmb8*-flox mice (Figure S2E). This did not affect neuronal and axonal counts or proteasome function, as measured by K48-linked ubiquitin levels in healthy mice (Figures S2F–S2H). However, during EAE, neuronal *Psmb8* deletion reduced disease severity (Figures 1I and S2I) and protected against neuronal loss (Figure 1J), preserved synapses in the spinal cord ventral horns, and axons in the dorsal columns (Figures S2J–S2L), and reduced mitochondrial injury, as assessed by ultrastructural evaluation of cristae loss and disorganization[41–43] (Figure 1K). Myelin pathology remained unaffected (Figures S2M and S2N).

This result was unexpected, as PSMB8 is essential for maintaining redox balance in proliferating cells and microglia.[30,31] Since *Psmb8* deficiency in peripheral immune cells and endothelial cells affects MHC class I expression and immune activation, we investigated whether this was altered in *Psmb8*-cKO mice. However, we found no differences in neuronal MHC class I expression during EAE (Figures S2O and S2P) and observed no changes in CNS-infiltrating T cells during acute and chronic EAE, including interleukin (IL)-17 and IFNγ-producing T cells. Additionally, there were no differences in microglia activation (Figure S3). These findings suggest that PSMB8 plays a distinct role in neurons and increases their intrinsic vulnerability to chronic inflammation.

Continuous PSMB8 expression is neurotoxic

To test whether PSMB8 affects neuronal viability, we overexpressed PSMB5, PSMB8, or an mScarlet control construct in neurons (Figure 2A). Further, we induced endogenous PSMB8 expression by exposing neurons to IFNγ for 3 or 7 days (Figure 2B). This resulted in a gradual increase of PSMB8 protein abundance, which was accompanied by a decrease in PSMB5 levels (Figure 2B), demonstrating that PSMB5 is replaced by PSMB8 in IFNγ-exposed neurons. This was further confirmed by identifying a decreased PSMB5 and increased PSMB8 incorporation into the 20S and 26S proteasome cores (Figures S4A–S4H). Of note, IFNα stimulation over 7 days also increased neuronal PSMB8 expression and decreased PSMB5 expression, while IL-17, tumor necrosis factor alpha (TNF-α), granulocyte macrophage colony-stimulating factor (GM-CSF), IL-1β, and glutamate did not affect PSMB8 or PSMB5 levels (Figure S4I).

After 21 days, PSMB8 overexpression, but not PSMB5, led to pronounced neuronal death (Figures 2C, S4J, and S4K), which was rescued by co-expressing PSMB5 (Figure 2C),

---

(J) Quantification of neuron counts in the spinal cord VHOT of WT ($n = 7$) and *Psmb8*-cKO ($n = 6$) late-stage EAE mice (30 days p.i.). Scale bar, 50 μm.
(K) Transmission electron microscopy images of spinal cord neurons from WT ($n = 3$) and *Psmb8*-cKO ($n = 3$) mice during peak EAE (15 days p.i.). Mitochondria are highlighted by the indicated arrows. Scale bar, 1 μm.
For (E) and (F), a one-way ANOVA with post hoc Tukey's HSD tests was used. For (G)–(J), a Mann-Whitney U test was used. Individual data points and means are shown. $^*p < 0.05$, $^{**}p < 0.01$, $^{***}p < 0.001$, $^{****}p < 0.0001$.
See also Figures S1–S3 and S12.

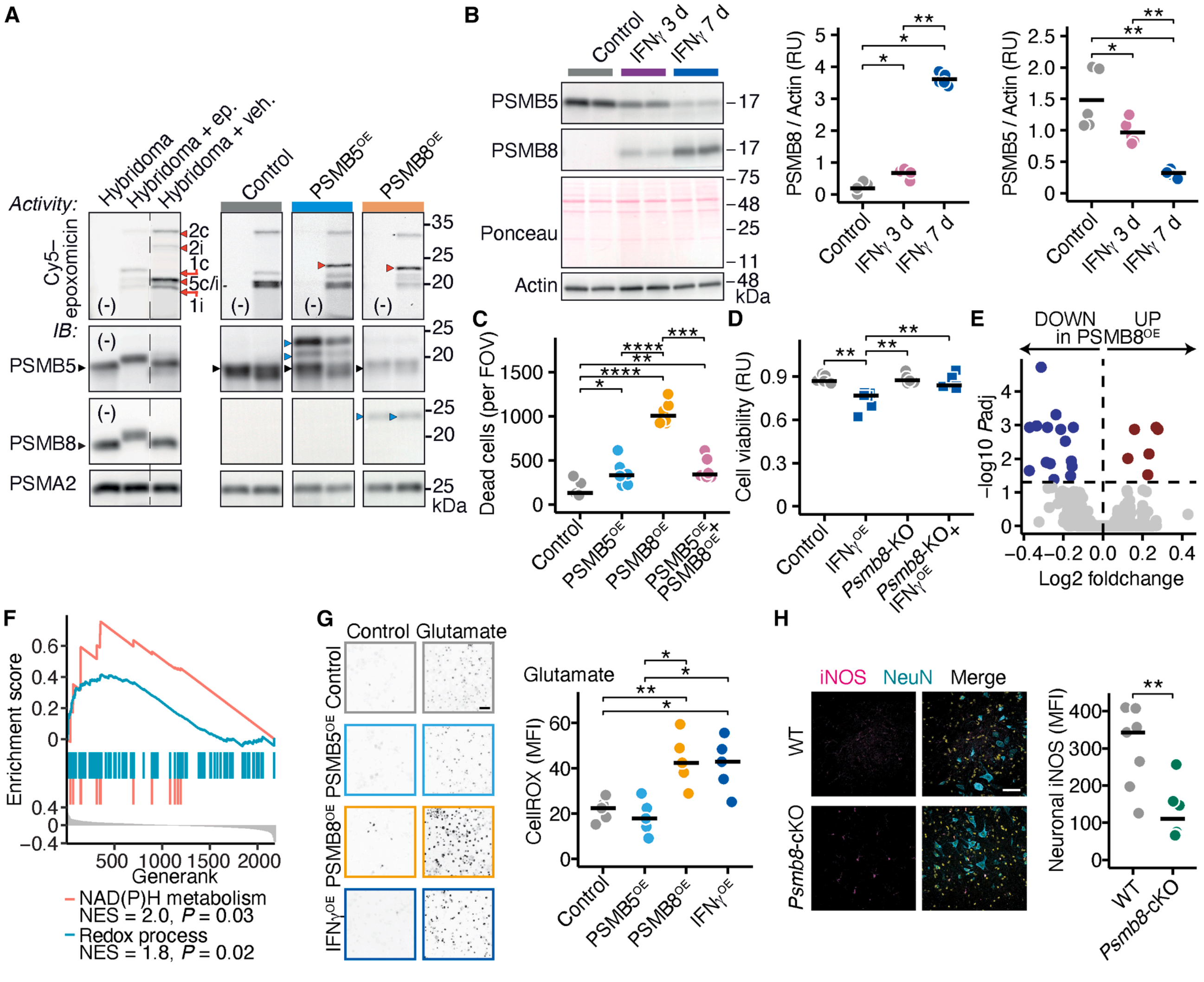

Figure 2. Continuous PSMB8 expression is neurotoxic

(A) Proteasomal subunit activity in neurons overexpressing mScarlet (control), PSMB5 (PSMB5^{OE}), or PSMB8 (PSMB8^{OE}). One lane without the activity probe was used as a negative control (labeled with “(–)”). Hybridoma cells, either untreated (veh.) or treated with the proteasome inhibitor epoxomicin, (ep.) served as positive and negative controls, respectively. Immunoblots (IBs) of PSMB5, PSMB8, and PSMA2 (proteasome loading control) corresponding to the activity gels across all conditions are shown. A red arrowhead marks the activity band of the overexpression constructs. In the PSMB5 IB, a black arrowhead indicates endogenous PSMB5, while blue arrowheads indicate size shift of endogenous/exogenous PSMB5 due to activity-based probe binding. In the PSMB8 IB, blue arrowheads denote a size shift of exogenous PSMB8 due to activity-based probe binding. In total 4 replicates were performed.

(B) Immunoblot analyses of PSMB5, PSMB8, actin and Ponceau staining as a loading control in neuronal cultures stimulated with 100 ng mL^{-1} IFNγ for 3 or 7 days ($n = 6$). Protein levels were normalized to actin for quantification as relative units (RUs). Band sizes are indicated in kDa.

(C) Number of dead cells per field of view (FOV) of neurons overexpressing mScarlet (control), PSMB5 (PSMB5^{OE}), PSMB8 (PSMB8^{OE}), or both for 21 days ($n = 6$). Representative images are shown in Figure S12H.

(D) Cell viability (RU) of mScarlet control neurons or chronically IFNγ-exposed (IFNγ^{OE}) WT and *Psmb8*-KO neurons exposed to 50 μM glutamate for 15 h ($n = 6$).

(E) Volcano plot visualization of differential expression analysis of mScarlet control and PSMB8^{OE} neurons. The horizontal dashed line represents an FDR-adjusted p value of 0.05 ($n = 5$).

(F) Enrichment analysis of the indicated gene ontology terms in the sequencing data of PSMB8^{OE} and mScarlet control neurons. Adjusted p values and normalized enrichment scores (NESs) are shown in the figure.

(G) Reactive oxygen species (ROS) in neurons overexpressing PSMB5^{OE}, PSMB8^{OE}, or IFNγ^{OE}, measured by CellROX, following treatment with 50 μM glutamate for 2 h ($n = 5$). Scale bar, 50 μm.

(H) Neuronal MFI of the inducible nitric oxide synthase (iNOS, turquoise) in the spinal cord VHOTs of WT ($n = 7$) and *Psmb8*-cKO ($n = 5$) EAE mice during late stage (30 days p.i.). Nuclei were visualized with DAPI (yellow). Scale bar, 50 μm. An unpaired t test was used.

For (B)–(D) and (G), a one-way ANOVA with post hoc Tukey’s honestly significant difference (HSD) tests was used. Individual data points and the means are shown. *$p < 0.05$, **$p < 0.01$, ***$p < 0.001$, ****$p < 0.0001$.

See also Figures S4 and S12.

underscoring the competitive incorporation into the proteasome. Since PSMB8 is induced by IFNγ and continuous IFNγ exposure renders neurons more susceptible to excitotoxicity,[8] we next investigated whether the proteasomal switch mediates this vulnerability. Indeed, genetic deletion of *Psmb8* (Figure 2D) prevented IFNγ-mediated (IFNγ^{OE}) vulnerability to glutamate excitotoxicity. In contrast, *Psmb8*-KO neurons were not protected from excitotoxicity in the absence of IFNγ exposure (Figure 2D).

To explore the mechanism behind PSMB8-mediated neuronal toxicity, we performed mRNA sequencing of control mScarlet-, PSMB5-, and PSMB8-overexpressing neurons at a time point when no differences in toxicity were observed (7 days of overexpression). In comparison with controls, we detected differentially expressed genes in PSMB8, but not in PSMB5-overexpressing neurons (Figures 2E and S4L). PSMB8-overexpressing neurons expressed fewer gene transcripts related to synaptic potentiation or plasticity, which aligns with its neurotoxic effects (Figure S4M), and induced gene transcripts related to redox balance and metabolic co-enzymes (Figure 2F).

To validate that PSMB8 alters neuronal redox balance, we measured reactive oxygen species (ROS) at baseline and after glutamate stimulation. We observed higher ROS levels in PSMB8, but not PSMB5-overexpressing neurons compared with controls, as well as a stronger excitotoxicity-induced ROS production (Figures 2G and S4N). In line with this, neuronal expression of the inducible nitric oxide synthase (iNOS), a marker for ROS production, was reduced in *Psmb8*-cKO mice during EAE (Figure 2H) and in ONX-0914-treated EAE mice (Figure S4O). We concluded that PSMB8 incorporation disrupts redox homeostasis during neuroinflammation.

PSMB8 decreases catalytic proteasome activity in neurons

Since PSMB5 and PSMB8 are the main catalytic subunits of the 20S proteasome core particle, we next measured the 20S and 26S activity in mScarlet-, PSMB5-, or PSMB8-overexpressing neurons. Unexpectedly, PSMB8 drastically decreased β5 catalytic 20S and 26S activity (Figure 3A), which contrasts with previous reports in cell lines, microglia, and astroglia.[30–32] Accordingly, PSMB8 expression levels were negatively correlated with catalytic activity, whereas PSMB5 abundance was positively associated with neuronal catalytic activity (Figures S5A and S5B). This was further confirmed when we induced endogenous PSMB8 expression by exposing neurons to IFNγ (Figures 3B, S5C, and S5D).

To test whether inflammation impairs neuronal proteasomal degradation *in vivo*, we stained K48-poly-ubiquitin, which accumulates when the proteasome is dysfunctional. We found increased K48-poly-ubiquitin levels in neurons during acute and chronic EAE (Figures S5E and S5F), and higher levels in chronic progressive EAE mice compared with those that recovered (Figure S5G). Notably, neuron-specific deletion of *Psmb8* (Figure 3C) or treatment with ONX-0914 (Figure S5H) reduced neuronal K48-poly-ubiquitin accumulation during EAE, highlighting a causal role for neuronal PSMB8 in impairing overall proteasomal activity.

Next, we sought to explore the downstream molecular mechanism of neuronal PSMB8 toxicity. Since PSMB8 leads to ROS accumulation and imbalance of metabolic co-factors (Figures 2E–2H), we hypothesized that a regulator of metabolism might accumulate during neuroinflammation. Neurons typically have a low rate of glycolysis due to a constant degradation of PFKFB3, the key switch between the PPP, which is essential for the synthesis of antioxidative co-factors, and glycolysis.[23]

As a first step, we analyzed PFKFB3 expression in neuronal cultures overexpressing mScarlet, PSMB5, or PSMB8. We found elevated PFKFB3 levels only in PSMB8-overexpressing neurons, with stronger upregulation following glutamate exposure (Figures 3D, 3E, S5I, and S5J). Furthermore, chronic IFNγ exposure increased neuronal PFKFB3 expression at baseline and excitotoxicity, an effect absent in *Psmb8*-KO neurons (Figures 3F, S5K, and S5L). Treating neurons with the pan-proteasomal inhibitor MG-132 also increased PFKFB3 levels, independent of PSMB8 overexpression, indicating that PSMB8 does not alter PFKFB3 synthesis (Figures 3D, S5M, and S5N). PSMB5 expression counteracted the PSMB8-mediated PFKFB3 accumulation (Figure S5O), further supporting the competition between β5 subunits.

Notably, neuronal PFKFB3 expression increased during both peak and late-stage EAE in C57BL/6 mice (Figure 3G), as well as during EAE relapses in SJL mice (Figure S5P) and during peak and late-stage EAE in Biozzi ABH mice (Figure S5Q). The accumulation of PFKFB3 was reversed either by genetically deleting *Psmb8* in neurons (Figures 3H and S5R) or by treating C57BL/6 EAE mice with ONX-0914 (Figure S5S). PFKFB3 also increased in astrocytes during peak EAE, and in CC1+ (pre-)myelinating oligodendrocytes in late-stage EAE, but not in microglia, NG2+ oligodendrocyte precursor cells, or endothelial cells (Figure S5T). Thus, we discovered that the inflammation-induced proteasomal switch leads to the accumulation of PFKFB3 in neurons.

The immunoproteasome modulates neuronal metabolism

To test whether IFNγ- and PSMB8-induced PFKFB3 accumulation alters neuronal metabolism, we measured mitochondrial- and glycolysis-dependent ATP production by sequentially applying inhibitors of mitochondrial respiration, glycolysis (2-desoxyglucose [2-DG]) or PFKFB3 (Pfk-158; Figure 4A). We quantified ATP and lactate levels from the supernatant (Figure S6A), as well as glucose-6-phosphate dehydrogenase activity (Figures S6B and S6C). Neurons overexpressing PSMB8 or exposed to IFNγ showed increased glycolysis (Figure 4A) without changes in mitochondrial ATP production. This effect was reversed by *Psmb8* deletion or PSMB5 overexpression (Figures 4B, S6D, and S6E). To determine whether this metabolic switch is causally linked to PFKFB3, we employed overexpression of PFKFB3, pharmacological inhibition, and genetic deletion of *Pfkfb3* in neurons (Figure S6F). PFKFB3 overexpression increased glycolytic but not mitochondrial ATP production (Figure S6G). Furthermore, chronic IFNγ exposure increased PFKFB3-dependent metabolism, a response that was absent in *Psmb8*-KO neurons (Figure 4C). Deleting *Pfkfb3* significantly reduced glycolysis-dependent ATP production in PSMB8-expressing and IFNγ-exposed neurons, but not in controls (Figures 4D and S6H).

To directly measure mitochondrial and glycolytic respiration, we employed the Seahorse assay, giving us the oxygen consumption rate (OCR) and extracellular acidification rate (ECAR). We calculated the ECAR/OCR ratio at baseline and the ECAR

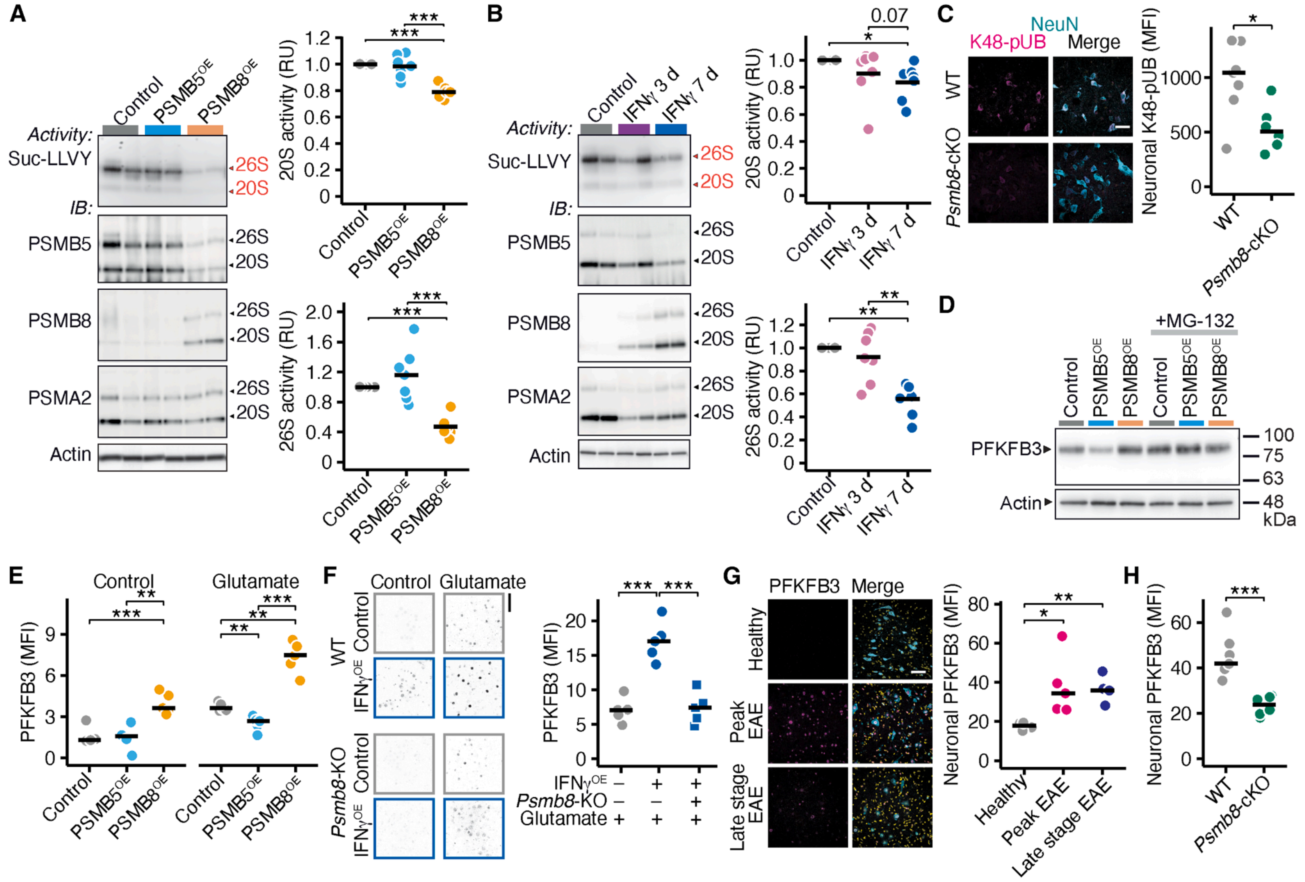

Figure 3. Neuronal PSMB8 drastically decreases proteasomal activity

(A) Proteasomal activity measured using the β5-specific substrate Suc-Leu-Leu-Val-Tyr (Suc-LLVY) in neurons overexpressing an mScarlet (control), PSMB5 ($PSMB5^{OE}$), or PSMB8 ($PSMB8^{OE}$) in native gels. Immunoblots (IBs) of PSMB5, PSMB8, and PSMA2 across all conditions of the representative activity gel are shown. Neuronal 20S and 26S activities were measured ($n = 7$) in RUs. The data were normalized to the control samples within the same gel.

(B) Proteasomal activity was measured using the β5-specific substrate Suc-LLVY in unstimulated neurons, neurons stimulated with 100 ng mL^{-1} IFNγ for 3 or 7 days in native gels. Immunoblot (IB) reprobes for PSMB5, PSMB8, and PSMA2 across all conditions in the representative activity gel are shown. Neuronal 20S and 26S activities were measured ($n = 7$) in RUs. The data were normalized to the control samples within the same gel.

(C) K48-poly-ubiquitin (K48-pUB) MFI was quantified in NeuN expressing neurons of the VHOT in the spinal cords of WT ($n = 7$) and *Psmb8*-cKO ($n = 6$) EAE during peak stage (15 days p.i.). Scale bar, 50 μm.

(D) Representative immunoblot of PFKFB3 and actin of control mScarlet-overexpressing, $PSMB5^{OE}$, and $PSMB8^{OE}$ neurons ($n = 7$), either treated with vehicle or 1 μM of the pan-proteasomal inhibitor MG-132 for 15 h. The quantification is shown in Figure S5I.

(E) Quantification of neuronal PFKFB3 MFI in control mScarlet-overexpressing, $PSMB5^{OE}$, and $PSMB8^{OE}$ neurons, either treated with vehicle or 50 μM glutamate for 6 h ($n = 5$). Representative images are shown in Figure S5J.

(F) Quantification of neuronal PFKFB3 MFI in WT and *Psmb8*-KO neurons, either overexpressing mScarlet control or IFNγ ($IFN\gamma^{OE}$), and treated with either vehicle or 50 μM glutamate for 6 h ($n = 5$). Scale bar, 50 μm.

(G) Quantification of PFKFB3 MFI in neurons of the VHOTs of the spinal cord in healthy ($n = 4$), peak EAE (15 days p.i.; $n = 5$), and late-stage EAE mice (30 days p.i.; $n = 4$). Nuclei were visualized with DAPI (yellow). Scale bar, 50 μm.

(H) Quantification of PFKFB3 MFI in neurons of the VHOTs in the spinal cord in WT ($n = 7$) and *Psmb8*-cKO ($n = 6$) EAE mice during the late stage (30 days p.i.). Representative images are shown in Figure S5R.

For (A), (B), and (E)–(G), a one-way ANOVA with post hoc Tukey's HSD tests was used. For (C) and (H), an unpaired t test was used. Individual data points and means are shown. $^{*}p < 0.05$, $^{**}p < 0.01$, $^{***}p < 0.001$, $^{****}p < 0.0001$.

See also Figures S5 and S12.

after oligomycin divided by the ECAR at baseline, which quantifies glycolytic respiration.[44–46] While PSMB8-overexpressing neurons exhibited decreased basal mitochondrial respiration, maximal respiratory capacity did not change in comparison to control or PSMB5-overexpressing neurons (Figure S6I). Notably, we detected higher glycolytic respiration in PSMB8-overexpressing neurons (Figures 4E and S6J). Chronic IFNγ stimulation increased glycolytic respiration, which was inhibited by deletion of *Psmb8* or *Pfkfb3*, as well as by pharmacological PFKFB3 inhibition, whereas mitochondrial respiration was unaltered (Figures 4F–4H and S6K–S6R). Similarly, the increased glycolytic respiration induced by PSMB8 and PFKFB3

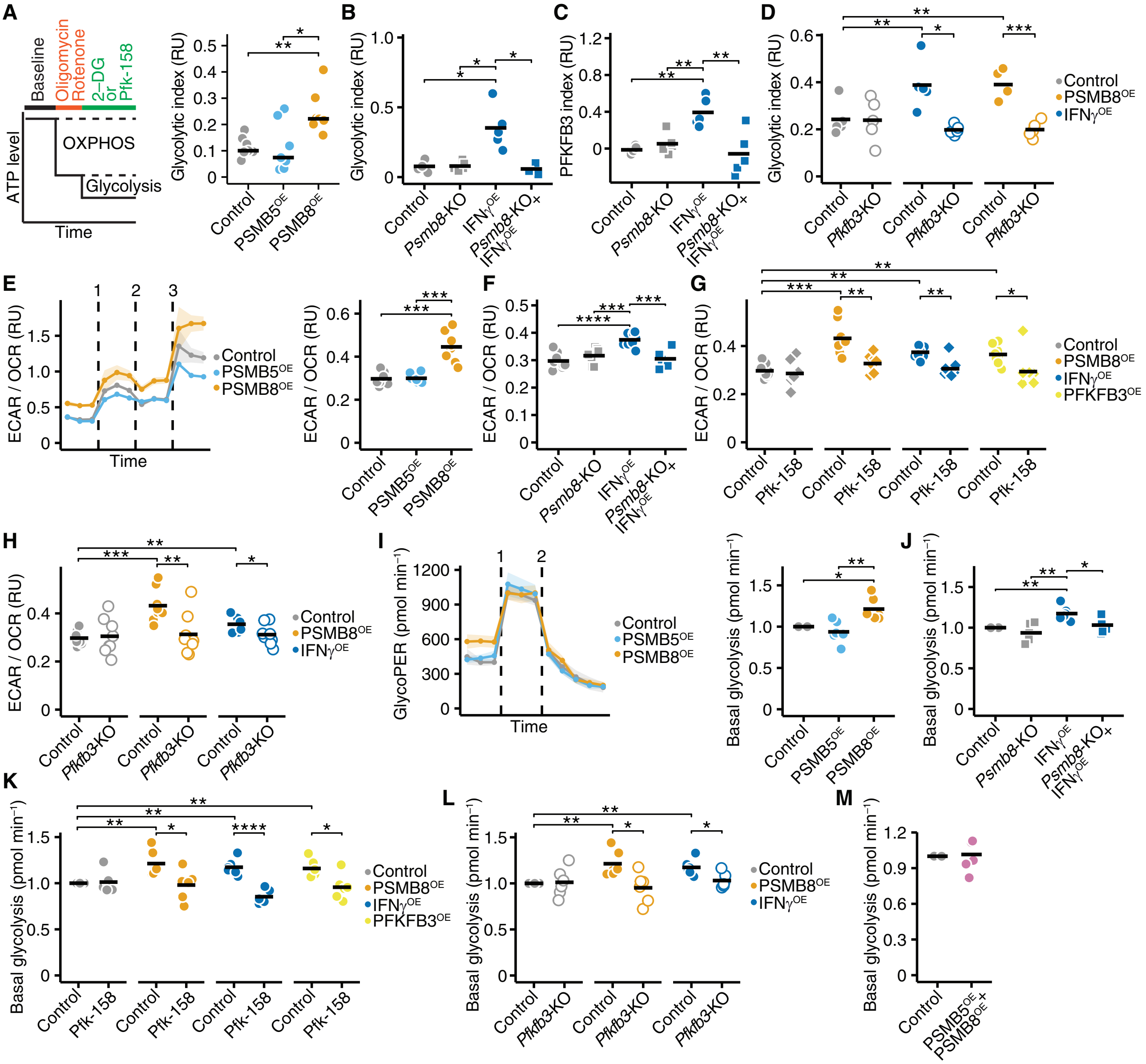

Figure 4. Proteasomal dysfunction leads to a metabolic switch in neurons

(A) Representative workflow and quantification of glycolytic and mitochondrial ATP production in RUs of mScarlet control, PSMB5 (PSMB5^{OE}), or PSMB8 (PSMB8^{OE}) overexpressing neurons (*n* = 7).

(B) Glycolytic index (RU) in WT (control) and *Psmb8*-KO neurons continuously exposed to IFNγ for 7 days (IFNγ^{OE}; *n* = 5).

(C) PFKFB3 index (RU), determined by adding 500 nM Pfk-158 after oligomycin and rotenone instead of 2-DG to estimate the PFKFB3-dependent metabolism, in WT and *Psmb8*-KO neurons continuously exposed to IFNγ for 7 days (IFNγ^{OE}; *n* = 5).

(D) Glycolytic index (RU) of WT and *Pfkfb3*-KO mScarlet control, PSMB8^{OE}, or IFNγ^{OE} neurons (*n* = 5).

(E) Representative graph of the extracellular acidification rate (ECAR) to oxygen consumption rate (OCR) ratio in RUs for mScarlet control, PSMB5^{OE}, and PSMB8^{OE} neurons (*n* = 8). ECAR and OCR were measured using the Seahorse assay by subsequently applying oligomycin (1), antimycin A plus rotenone (2), and FCCP (3). The baseline ECAR/OCR ratio was used to quantify glycolytic respiration.

(F) ECAR/OCR ratio (RU) in WT (control) and *Psmb8*-KO neurons continuously exposed to IFNγ for 7 days (IFNγ^{OE}; *n* = 8).

(G) ECAR/OCR ratio (RU) in WT, PSMB8^{OE}, PFKFB3^{OE}, and IFNγ^{OE} neurons that were treated with either vehicle control or 500 nM Pfk-158 every other day (*n* = 8).

(H) ECAR/OCR ratio (RU) of WT and *Pfkfb3*-KO mScarlet control, PSMB8^{OE}, or IFNγ^{OE} neurons (*n* = 8).

(I) Representative graph of the glycolytic PER (GlycoPER) in pmol min^{-1} for mScarlet control, PSMB5^{OE}, and PSMB8^{OE} neurons (*n* = 6). The GlykoPER was measured using the Seahorse assay by subsequently applying antimycin A plus rotenone (1), and 2-DG (2). The baseline GlycoPER was used to quantify glycolysis.

(J) Basal glycolysis (pmol min^{-1}) in WT (control) and *Psmb8*-KO neurons continuously exposed to IFNγ for 7 days (IFNγ^{OE}; *n* = 6).

(K) Basal glycolysis (pmol min^{-1}) in WT, PSMB8^{OE}, PFKFB3^{OE}, and IFNγ^{OE} neurons treated with either a vehicle control or 500 nM Pfk-158 every other day (*n* = 6).

(legend continued on next page)

overexpression was normalized by genetic or pharmacological inhibition of PFKFB3 and by PSMB5 overexpression, while mitochondrial respiration was unaffected. Notably, genetic deletion of *Pfkfb3* or *Psmb8* did not alter glycolytic respiration at baseline conditions (Figures 4G, 4H, and S6K–S6R).

We also measured the proton efflux rate (PER) that allows the direct estimation of the glycolytic PER (GlycoPER). PSMB8-overexpressing neurons showed higher basal glycolysis, whereas compensatory glycolysis following mitochondrial electron transport chain inhibition remained unaltered (Figures 4I and S7A). Similarly, continuous IFNγ exposure increased basal glycolysis, which could be reversed by deleting *Psmb8* (Figures 4J and S7B). Genetic deletion or pharmacological inhibition of PFKFB3 and PSMB5 overexpression reversed the increased glycolysis induced by PSMB8 or PFKFB3 overexpression, as well as by chronic IFNγ exposure, while deletion of *Pfkfb3* or *Psmb8* did not change basal glycolysis in control neurons (Figures 4K–4M and S7C–S7E). Thus, we demonstrate that PFKFB3 plays a negligible role in neuronal metabolism under homeostatic conditions but is crucial in the PSMB8-regulated metabolic switch.

PSMB8 decreases GSH production in neurons

Next, we examined whether PSMB8-dependent increase in glycolysis also resulted in a downregulation of the PPP. We measured nicotinamide adenine dinucleotide phosphate (NADPH), a key byproduct of the PPP that is essential for regenerating antioxidant glutathione (GSH). Indeed, PSMB8 or PFKFB3 overexpression, as well as IFNγ exposure, reduced NADPH and GSH levels (Figures 5A and 5B). These effects were reversed by PFKFB3 (Pfk-158) or glycolysis (2-DG) inhibition (Figures 5C–5H). In contrast, Pfk158 treatment of control neurons did not affect NADPH or GSH levels (Figures S7F and S7G).

We investigated whether the PSMB8-dependent metabolic changes observed *in vitro* could be recapitulated *in vivo* during EAE. We performed matrix-assisted laser desorption/ionization mass spectrometry imaging (MALDI-MSI) and analyzed metabolites in the spinal cord gray matter ventral horns from late-stage EAE wild-type (WT) and *Psmb8*-cKO mice. Our analysis revealed significantly lower levels of glycolytic byproducts, lactate, and glucose-6-phosphate, along with an accumulation of phosphoenolpyruvate, an intermediate substrate in glycolysis, indicating reduced glycolytic activity in mice with neuron-specific *Psmb8* deletion during EAE. Furthermore, fructose-1/2,6-bisphosphate was also decreased in *Psmb8*-cKO compared with WT EAE mice. Since fructose-2,6-bisphosphate synthesis depends on the activity of PFKFB3, these findings provide *in vivo* evidence that neuronal PSMB8 results in higher PFKFB3 activity in EAE. We also detected elevated levels of GSH and NADPH in *Psmb8*-cKO mice during EAE, demonstrating that neuronal *Psmb8* deletion enhances PPP activity. Differences in metabolites of the citrate cycle between WT and *Psmb8*-cKO EAE mice were not observed (Figure 5I).

Since GSH is a necessary substrate for glutathione peroxidase 4 (GPX4), the main gatekeeper of neuronal redox homeostasis,[47] we hypothesized that the PFKFB3-dependent metabolic switch might underlie the increased ROS production observed in PSMB8-expressing neurons (Figure 2G). Indeed, inhibiting glycolysis (2-DG), PFKFB3 (Pfk-158), or using the antioxidant co-enzyme Q10 in control, IFNγ-overexpressing, or PSMB8-overexpressing neurons (Figures 5K–5M), as well as genetically deleting *Psmb8* or *Pfkfb3* (Figures 5N–5P), reduced excitotoxicity-induced ROS production. Again, under control conditions, *Psmb8*-KO had no effect (Figure 5N). Thus, our data provide *in vitro* and *in vivo* evidence that IFNγ-induced PSMB8 results in a metabolic switch, driven by the accumulation of PFKFB3, which increases glycolysis, reduces PPP activity, and decreases production of antioxidative co-factors in inflamed neurons.

The metabolic switch increases neuronal vulnerability to ferroptosis

We next asked whether altered metabolism contributes to inflammation-induced neuronal death. We treated control, PSMB5-, or PSMB8-overexpressing neurons with 2-DG or Pfk-158. Both treatments reduced the PSMB8 neurotoxicity and mitigated the increased vulnerability to excitotoxicity mediated by IFNγ (Figures 6A, 6B, and S8A–S8C). Deleting *Pfkfb3* also protected against excitotoxicity in PSMB8-overexpressing and IFNγ-exposed neurons (Figure 6C). Notably, treatment with 2-DG or Pfk-158, as well as *Pfkfb3* deletion, protected control neurons from excitotoxicity (Figures 6C and S8D), consistent with glutamate-induced PFKFB3 upregulation observed by us and others.[24]

Given reduced PPP activity and GSH levels, we hypothesized that the immunoproteasome sensitizes neurons to lipid peroxidation and ferroptosis.[48] PSMB8-, PFKFB3-, and IFNγ-overexpressing neurons were more vulnerable to glutamate or RSL3 (GPX4 inhibitor), which could be rescued by treatment with radical trapping agents ferrostatin-1 or liproxstatin-1[49] (Figures 6D and 6E) or the antioxidative co-enzyme Q10 (Figure S8E).

PSMB8, PFKFB3, and IFNγ-expressing neurons displayed higher lipid peroxidation after glutamate or RSL3 exposure (Figures 6F, 6G, S8F, and S8G), which was reversed by treatment with 2-DG, Pfk-158, liproxstatin-1, or by co-expressing PSMB5 (Figures 6F–6I, S8H, and S8I). *In vivo*, we observed less neuronal 4-hydroxynoneal (4-HNE) expression, a biomarker of lipid peroxidation, in EAE mice lacking *Psmb8* in neurons or treated with ONX-0914 (Figures S8J and S8K). PSMB8 and PFKFB3 did not alter the protein expression of ferroptosis regulators acyl-co-enzyme A (CoA) synthetase long chain family member 4 (ACSL4),[50] ferroptosis suppressor 1 (FSP1),[51] or GPX4 at baseline and under excitotoxic conditions (Figure S8L). We concluded that

---

(L) Basal glycolysis (pmol min^{-1}) of WT and *Pfkfb3*-KO mScarlet control, PSMB8^{OE}, or $\text{IFN}\gamma^{\text{OE}}$ neurons ($n = 6$).

(M) Basal glycolysis (pmol min^{-1}) in neurons that overexpressing mScarlet or PSMB5 and PSMB8 simultaneously ($n = 6$).

For (A)–(C), (E), (F), (I), and (J), a one-way ANOVA with post hoc Tukey's HSD tests was used. For (D), (G), (H), (K)–(M), unpaired t tests with FDR correction for multiple comparisons were used. Individual data points and means are shown. *$p < 0.05$, **$p < 0.01$, ***$p < 0.001$, ****$p < 0.0001$.

See also Figures S6 and S12.

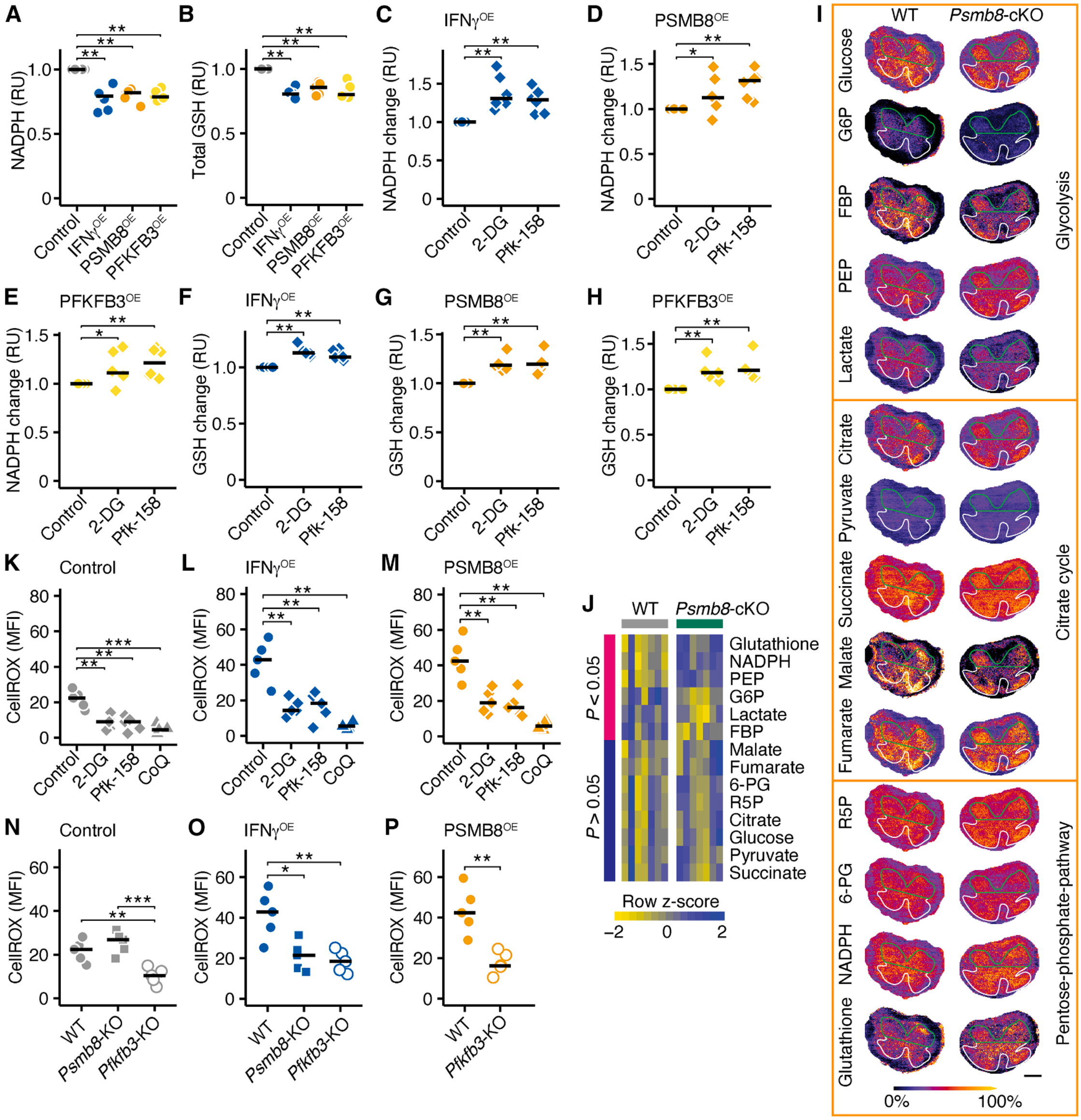

Figure 5. The immunoproteasome decreases GSH production in neurons

(A) Total NADPH levels (RU) in mScarlet control, IFNγ^{OE}, PSMB8^{OE}, or PFKFB3^{OE} neurons ($n = 5$). Data were normalized to controls.

(B) Total GSH levels (RU) in mScarlet control, IFNγ^{OE}, PSMB8^{OE}, or PFKFB3^{OE} neurons ($n = 5$). Data were normalized to controls.

(C–E) Relative NADPH change (RU) in IFNγ^{OE} (C), PSMB8^{OE} (D), and PFKFB3^{OE} (E) neurons treated every other day with 2 mM 2-DG, or 500 nM Pfk-158 ($n = 6$). Data were normalized to controls.

(F–H) Relative GSH change (RU) in IFNγ^{OE} (F), PSMB8^{OE} (G), and PFKFB3^{OE} (H) neurons treated every other day with 2 mM 2-DG, or 500 nM Pfk-158 ($n = 6$). Data were normalized to controls.

(I and J) Representative images (I) and quantification (J) of glucose, glucose-6-phosphate (G6P), fructose-1/2,6-bisphosphate (FBP), phosphoenolpyruvate (PEP), lactate, citrate, pyruvate, succinate, malate, fumarate, ribose-5-phosphate (R5P), 6-phosphogluconolactone (6-PG), NADPH, and GSH using MALDI mass spectrometry in WT and *Psmb8*-cKO ($n = 7$) mice at late EAE stage (30 days p.i.). The gray matter is indicated in white and the ventral horns in green, which were used for quantification. The row Z scores are displayed in the heatmap, and the rows are sorted by significance. Unpaired t tests were used for statistical comparison. Scale bar, 500 μm.

(K–M) Quantification of ROS by measuring CellROX MFI in mScarlet control (K), IFNγ^{OE} (L), and PSMB8^{OE} (M) neurons treated with either vehicle, 2 mM 2-DG, 500 nM Pfk-158, or 6 μM co-enzyme Q10 (CoQ) and exposed to 50 μM glutamate for 2 h ($n = 5$).

(N–P) Quantification of ROS by measuring CellROX MFI in WT, *Psmb8*-KO, and *Pfkfb3*-KO mScarlet control (N), and IFNγ^{OE} (O) neurons, or WT and *Pfkfb3*-KO PSMB8^{OE} neurons (P) after 2-h exposure to 50 μM glutamate ($n = 5$).

For (A)–(H), a Mann-Whitney U test was performed. For (K)–(P), a one-way ANOVA with post hoc Tukey's HSD tests was used. Individual data points and means are shown. $^{*}p < 0.05$, $^{**}p < 0.01$, $^{***}p < 0.001$, $^{****}p < 0.0001$.

See also Figures S7 and S12.

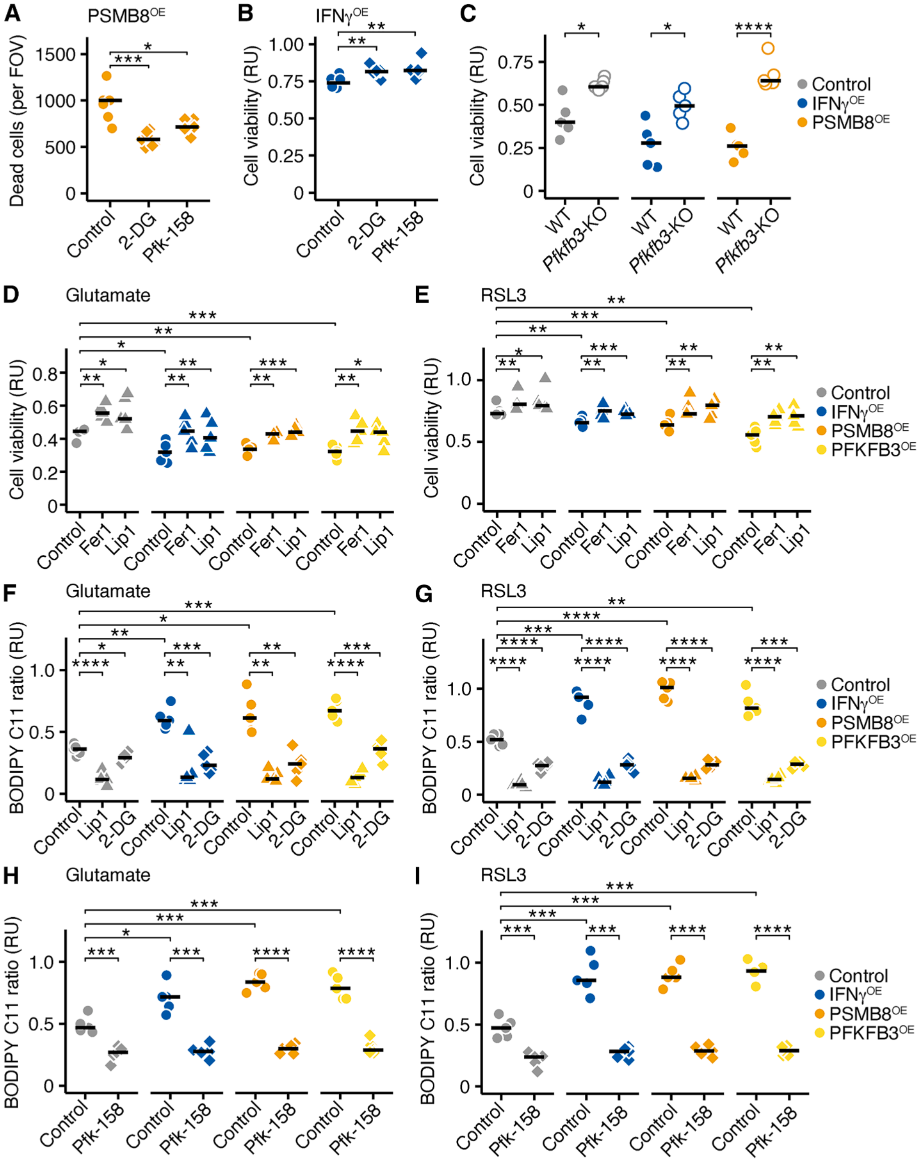

Figure 6. PFKFB3 accumulation increases the neuronal susceptibility to ferroptosis

(A) Number of dead cells per field of view (FOV) of neurons overexpressing PSMB8 for 14 days (PSMB8^{OE}) and treated every other day with 2 mM 2-DG or 500 nM Pfk-158 (*n* = 6).

(B) Cell viability in RUs of neurons chronically exposed to IFNγ for 7 days (IFNγ^{OE}) and treated with 2 mM 2-DG or 500 nM Pfk-158 prior to exposure to 50 μM glutamate for 15 h (*n* = 5).

(C) Cell viability (RU) of WT and *Pfkfb3*-KO mScarlet control, IFNγ^{OE}, and PSMB8^{OE} neurons treated with 50 μM glutamate for 15 h (*n* = 5).

(D and E) Cell viability (RU) of mScarlet control, IFNγ^{OE}, PSMB8^{OE}, and PFKFB-overexpressing neurons (PFKFB3^{OE}) treated with 10 μM ferrostatin-1 (Fer1) or 1 μM liproxstatin-1 (Lip1) prior to exposure to 50 μM glutamate (D) or 6 μM RSL3 (E) for 15 h (*n* = 5).

(F and G) Quantification of lipid peroxidation by measuring the BODIPY C11 ratio in mScarlet control, IFNγ^{OE}, PSMB8^{OE}, and PFKFB3-overexpressing neurons (PFKFB3^{OE}) treated with 1 μM Lip1, or 2 mM 2-DG before exposure to 50 μM glutamate (F) or 6 μM RSL3 (G) for 10 h (*n* = 5).

(H and I) Quantification of lipid peroxidation by measuring the BODIPY C11 ratio of mScarlet control, IFNγ^{OE}, PSMB8^{OE}, and PFKFB3-overexpressing neurons (PFKFB3^{OE}) treated with 500 nM Pfk-158 before exposure to 50 μM glutamate (F) or 6 μM RSL3 (G) for 10 h (*n* = 5).

For (A), (B), and (D)–(G), a one-way ANOVA with post hoc Tukey's HSD tests was used. For (C), (H), and (I), unpaired t tests with FDR correction for multiple comparisons were used. Individual data points and means are shown. *$p < 0.05$, **$p < 0.01$, ***$p < 0.001$, ****$p < 0.0001$.

See also Figures S8, S9, S10, and S12.

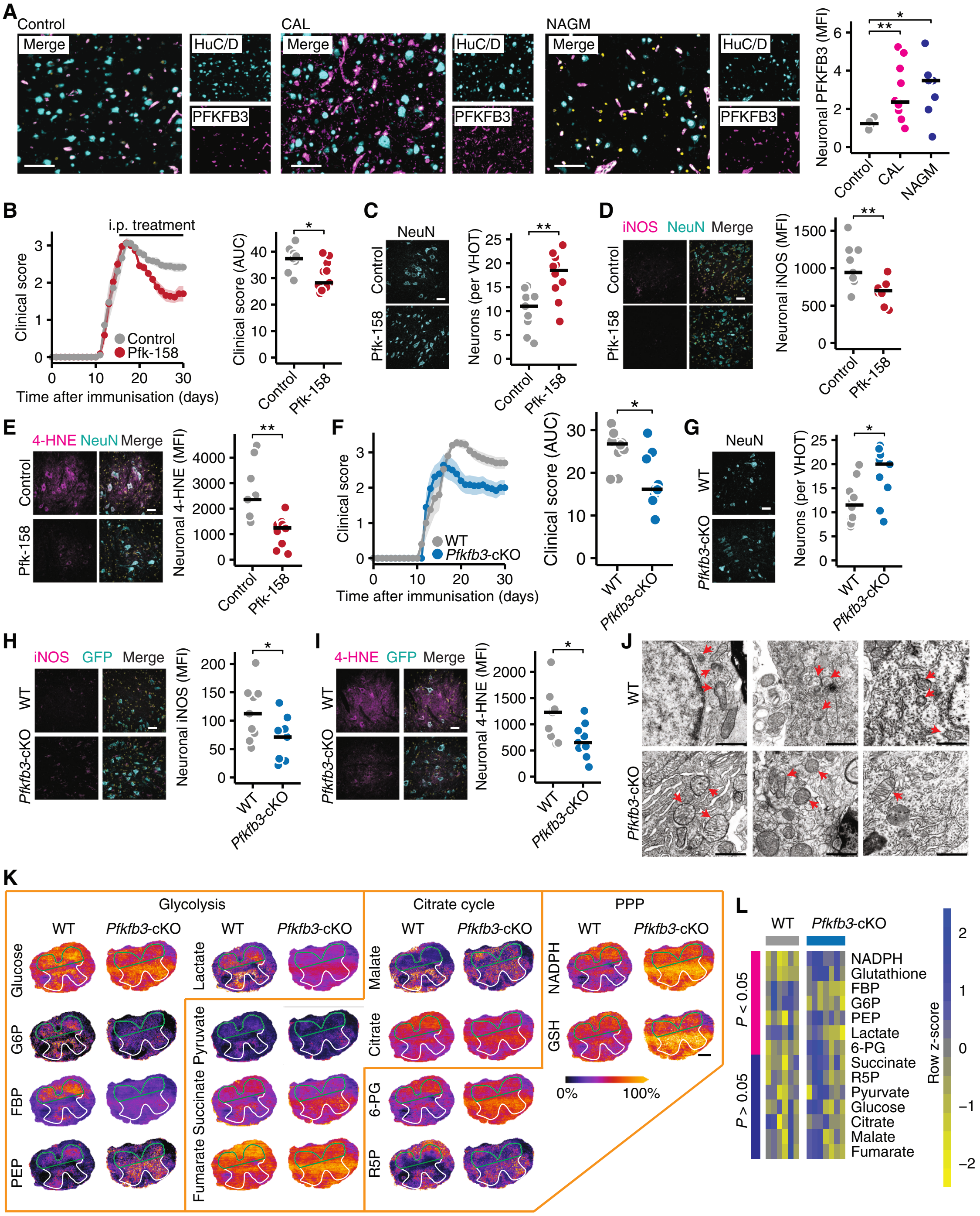

Figure 7. PFKFB3 inhibition is neuroprotective in CNS inflammation

(A) MFI of neuronal PFKFB3 in *postmortem* cortices of controls ($n = 4$), chronic active lesions (CALs) of people with relapsing MS ($n = 10$), and normal-appearing gray matter (NAGM) of people with progressive MS ($n = 7$). DAPI was stained to visualize nuclei and HuC/D to visualize neurons. Scale bar, 200 μm. A one-way ANOVA ($p < 0.05$) with post hoc Tukey's HSD tests was.

(B) EAE disease course of mice treated daily with vehicle ($n = 9$) or 12 mg kg^{-1} body weight Pfk-158 ($n = 11$) i.p., starting at the acute EAE stage, 14 days p.i. A Mann-Whitney U test was performed on the AUC during the peak and chronic disease stage (15–30 days p.i.) for statistical comparisons. Vehicle-treated mice are the same as those shown in Figure 1F since these treatments were performed in the same experiment.

(C) Quantification of neuron count in the spinal cord VHOTs of late-stage EAE mice (30 days p.i.) treated with vehicle ($n = 9$) or 12 mg kg^{-1} body weight Pfk-158 ($n = 10$) i.p. Scale bar, 50 μm.

(legend continued on next page)

the PFKFB3-mediated metabolic switch toward glycolysis increases neuronal vulnerability to oxidative injury and ferroptosis.

IFNγ-induced PFKFB3 accumulation is independent of the CDK5/CDH1 axis

Under homeostasis neurons maintain low PFKFB3 levels through continuous ubiquitination mediated by the anaphase-promoting complex (APC)/cdc20 homolog 1 (CDH1),[23] which is negatively regulated by the cyclin-dependent kinase-5 (CDK5) complex. Calcium influx or ROS stabilizes CDK5, leading to CDH1 inhibition and subsequent PFKFB3 accumulation.[52,53] Consistent, we observed increased levels of PFKFB3 (Figure 3E) and CDK5 (Figure S9A) following excitotoxic insult. Since CDK5 itself is subject to ubiquitin-mediated degradation, we investigated whether its accumulation could promote CDH1 degradation and thereby contribute to inflammation-induced PFKFB3 accumulation.

Higher CDK5 levels were observed in neurons chronically exposed to IFNγ, both at steady state and after excitotoxicity, but not in *Psmb8*-KO neurons (Figure S9A). PSMB8, but not PSMB5, overexpression also increased CDK5 protein levels and reduced CDH1 levels (Figures S9B and S9C). This pattern was replicated *in vivo*, as *Psmb8*-cKO EAE mice or ONX-0914-treated EAE mice showed lower CDK5 and higher CDH1 levels in neurons (Figures S9D–S9G).

Next, we tested whether this dysregulation explains the IFNγ- and PSMB8-mediated PFKFB3 accumulation. Overexpression of CDH1 counteracted the neuronal PFKFB3 increase during excitotoxicity, RSL3 treatment or PFKFB3 overexpression, but not in neurons that were exposed to IFNγ or overexpressing PSMB8 (Figure S9H). Similarly, treating neurons with the CDK5 inhibitor 20-223 (CDK5i) blocked the PFKFB3 increase caused by excitotoxicity, RSL3 or PFKFB3 overexpression, but not the IFNγ- or PSMB8-mediated accumulation (Figures S10A and S10B).

In line with the differential regulation of PFKFB3, CDK5 inhibition by CDK5i or roscovitine, or CDH1 overexpression counteracted excitotoxicity-induced ROS production in control and PFKFB3-overexpressing neurons, but not in PSMB8-expressing neurons (Figures S10C–S10E). Similarly, CDK5i, roscovitine, or CDH1 overexpression did not prevent glutamate- or RSL3-induced lipid peroxidation and ferroptosis in PSMB8-expressing or IFNγ-exposed neurons (Figures S10F–S10J). Thus, IFNγ-mediated proteasomal impairment leads to PFKFB3 accumulation independently of its physiological regulation by the CDK5/CDH1 axis.

PFKFB3 inhibition is neuroprotective in CNS inflammation

Finally, we asked whether PFKFB3 inhibition can be used therapeutically in CNS inflammation to protect against neurodegeneration. In *postmortem* MS brains, neuronal PFKFB3 was elevated in cortical areas with chronic active lesions and in normal-appearing gray matter, suggesting that PFKFB3 could be involved in MS-related neurodegeneration (Figure 7A). We then treated EAE mice with daily i.p. injections of Pfk-158, starting at the acute disease stage (14 days post-immunization). This treatment significantly attenuated disease severity (Figures 7B and S11A) and protected against neuronal loss (Figure 7C), synaptic loss in the spinal cord ventral horns (but not in the dorsal horns), and axonal degeneration in the dorsal columns (Figure S11B–S11D). While no differences were observed in neuronal levels of poly-ubiquitin, PFKFB3, CDK5, or CDH1 (Figures S11E–S11H), pharmacological PFKFB3 inhibition protected against oxidative neuronal injury (Figure 7D) and lipid peroxidation (Figure 7E) in EAE.

Given that systemic PFKFB3 inhibition impairs immune cell activation,[54] we tested whether neuron-specific deletion of *Pfkfb3* confers neuroprotection in EAE. Neuronal *Pfkfb3* deletion (*Pfkfb3*-cKO; Figure S11I) did not affect neuronal and axonal counts or K48-poly-ubiquitination levels in healthy mice (Figures S11J–S11L). *Pfkfb3*-cKO mice exhibited a less severe disease course (Figures 7F and S11M), characterized by reduced neuronal and synaptic loss, axonal degeneration, oxidative stress, lipid peroxidation, and mitochondrial injury (Figures 7G–7J and S11N–S11P). Of note, demyelination, poly-ubiquitination, and the levels of CDK5, CDH1, and PSMB8 (Figures S11Q–S11V) remained unchanged. Additionally, infiltration of immune cells and activation of microglia during peak and late-stage EAE

(D) Neuronal MFI of iNOS in the spinal cord VHOT of late-stage EAE mice (30 days p.i.) treated with vehicle ($n = 9$) or 12 mg kg^{-1} body weight Pfk-158 ($n = 10$) i.p. Nuclei were visualized with DAPI (yellow). Scale bar, 50 μm.

(E) Neuronal MFI of 4-hydroxynonenal (4-HNE) in the spinal cord VHOT of late-stage EAE mice (30 days p.i.) treated with vehicle ($n = 9$) or 12 mg kg^{-1} body weight Pfk-158 ($n = 10$) i.p. Nuclei were visualized with DAPI (yellow). Scale bar, 50 μm.

(F) EAE disease course of LSL-Cas9 mice injected retro-orbitally with an adeno-associated virus (AAV)-PHP.eB expressing either non-targeting guides (WT; $n = 10$) or two guides against *Pfkfb3* (*Pfkfb3*-cKO; $n = 9$), along with Cre recombinase under the control of the neuron-specific human synapsin promoter. A Mann-Whitney U test of AUC during the peak and chronic stage (15–30 days p.i.) was used for statistical comparisons.

(G) Quantification of neuron count in the spinal cord VHOT of WT ($n = 10$) and *Pfkfb3*-cKO ($n = 9$) late-stage EAE mice (30 days p.i.). Scale bar, 50 μm.

(H) Neuronal iNOS MFI in the spinal cord VHOT of WT ($n = 10$) and *Pfkfb3*-cKO ($n = 9$) late-stage EAE mice (30 days p.i.). Neuronal GFP expression indicates neurons transfected with the respective guide RNAs. Nuclei were visualized with DAPI (yellow). Scale bar, 50 μm.

(I) Neuronal 4-HNE MFI in the spinal cord VHOT of WT ($n = 10$) and Pfkfb3-cKO ($n = 9$) late-stage EAE mice (30 days p.i.). Neuronal GFP expression indicates neurons transfected with the respective guide RNAs. Nuclei were visualized with DAPI (yellow). Scale bar, 10 μm.

(J) Transmission electron microscopy images of spinal cord neurons from WT ($n = 3$) and *Pfkfb3*-cKO ($n = 3$) mice during peak EAE (15 days p.i.). Mitochondria are highlighted by the indicated arrows. Scale bar, 1 μm.

(K and L) Representative images (K) and quantification (L) of glucose, glucose-6-phosphate (G6P), fructose-1/2,6-bisphosphate (FBP), phosphoenolpyruvate (PEP), lactate, citrate, pyruvate, succinate, malate, fumarate, ribose-5-phosphate (R5P), 6-phosphogluconolactone (6-PG), NADPH, and GSH using MALDI mass spectrometry in WT ($n = 6$) and *Pfkfb3*-cKO ($n = 7$) mice at late-stage of EAE (30 days p.i.). The gray matter is indicated in white and the ventral horns in green, which were used for quantification. The row *Z* scores are shown in the heatmap and the rows are sorted by significance. Unpaired t tests were used for statistical comparison. Scale bar, 500 μm.

Unless stated otherwise, the Mann-Whitney U test was used for statistical comparisons, and individual data points and means are shown. $^{*}p < 0.05$, $^{**}p < 0.01$. See also Figures S11 and S12.

(Figures S11W–S11AC) were comparable between *Pfkfb3*-cKO and control mice.

Using MALDI-MSI, we confirmed reduced enzymatic activity of PFKFB3 in *Pfkfb3*-cKO EAE mice by detecting decreased levels of its metabolite, fructose-1/2,6-bisphosphate. We also observed lower levels of glucose-6-phosphate and lactate and higher levels of phosphoenolpyruvate, NADPH, and GSH in the spinal cord ventral horns of *Pfkfb3*-cKO mice during late-stage EAE. Notably, these effects occurred independently of mitochondrial respiration, as citrate cycle metabolite levels were comparable between *Pfkfb3*-cKO and control EAE mice (Figures 7K and 7L). Thus, our data identify PFKFB3 as a critical metabolic switch in neurons, controlling antioxidative defense mechanisms during CNS inflammation.

DISCUSSION

This study identifies the immunoproteasome subunit PSMB8 as a key driver of inflammation-induced neurodegeneration. In inflamed neurons, IFNγ-induced PSMB8 reduces the neuronal proteasome activity, thereby promoting the accumulation of PFKFB3. This metabolic enzyme increases glycolysis and suppresses PPP activity, leading to the depletion of antioxidative co-factors such as GSH and sensitizing neurons to ferroptosis by impairing GPX4-mediated detoxification of phospholipid hydroperoxides. Previously, we showed that IFNγ also induces the stimulator of interferon genes (STING) in neurons, resulting in autophagic GPX4 degradation.[8] While PSMB8 and PFKFB3 did not affect GPX4 levels, they reduced GSH by limiting PPP activity. Thus, PSMB8 and STING impair distinct arms of the neuronal antioxidant system, acting synergistically to promote ferroptosis.

Unlike immune or tumor cells, neurons failed to upregulate PSMB8 in response to TNF-α[55] or MS-relevant cytokines,[56] including IL-17, IL-1β, and GM-CSF. However, IFNα also induced PSMB8, suggesting a shared response to type I and type II IFNs in neurons. Despite constitutive type I IFN signaling in neurons due to double-stranded RNA content,[57] we observed no PSMB8 expression in healthy neurons. This suggests exclusive signaling pathways that are activated in neuroinflammatory and possibly NDDs through chronic exposure to IFNs. Understanding this distinct NISR may enable treatment strategies for inflammation-induced neurodegeneration, addressing an unmet clinical need in MS and beyond.

We focused on chronic IFNγ exposure, likely derived from CNS-resident or infiltrating CD8+ T cells,[58] and found that it profoundly disrupts neuronal UPS function, undermining metabolic homeostasis. As such, UPS modulation emerges as attractive treatment option. Deubiquitinating enzyme inhibitors have shown to be neuroprotective in EAE,[15] and enhancing pharmacological clearance of accumulated synaptic proteins improves outcomes in MS and AD models.[15,59] Our data show that neuronal PSMB8 induction disrupts proteostasis, leads to protein accumulations, and contributes to neuronal loss, while its deletion in EAE mice restores UPS function and protects neurons.

Neuroinflammation is a hallmark of NDDs and aging and predicts disease progression in MS, AD, or PD.[2,7,60] The induction of PSMB8 in neurons may represent a unifying mechanism underlying UPS dysfunction across these disorders. Region-specific proteasome inhibition can recapitulate neurodegenerative features with disease-specific protein accumulations.[61–64] Furthermore, several hereditary NDDs are linked to mutations affecting the UPS, and genome-wide association studies in AD have shown associations between the UPS, protein accumulations, and disease severity.[65–67] Notably, we demonstrate that inflammation alone is sufficient to impair neuronal UPS function and promote toxic protein accumulations. The immunoproteasome induction may therefore represent a critical "tipping point[68]" in NDDs that determines disease progression.

The loss of proteasome activity in neurons was caused by the incorporation of PSMB8 into the 20S core, likely due to its preferential interaction with the proteasome maturation protein (POMP).[69] This contrasts with dividing cells, where PSMB8 enhances activity and protects against inflammation-induced proteotoxic stress and oxidative injury.[30–32] Loss-of-function *PSMB8* mutations cause proteasome-associated autoinflammatory syndromes (PRAASs) through the accumulation of poly-ubiquitinated proteins, ROS accumulation, and aberrant immune cell activation,[70–72] indicating its essential role in immune cells. However, neurons showed no baseline PSMB8 expression; instead, its induction increased ROS production and ferroptosis, which could be counteracted by PSMB5 overexpression. This competition may underlie the neuroprotective effects of immunoproteasome inhibitor ONX-0914 treatment in EAE, beyond its immunosuppressive properties. Of note, in an AD mouse model, decreased proteasome activity was rescued by transgenic overexpression of PSMB5,[73] suggesting that increasing proteasome activity in neurons may be a viable treatment strategy across NDDs. While the immunoproteasome regulates MHC class I antigenic peptide processing in immune and endothelial cells,[28,29] neuronal PSMB8 expression did not alter MHC class I levels or CNS T cell infiltration in EAE. This suggests that antigen presentation by neurons to CD8 + T cells is not relevant for disease progression or differs from immune cells.

Our findings emphasize the need to investigate neuron-specific mechanisms. This difference between post-mitotic neurons and dividing cells extend to PFKFB3, the main glycolytic switch.[74] Neurons exhibit low PFKFB3 expression due to continuous degradation[23] that is controlled by the E3 ubiquitin ligase CDH1 and the kinase CDK5, which initiates CDH1 degradation through phosphorylation. Neuronal calcium accumulation and oxidative stress stabilize CDK5, inhibiting CDH1[24,25] and leading to PFKFB3 accumulation. Prolonged increases in PFKFB3 protein abundance in neurons due to excitotoxicity, oxidative injury,[24,25] or transgenic overexpression[22] promotes a metabolic shift from the PPP to glycolysis, which accelerates cell death. We identified that an inflammation-induced imbalance of the neuronal PSMB5/PSMB8 ratio induces a metabolic switch by reducing PFKFB3 degradation, decreasing PPP activity and GSH production. Notably, this switch occurs independently of CDK5 and CDH1 under inflammatory conditions, highlighting that the physiological homeostatic mechanisms of PFKFB3 degradation are impaired. This metabolic switch renders neurons more vulnerable to excitotoxicity and ferroptosis. Of note, CDH1 was reduced in PSMB8-expressing neurons despite impaired proteasome function, suggesting alternate degradation pathways.[75] Notably, while we and others[76,77] have observed an upregulation of PSMB8 in

NG2+ oligodendrocyte progenitor cells and CC1+ (pre-)myelinating oligodendrocytes in EAE, PFKFB3 only accumulated in CC1+ (pre-)myelinating oligodendrocytes at later disease stages. This may contribute to the vulnerability of myelinating oligodendrocytes to ferroptosis in EAE and MS,[78,79] further supporting PFKFB3 inhibition as a promising treatment strategy for MS. The inflammation-dependent accumulation of PFKFB3 may also explain the shift to glycolysis in aging and NDDs.[80,81]

Limitations of the study

While we identified PSMB8 as a key modulator of inflammation-induced aberrant proteostasis in neurons, several questions remain. First, although PSMB8 or PFKFB3 expression reduced PPP activity and GSH levels, this antioxidant was not fully depleted, suggesting alternative sources of GSH in neurons that may be differentially regulated during CNS inflammation. Second, since the immunoproteasome has been unexplored in neurons, we focused on its general function. However, neuronal subtypes have distinct expression profiles, activities, and morphologies,[82] and it is likely that the constitutive and immunoproteasome exhibit subtype-specific functions, which should be characterized in future studies. Third, while we focused on the neuron-intrinsic effects of the immunoproteasome, immunophenotyping revealed an increased lymphocyte infiltration during peak EAE in *Psmb8*-cKO mice, which was not explained by differential neuronal MHC class I expression, cytokine expression by T cells, or microglia activation. It is possible that the immunoproteasome alters the secreted peptidome of neurons, which may differently regulate the immune response.[83] The immunoproteasome-dependent neuronal secretome should be subject to subsequent investigations. Lastly, while our findings are supported by cell-type-specific deletions in neuronal cultures and EAE mice, the pharmacological inhibitors used are immunosuppressive.[39,40,84,85] Although individuals with autoimmune disorders such as MS may benefit from an additional immunomodulation, a neuron-specific approach may be more appropriate for treating NDDs. Future studies should explore novel technologies such as biodegraders[86] to specifically target PSMB8 or PFKFB3 in neurons.

RESOURCE AVAILABILITY

Lead contact

Further information and requests for resources and reagents should be directed to and will be fulfilled by the lead contact, Manuel A. Friese (manuel.friese@zmnh.uni-hamburg.de).

Materials availability

Plasmids and mouse lines generated in this study are available upon reasonable request from the corresponding author.

Data and code availability

- Bulk mRNA sequencing data have been deposited at Gene Expression Omnibus (GEO: GSE279705, GSE279706, and GSE279707) and are publicly available as of the date of publication. Accession numbers are listed in the key resources table. This paper analyzes existing, publicly available data. These accession numbers for the datasets are listed in the key resources table. All other data reported in this paper will be shared by the lead contact upon request.
- This paper does not report original code.
- Any additional information required to reanalyze the data reported in this paper is available from the lead contact upon request.

ACKNOWLEDGMENTS

We thank the Friese and Meyer-Schwesinger laboratories for helpful discussions. We thank our mouse histopathology facility at the UKE for performing immunohistochemistry on paraffin-embedded tissues. Furthermore, we thank the virus vector facility at the UKE for producing AAVs. We thank Christina Schmidt for her help with electron microscopy. This work was funded by the Deutsche Forschungsgemeinschaft FOR 5705 (FR 1720/29-1 to M.A.F, ME 2108/15-1 to C.M.-S., GL 589/12-1 to M.G., EN 1328/3-1 to J.B.E., and KE 774/6-1 to M.K.) and SPP 2306 (FR 1720/30-1 to M.A.F. and WO 2835/1-1 to M.S.W.). The MALDI-TOF-MS is supported by the Deutsche Forschungsgemeinschaft (426788273). M.S.W. is funded by the Else Kröner Memorial Fellowship of the Else Kröner-Fresenius-Stiftung (2023_EKMS.03). D.M. is supported by the Swiss National Science Foundation (310030_215050 and 310030B_201271) and European Research Council (865026). V.G.P. is supported by the NovoNordisk Foundation (Young Investigator: NNF21OC0066381) and Bundesministerium für Bildung und Forschung (BMBF: eMed Junior Consortium Fibromap).

AUTHOR CONTRIBUTIONS

M.S.W., C.M.-S., and M.A.F. designed and planned experiments. M.S.W. performed and analyzed most experiments. J.B., V.V., M. Wang, B.D., D.L., and C. M. performed immunoblots. J.B., D.L., and M. Wang measured proteasome activity. M.S.W. and L.C.B. performed Seahorse experiments. D.N., K.M.-J. M., L.C.B., A.M., and L.B.-L. helped with immunostainings and cloning. M. Walkenhorst, I. Winschel, J.K.S., S.B., and N.M. performed FACS experiments. N.R., G.S., and J.B.E. performed nucleus sequencing. M.S.W., C.M., and L.K.P. performed C57BL/6 and SJL EAE experiments. T.M., M.K., and D.M. performed Biozzi ABH EAE experiments. I.I. and J.B.E. performed neuronal immunoprecipitation for neuronal proteomics. P.L., A.M., and D.C. D. provided mouse line and reagents for neuronal proteome tagging and helped with experimental procedures. H.K.G. performed ELISA. M.v.H. and L.J. performed mass spectrometry analysis for neuronal proteome tagging. M.M., N.F., and M.R. performed MALDI-MSI. I. Wagner, M.G., and D.M. provided human samples and performed immunostainings. E.K. and F.L.H. generated *Psmb8*-floxed mice. V.G.P. and J.R.N. conceptualized and performed transmission electron microscopy analyses. M.S.W. and M.A.F. wrote the first version of the manuscript. C.M.-S. and M.A.F. provided funding for the work. M.A.F. initiated the study. All co-authors contributed to the editing and discussion of the manuscript and approved the final version.

DECLARATION OF INTERESTS

The authors declare no competing interests.

STAR★METHODS

Detailed methods are provided in the online version of this paper and include the following:

- KEY RESOURCES TABLE
- EXPERIMENTAL MODEL AND STUDY PARTICIPANT DETAILS
  - Human subjects
  - Animals
  - Cells
- METHOD DETAILS
  - Vector construction
  - Lentiviral production and transduction
  - Neuronal proteome analysis in LSL-R26-MetRS* animals
  - Generation of mouse neuronal cultures with conditional knockouts
  - Compounds and chemicals
  - Proteasome activity
  - IFNγ ELISA

  - Cell viability assays
  - Estimation of mitochondrial and glycolytic respiration
  - Seahorse assay
  - GSH estimation
  - Lactate estimation
  - Glucose-6-phosphate dehydrogenase (G6PD) activity estimation
  - Nicotinamide adenine dinucleotide phosphate (NADPH) estimation
  - MALDI mass spectrometry imaging
  - Reactive oxygen species (ROS) live cell imaging
  - Lipid peroxidation live cell imaging
  - Immunocytochemistry
  - Experimental autoimmune encephalomyelitis (EAE)
  - RNA sequencing and analysis
  - Nucleus isolation and flow cytometric sorting
  - Mouse histopathology
  - Human histopathology
  - Transmission electron microscopy
  - Immunoblot
  - Real-time PCR
  - Immunophenotyping by flow cytometry
- QUANTIFICATION AND STATISTICAL ANALYSIS

SUPPLEMENTAL INFORMATION

Supplemental information can be found online at https://doi.org/10.1016/j.cell.2025.05.029.

Received: November 26, 2024
Revised: March 23, 2025
Accepted: May 21, 2025
Published: June 17, 2025

REFERENCES

1. Woo, M.S., Engler, J.B., and Friese, M.A. (2024). The neuropathobiology of multiple sclerosis. Nat. Rev. Neurosci. *25*, 493–513. https://doi.org/10.1038/s41583-024-00823-z.
2. Attfield, K.E., Jensen, L.T., Kaufmann, M., Friese, M.A., and Fugger, L. (2022). The immunology of multiple sclerosis. Nat. Rev. Immunol. *22*, 734–750. https://doi.org/10.1038/s41577-022-00718-z.
3. Wilson, D.M., Cookson, M.R., Van Den Bosch, L., Zetterberg, H., Holtzman, D.M., and Dewachter, I. (2023). Hallmarks of neurodegenerative diseases. Cell *186*, 693–714. https://doi.org/10.1016/j.cell.2022.12.032.
4. López-Otín, C., Blasco, M.A., Partridge, L., Serrano, M., and Kroemer, G. (2023). Hallmarks of aging: An expanding universe. Cell *186*, 243–278. https://doi.org/10.1016/j.cell.2022.11.001.
5. Lindestam Arlehamn, C.S., Dhanwani, R., Pham, J., Kuan, R., Frazier, A., Rezende Dutra, J., Phillips, E., Mallal, S., Roederer, M., Marder, K.S., et al. (2020). α-Synuclein-specific T cell reactivity is associated with preclinical and early Parkinson's disease. Nat. Commun. *11*, 1875. https://doi.org/10.1038/s41467-020-15626-w.
6. Rossi, S., Motta, C., Studer, V., Macchiarulo, G., Germani, G., Finardi, A., Furlan, R., Martino, G., and Centonze, D. (2015). Subclinical central inflammation is risk for RIS and CIS conversion to MS. Mult. Scler. *21*, 1443–1452. https://doi.org/10.1177/1352458514564482.
7. Pascoal, T.A., Benedet, A.L., Ashton, N.J., Kang, M.S., Therriault, J., Chamoun, M., Savard, M., Lussier, F.Z., Tissot, C., Karikari, T.K., et al. (2021). Microglial activation and tau propagate jointly across Braak stages. Nat. Med. *27*, 1592–1599. https://doi.org/10.1038/s41591-021-01456-w.
8. Woo, M.S., Mayer, C., Binkle-Ladisch, L., Sonner, J.K., Rosenkranz, S.C., Shaposhnykov, A., Rothammer, N., Tsvilovskyy, V., Lorenz, S.M., Raich, L., et al. (2024). STING orchestrates the neuronal inflammatory stress response in multiple sclerosis. Cell *187*, 4043–4060.e30. https://doi.org/10.1016/j.cell.2024.05.031.
9. Di Liberto, G., Pantelyushin, S., Kreutzfeldt, M., Page, N., Musardo, S., Coras, R., Steinbach, K., Vincenti, I., Klimek, B., Lingner, T., et al. (2018). Neurons under T Cell Attack Coordinate Phagocyte-Mediated Synaptic Stripping. Cell *175*, 458–471.e19. https://doi.org/10.1016/j.cell.2018.07.049.
10. Jorfi, M., Park, J., Hall, C.K., Lin, C.J., Chen, M., von Maydell, D., Kruskop, J.M., Kang, B., Choi, Y., Prokopenko, D., et al. (2023). Infiltrating CD8+ T cells exacerbate Alzheimer's disease pathology in a 3D human neuroimmune axis model. Nat. Neurosci. *26*, 1489–1504. https://doi.org/10.1038/s41593-023-01415-3.
11. Panagiotakopoulou, V., Ivanyuk, D., De Cicco, S., Haq, W., Arsić, A., Yu, C., Messelodi, D., Oldrati, M., Schöndorf, D.C., Perez, M.-J., et al. (2020). Interferon-γ signaling synergizes with LRRK2 in neurons and microglia derived from human induced pluripotent stem cells. Nat. Commun. *11*, 5163. https://doi.org/10.1038/s41467-020-18755-4.
12. Kaya, T., Mattugini, N., Liu, L., Ji, H., Cantuti-Castelvetri, L., Wu, J., Schifferer, M., Groh, J., Martini, R., Besson-Girard, S., et al. (2022). CD8+ T cells induce interferon-responsive oligodendrocytes and microglia in white matter aging. Nat. Neurosci. *25*, 1446–1457. https://doi.org/10.1038/s41593-022-01183-6.
13. Berriat, F., Lobsiger, C.S., and Boillée, S. (2023). The contribution of the peripheral immune system to neurodegeneration. Nat. Neurosci. *26*, 942–954. https://doi.org/10.1038/s41593-023-01323-6.
14. Woo, M.S., Ufer, F., Rothammer, N., Di Liberto, G., Binkle, L., Haferkamp, U., Sonner, J.K., Engler, J.B., Hornig, S., Bauer, S., et al. (2021). Neuronal metabotropic glutamate receptor 8 protects against neurodegeneration in CNS inflammation. J. Exp. Med. *218*, e20201290. https://doi.org/10.1084/jem.20201290.
15. Schattling, B., Engler, J.B., Volkmann, C., Rothammer, N., Woo, M.S., Petersen, M., Winkler, I., Kaufmann, M., Rosenkranz, S.C., Fejtova, A., et al. (2019). Bassoon proteinopathy drives neurodegeneration in multiple sclerosis. Nat. Neurosci. *22*, 887–896. https://doi.org/10.1038/s41593-019-0385-4.
16. Rosenkranz, S.C., Shaposhnykov, A.A., Träger, S., Engler, J.B., Witte, M.E., Roth, V., Vieira, V., Paauw, N., Bauer, S., Schwencke-Westphal, C., et al. (2021). Enhancing mitochondrial activity in neurons protects against neurodegeneration in a mouse model of multiple sclerosis. eLife *10*, 1875. https://doi.org/10.7554/eLife.61798.
17. Jhelum, P., Zandee, S., Ryan, F., Zarruk, J.G., Michalke, B., Venkataramani, V., Curran, L., Klement, W., Prat, A., and David, S. (2023). Ferroptosis induces detrimental effects in chronic EAE and its implications for progressive MS. Acta Neuropathol. Commun. *11*, 121. https://doi.org/10.1186/s40478-023-01617-7.
18. Van San, E., Debruyne, A.C., Veeckmans, G., Tyurina, Y.Y., Tyurin, V.A., Zheng, H., Choi, S.M., Augustyns, K., van Loo, G., Michalke, B., et al. (2023). Ferroptosis contributes to multiple sclerosis and its pharmacological targeting suppresses experimental disease progression. Cell Death Differ. *30*, 2092–2103. https://doi.org/10.1038/s41418-023-01195-0.
19. Luoqian, J., Yang, W., Ding, X., Tuo, Q.Z., Xiang, Z., Zheng, Z., Guo, Y.J., Li, L., Guan, P., Ayton, S., et al. (2022). Ferroptosis promotes T-cell activation-induced neurodegeneration in multiple sclerosis. Cell. Mol. Immunol. *19*, 913–924. https://doi.org/10.1038/s41423-022-00883-0.
20. Tai, Y.-H., Engels, D., Locatelli, G., Emmanouilidis, I., Fecher, C., Theodorou, D., Müller, S.A., Licht-Mayer, S., Kreutzfeldt, M., Wagner, I., et al. (2023). Targeting the TCA cycle can ameliorate widespread axonal energy deficiency in neuroinflammatory lesions. Nat. Metab. *5*, 1364–1381. https://doi.org/10.1038/s42255-023-00838-3.
21. Woo, M.S., Bal, L.C., Winschel, I., Manca, E., Walkenhorst, M., Sevgili, B., Sonner, J.K., Di Liberto, G., Mayer, C., Binkle-Ladisch, L., et al. (2024). The NR4A2/VGF pathway fuels inflammation-induced neurodegeneration via promoting neuronal glycolysis. J. Clin. Invest. *134*, e177692. https://doi.org/10.1172/JCI177692.

22. Jimenez-Blasco, D., Agulla, J., Lapresa, R., Garcia-Macia, M., Bobo-Jimenez, V., Garcia-Rodriguez, D., Manjarres-Raza, I., Fernandez, E., Jeanson, Y., Khoury, S., et al. (2024). Weak neuronal glycolysis sustains cognition and organismal fitness. Nat. Metab. *6*, 1253–1267. https://doi.org/10.1038/s42255-024-01049-0.
23. Herrero-Mendez, A., Almeida, A., Fernández, E., Maestre, C., Moncada, S., and Bolaños, J.P. (2009). The bioenergetic and antioxidant status of neurons is controlled by continuous degradation of a key glycolytic enzyme by APC/C–Cdh1. Nat. Cell Biol. *11*, 747–752. https://doi.org/10.1038/ncb1881.
24. Rodriguez-Rodriguez, P., Fernandez, E., Almeida, A., and Bolaños, J.P. (2012). Excitotoxic stimulus stabilizes PFKFB3 causing pentose-phosphate pathway to glycolysis switch and neurodegeneration. Cell Death Differ. *19*, 1582–1589. https://doi.org/10.1038/cdd.2012.33.
25. Lopez-Fabuel, I., Garcia-Macia, M., Buondelmonte, C., Burmistrova, O., Bonora, N., Alonso-Batan, P., Morant-Ferrando, B., Vicente-Gutierrez, C., Jimenez-Blasco, D., Quintana-Cabrera, R., et al. (2022). Aberrant upregulation of the glycolytic enzyme PFKFB3 in CLN7 neuronal ceroid lipofuscinosis. Nat. Commun. *13*, 536. https://doi.org/10.1038/s41467-022-28191-1.
26. Bi, M., Du, X., Jiao, Q., Chen, X., and Jiang, H. (2021). Expanding the role of proteasome homeostasis in Parkinson's disease: beyond protein breakdown. Cell Death Dis. *12*, 154. https://doi.org/10.1038/s41419-021-03441-0.
27. Rousseau, A., and Bertolotti, A. (2018). Regulation of proteasome assembly and activity in health and disease. Nat. Rev. Mol. Cell Biol. *19*, 697–712. https://doi.org/10.1038/s41580-018-0040-z.
28. Kincaid, E.Z., Che, J.W., York, I., Escobar, H., Reyes-Vargas, E., Delgado, J.C., Welsh, R.M., Karow, M.L., Murphy, A.J., Valenzuela, D.M., et al. (2011). Mice completely lacking immunoproteasomes show major changes in antigen presentation. Nat. Immunol. *13*, 129–135. https://doi.org/10.1038/ni.2203.
29. Sachs, W., Blume, L., Loreth, D., Schebsdat, L., Hatje, F., Koehler, S., Wedekind, U., Sachs, M., Zieliniski, S., Brand, J., et al. (2024). The proteasome modulates endocytosis specifically in glomerular cells to promote kidney filtration. Nat. Commun. *15*, 1897. https://doi.org/10.1038/s41467-024-46273-0.
30. Seifert, U., Bialy, L.P., Ebstein, F., Bech-Otschir, D., Voigt, A., Schröter, F., Prozorovski, T., Lange, N., Steffen, J., Rieger, M., et al. (2010). Immunoproteasomes Preserve Protein Homeostasis upon Interferon-Induced Oxidative Stress. Cell *142*, 613–624. https://doi.org/10.1016/j.cell.2010.07.036.
31. Çetin, G., Studencka-Turski, M., Venz, S., Schormann, E., Junker, H., Hammer, E., Völker, U., Ebstein, F., and Krüger, E. (2022). Immunoproteasomes control activation of innate immune signaling and microglial function. Front. Immunol. *13*, 982786. https://doi.org/10.3389/fimmu.2022.982786.
32. Orre, M., Kamphuis, W., Dooves, S., Kooijman, L., Chan, E.T., Kirk, C.J., Dimayuga Smith, V., Koot, S., Mamber, C., Jansen, A.H., et al. (2013). Reactive glia show increased immunoproteasome activity in Alzheimer's disease. Brain *136*, 1415–1431. https://doi.org/10.1093/brain/awt083.
33. Sun, C., Desch, K., Nassim-Assir, B., Giandomenico, S.L., Nemcova, P., Langer, J.D., and Schuman, E.M. (2023). An abundance of free regulatory (19S) proteasome particles regulates neuronal synapses. Science *380*, eadf2018. https://doi.org/10.1126/science.adf2018.
34. Wheeler, M.A., Clark, I.C., Tjon, E.C., Li, Z., Zandee, S.E.J., Couturier, C. P., Watson, B.R., Scalisi, G., Alkwai, S., Rothhammer, V., et al. (2020). MAFG-driven astrocytes promote CNS inflammation. Nature *578*, 593–599. https://doi.org/10.1038/s41586-020-1999-0.
35. Jordão, M.J.C., Sankowski, R., Brendecke, S.M., Sagar, L., Locatelli, G., Tai, Y.-H., Tay, T.L., Schramm, E., Armbruster, S., Hagemeyer, N., et al. (2019). Single-cell profiling identifies myeloid cell subsets with distinct fates during neuroinflammation. Science *363*, eaat7554. https://doi.org/10.1126/science.aat7554.
36. Absinta, M., Maric, D., Gharagozloo, M., Garton, T., Smith, M.D., Jin, J., Fitzgerald, K.C., Song, A., Liu, P., Lin, J.-P., et al. (2021). A lymphocyte–microglia–astrocyte axis in chronic active multiple sclerosis. Nature *597*, 709–714. https://doi.org/10.1038/s41586-021-03892-7.
37. Alvarez-Castelao, B., Schanzenbächer, C.T., Hanus, C., Glock, C., Tom Dieck, S., Dörrbaum, A.R., Bartnik, I., Nassim-Assir, B., Ciirdaeva, E., Mueller, A., et al. (2017). Cell-type-specific metabolic labeling of nascent proteomes in vivo. Nat. Biotechnol. *35*, 1196–1201. https://doi.org/10.1038/nbt.4016.
38. Reichelt, J., Sachs, W., Frömbling, S., Fehlert, J., Studencka-Turski, M., Betz, A., Loreth, D., Blume, L., Witt, S., Pohl, S., et al. (2023). Non-functional ubiquitin C-terminal hydrolase L1 drives podocyte injury through impairing proteasomes in autoimmune glomerulonephritis. Nat. Commun. *14*, 2114. https://doi.org/10.1038/s41467-023-37836-8.
39. Althof, N., Goetzke, C.C., Kespohl, M., Voss, K., Heuser, A., Pinkert, S., Kaya, Z., Klingel, K., and Beling, A. (2018). The immunoproteasome-specific inhibitor ONX 0914 reverses susceptibility to acute viral myocarditis. EMBO Mol. Med. *10*, 200–218. https://doi.org/10.15252/emmm.201708089.
40. Zilberberg, J., Matos, J., Dziopa, E., Dziopa, L., Yang, Z., Kirk, C.J., Assefnia, S., and Korngold, R. (2015). Inhibition of the Immunoproteasome Subunit LMP7 with ONX 0914 Ameliorates Graft-versus-Host Disease in an MHC-Matched Minor Histocompatibility Antigen–Disparate Murine Model. Biol. Blood Marrow Transplant. *21*, 1555–1564. https://doi.org/10.1016/j.bbmt.2015.06.010.
41. Kamogashira, T., Hayashi, K., Fujimoto, C., Iwasaki, S., and Yamasoba, T. (2017). Functionally and morphologically damaged mitochondria observed in auditory cells under senescence-inducing stress. npj Aging Mech. Dis. *3*, 2. https://doi.org/10.1038/s41514-017-0002-2.
42. Costa, V., Giacomello, M., Hudec, R., Lopreiato, R., Ermak, G., Lim, D., Malorni, W., Davies, K.J.A., Carafoli, E., and Scorrano, L. (2010). Mitochondrial fission and cristae disruption increase the response of cell models of Huntington's disease to apoptotic stimuli. EMBO Mol. Med. *2*, 490–503. https://doi.org/10.1002/emmm.201000102.
43. Eustaquio, T., Wang, C., Dugard, C.K., George, N.I., Liu, F., Slikker, W., Paule, M.G., Howard, P.C., and Paredes, A.M. (2018). Electron microscopy techniques employed to explore mitochondrial defects in the developing rat brain following ketamine treatment. Exp. Cell Res. *373*, 164–170. https://doi.org/10.1016/j.yexcr.2018.10.009.
44. Gerriets, V.A., Kishton, R.J., Nichols, A.G., Macintyre, A.N., Inoue, M., Ilkayeva, O., Winter, P.S., Liu, X., Priyadharshini, B., Slawinska, M.E., et al. (2015). Metabolic programming and PDHK1 control CD4+ T cell subsets and inflammation. J. Clin. Invest. *125*, 194–207. https://doi.org/10.1172/JCI76012.
45. Baek, G., Tse, Y.F., Hu, Z., Cox, D., Buboltz, N., McCue, P., Yeo, C.J., White, M.A., DeBerardinis, R.J., Knudsen, E.S., et al. (2014). MCT4 Defines a Glycolytic Subtype of Pancreatic Cancer with Poor Prognosis and Unique Metabolic Dependencies. Cell Rep. *9*, 2233–2249. https://doi.org/10.1016/j.celrep.2014.11.025.
46. Sonntag, K.-C., Ryu, W.-I., Amirault, K.M., Healy, R.A., Siegel, A.J., McPhie, D.L., Forester, B., and Cohen, B.M. (2017). Late-onset Alzheimer's disease is associated with inherent changes in bioenergetics profiles. Sci. Rep. *7*, 14038. https://doi.org/10.1038/s41598-017-14420-x.
47. Ingold, I., Berndt, C., Schmitt, S., Doll, S., Poschmann, G., Buday, K., Roveri, A., Peng, X., Porto Freitas, F., Seibt, T., et al. (2018). Selenium Utilization by GPX4 Is Required to Prevent Hydroperoxide-Induced Ferroptosis. Cell *172*, 409–422.e21. https://doi.org/10.1016/j.cell.2017.11.048.
48. Dixon, S.J., and Olzmann, J.A. (2024). The cell biology of ferroptosis. Nat. Rev. Mol. Cell Biol. *25*, 424–442. https://doi.org/10.1038/s41580-024-00703-5.
49. Friedmann Angeli, J.P., Schneider, M., Proneth, B., Tyurina, Y.Y., Tyurin, V.A., Hammond, V.J., Herbach, N., Aichler, M., Walch, A., Eggenhofer, E., et al. (2014). Inactivation of the ferroptosis regulator Gpx4 triggers

acute renal failure in mice. Nat. Cell Biol. *16*, 1180–1191. https://doi.org/10.1038/ncb3064.

50. Doll, S., Proneth, B., Tyurina, Y.Y., Panzilius, E., Kobayashi, S., Ingold, I., Irmler, M., Beckers, J., Aichler, M., Walch, A., et al. (2017). ACSL4 dictates ferroptosis sensitivity by shaping cellular lipid composition. Nat. Chem. Biol. *13*, 91–98. https://doi.org/10.1038/nchembio.2239.

51. Mishima, E., Ito, J., Wu, Z., Nakamura, T., Wahida, A., Doll, S., Tonnus, W., Nepachalovich, P., Eggenhofer, E., Aldrovandi, M., et al. (2022). A non-canonical vitamin K cycle is a potent ferroptosis suppressor. Nature *608*, 778–783. https://doi.org/10.1038/s41586-022-05022-3.

52. Sun, K.H., De Pablo, Y., Vincent, F., and Shah, K. (2008). Deregulated Cdk5 promotes oxidative stress and mitochondrial dysfunction. J. Neurochem. *107*, 265–278. https://doi.org/10.1111/j.1471-4159.2008.05616.x.

53. Maestre, C., Delgado-Esteban, M., Gomez-Sanchez, J.C., Bolaños, J.P., and Almeida, A. (2008). Cdk5 phosphorylates Cdh1 and modulates cyclin B1 stability in excitotoxicity. EMBO J. *27*, 2736–2745. https://doi.org/10.1038/emboj.2008.195.

54. Telang, S., Clem, B.F., Klarer, A.C., Clem, A.L., Trent, J.O., Bucala, R., and Chesney, J. (2012). Small molecule inhibition of 6-phosphofructo-2-kinase suppresses t cell activation. J. Transl. Med. *10*, 95. https://doi.org/10.1186/1479-5876-10-95.

55. Chang, H.H., Cheng, Y.C., Tsai, W.C., and Chen, Y. (2020). PSMB8 inhibition decreases tumor angiogenesis in glioblastoma through vascular endothelial growth factor A reduction. Cancer Sci. *111*, 4142–4153. https://doi.org/10.1111/cas.14625.

56. Becher, B., Spath, S., and Goverman, J. (2017). Cytokine networks in neuroinflammation. Nat. Rev. Immunol. *17*, 49–59. https://doi.org/10.1038/nri.2016.123.

57. Dorrity, T.J., Shin, H., Wiegand, K.A., Aruda, J., Closser, M., Jung, E., Gertie, J.A., Leone, A., Polfer, R., Culbertson, B., et al. (2023). Long 3′UTRs predispose neurons to inflammation by promoting immunostimulatory double-stranded RNA formation. Sci. Immunol. *8*, eadg2979. https://doi.org/10.1126/sciimmunol.adg2979.

58. Merkler, D., Vincenti, I., Masson, F., and Liblau, R.S. (2022). Tissue-resident CD8 T cells in central nervous system inflammatory diseases: present at the crime scene and …guilty. Curr. Opin. Immunol. *77*, 102211. https://doi.org/10.1016/j.coi.2022.102211.

59. Martinez, P., Patel, H., You, Y., Jury, N., Perkins, A., Lee-Gosselin, A., Taylor, X., You, Y., Viana Di Prisco, G., Huang, X., et al. (2022). Bassoon contributes to tau-seed propagation and neurotoxicity. Nat. Neurosci. *25*, 1597–1607. https://doi.org/10.1038/s41593-022-01191-6.

60. Yacoubian, T.A., Fang, Y.D., Gerstenecker, A., Amara, A., Stover, N., Ruffrage, L., Collette, C., Kennedy, R., Zhang, Y., Hong, H., et al. (2023). Brain and Systemic Inflammation in De Novo Parkinson's Disease. Mov. Disord. *38*, 743–754. https://doi.org/10.1002/mds.29363.

61. Komura, H., Kakio, S., Sasahara, T., Arai, Y., Takino, N., Sato, M., Satomura, K., Ohnishi, T., Nabeshima, Y.I., Muramatsu, S.I., et al. (2019). Alzheimer Aβ Assemblies Accumulate in Excitatory Neurons upon Proteasome Inhibition and Kill Nearby NAKα3 Neurons by Secretion. iScience *13*, 452–477. https://doi.org/10.1016/j.isci.2019.01.018.

62. Xie, W., Li, X., Li, C., Zhu, W., Jankovic, J., and Le, W. (2010). Proteasome inhibition modeling nigral neuron degeneration in Parkinson's disease. J. Neurochem. *115*, 188–199. https://doi.org/10.1111/j.1471-4159.2010.06914.x.

63. Li, Z., Arnaud, L., Rockwell, P., and Figueiredo-Pereira, M.E. (2004). A single amino acid substitution in a proteasome subunit triggers aggregation of ubiquitinated proteins in stressed neuronal cells. J. Neurochem. *90*, 19–28. https://doi.org/10.1111/j.1471-4159.2004.02456.x.

64. Bedford, L., Hay, D., Devoy, A., Paine, S., Powe, D.G., Seth, R., Gray, T., Topham, I., Fone, K., Rezvani, N., et al. (2008). Depletion of 26S Proteasomes in Mouse Brain Neurons Causes Neurodegeneration and Lewy-Like Inclusions Resembling Human Pale Bodies. J. Neurosci. *28*, 8189–8198. https://doi.org/10.1523/JNEUROSCI.2218-08.2008.

65. Hsieh, Y.C., Augur, Z.M., Arbery, M., Ashour, N., Barrett, K., Pearse, R.V., Tio, E.S., Duong, D.M., Felsky, D., De Jager, P.L., et al. (2024). Person-specific differences in ubiquitin-proteasome mediated proteostasis in human neurons. Alzheimers Dement. *20*, 2952–2967. https://doi.org/10.1002/alz.13680.

66. Ciechanover, A., and Brundin, P. (2003). The Ubiquitin Proteasome System in Neurodegenerative Diseases: sometimes the chicken, sometimes the egg. Neuron *40*, 427–446. https://doi.org/10.1016/S0896-6273(03)00606-8.

67. McKinnon, C., and Tabrizi, S.J. (2014). The Ubiquitin-Proteasome System in Neurodegeneration. Antioxid. Redox Signal. *21*, 2302–2321. https://doi.org/10.1089/ars.2013.5802.

68. Simons, M., Levin, J., and Dichgans, M. (2023). Tipping points in neurodegeneration. Neuron *111*, 2954–2968. https://doi.org/10.1016/j.neuron.2023.05.031.

69. Heink, S., Ludwig, D., Kloetzel, P.-M., and Krüger, E. (2005). IFN-γ--induced immune adaptation of the proteasome system is an accelerated and transient response. Proc. Natl. Acad. Sci. USA *102*, 9241–9246. https://doi.org/10.1073/pnas.0501711102.

70. Kitamura, A., Maekawa, Y., Uehara, H., Izumi, K., Kawachi, I., Nishizawa, M., Toyoshima, Y., Takahashi, H., Standley, D.M., Tanaka, K., et al. (2011). A mutation in the immunoproteasome subunit PSMB8 causes autoinflammation and lipodystrophy in humans. J. Clin. Invest. *121*, 4150–4160. https://doi.org/10.1172/JCI58414.

71. Brehm, A., Liu, Y., Sheikh, A., Marrero, B., Omoyinmi, E., Zhou, Q., Montealegre, G., Biancotto, A., Reinhardt, A., Almeida de Jesus, A., et al. (2015). Additive loss-of-function proteasome subunit mutations in CANDLE/PRAAS patients promote type I IFN production. J. Clin. Invest. *125*, 4196–4211. https://doi.org/10.1172/JCI81260.

72. Honda-Ozaki, F., Terashima, M., Niwa, A., Saiki, N., Kawasaki, Y., Ito, H., Hotta, A., Nagahashi, A., Igura, K., Asaka, I., et al. (2018). Pluripotent Stem Cell Model of Nakajo-Nishimura Syndrome Untangles Proinflammatory Pathways Mediated by Oxidative Stress. Stem Cell Rep. *10*, 1835–1850. https://doi.org/10.1016/j.stemcr.2018.04.004.

73. Chocron, E.S., Munkácsy, E., Kim, H.S., Karpowicz, P., Jiang, N., Van Skike, C.E., DeRosa, N., Banh, A.Q., Palavicini, J.P., Wityk, P., et al. (2022). Genetic and pharmacologic proteasome augmentation ameliorates Alzheimer's-like pathology in mouse and fly APP overexpression models. Sci. Adv. *8*, eabk2252. https://doi.org/10.1126/sciadv.abk2252.

74. Almeida, A., Bolaños, J.P., and Moncada, S. (2010). E3 ubiquitin ligase APC/C-Cdh1 accounts for the Warburg effect by linking glycolysis to cell proliferation. Proc. Natl. Acad. Sci. USA *107*, 738–741. https://doi.org/10.1073/pnas.0913668107.

75. Pal, D., Torres, A.E., Stromberg, B.R., Messina, A.L., Dickson, A.S., De, K., Willard, B., Venere, M., and Summers, M.K. (2020). Chk1-mediated phosphorylation of Cdh1 promotes the SCFβTRCP-dependent degradation of Cdh1 during S-phase and efficient cell-cycle progression. Cell Death Dis. *11*, 298. https://doi.org/10.1038/s41419-020-2493-1.

76. Kirby, L., Jin, J., Cardona, J.G., Smith, M.D., Martin, K.A., Wang, J., Strasburger, H., Herbst, L., Alexis, M., Karnell, J., et al. (2019). Oligodendrocyte precursor cells present antigen and are cytotoxic targets in inflammatory demyelination. Nat. Commun. *10*, 3887. https://doi.org/10.1038/s41467-019-11638-3.

77. Falcão, A.M., van Bruggen, D., Marques, S., Meijer, M., Jäkel, S., Agirre, E., Samudyata, F., Floriddia, E.M., Vanichkina, D.P., Ffrench-Constant, C., et al. (2018). Disease-specific oligodendrocyte lineage cells arise in multiple sclerosis. Nat. Med. *24*, 1837–1844. https://doi.org/10.1038/s41591-018-0236-y.

78. Li, X., Chu, Y., Ma, R., Dou, M., Li, S., Song, Y., Lv, Y., and Zhu, L. (2022). Ferroptosis as a mechanism of oligodendrocyte loss and demyelination in experimental autoimmune encephalomyelitis. J. Neuroimmunol. *373*, 577995. https://doi.org/10.1016/j.jneuroim.2022.577995.

79. Jhelum, P., Santos-Nogueira, E., Teo, W., Haumont, A., Lenoël, I., Stys, P.K., and David, S. (2020). Ferroptosis Mediates Cuprizone-Induced Loss of Oligodendrocytes and Demyelination. J. Neurosci. *40*, 9327–9341. https://doi.org/10.1523/JNEUROSCI.1749-20.2020.
80. Minhas, P.S., Jones, J.R., Latif-Hernandez, A., Sugiura, Y., Durairaj, A.S., Wang, Q., Mhatre, S.D., Uenaka, T., Crapser, J., Conley, T., et al. (2024). Restoring hippocampal glucose metabolism rescues cognition across Alzheimer's disease pathologies. Science *385*, eabm6131. https://doi.org/10.1126/science.abm6131.
81. Byrns, C.N., Perlegos, A.E., Miller, K.N., Jin, Z., Carranza, F.R., Manchandra, P., Beveridge, C.H., Randolph, C.E., Chaluvadi, V.S., Zhang, S.L., et al. (2024). Senescent glia link mitochondrial dysfunction and lipid accumulation. Nature *630*, 475–483. https://doi.org/10.1038/s41586-024-07516-8.
82. Yao, Z., van Velthoven, C.T.J., Kunst, M., Zhang, M., McMillen, D., Lee, C., Jung, W., Goldy, J., Abdelhak, A., Aitken, M., et al. (2023). A high-resolution transcriptomic and spatial atlas of cell types in the whole mouse brain. Nature *624*, 317–332. https://doi.org/10.1038/s41586-023-06812-z.
83. Goldberg, K., Lobov, A., Antonello, P., Shmueli, M.D., Yakir, I., Weizman, T., Ulman, A., Sheban, D., Laser, E., Kramer, M.P., et al. (2025). Cell-autonomous innate immunity by proteasome-derived defence peptides. Nature *639*, 1032–1041. https://doi.org/10.1038/s41586-025-08615-w.
84. Peeters, K., Van Leemputte, F., Fischer, B., Bonini, B.M., Quezada, H., Tsytlonok, M., Haesen, D., Vanthienen, W., Bernardes, N., Gonzalez-Blas, C.B., et al. (2017). Fructose-1,6-bisphosphate couples glycolytic flux to activation of Ras. Nat. Commun. *8*, 922. https://doi.org/10.1038/s41467-017-01019-z.
85. Xu, K., Yin, N., Peng, M., Stamatiades, E.G., Shyu, A., Li, P., Zhang, X., Do, M.H., Wang, Z., Capistrano, K.J., et al. (2021). Glycolysis fuels phosphoinositide 3-kinase signaling to bolster T cell immunity. Science *371*, 405–410. https://doi.org/10.1126/science.abb2683.
86. Chang, S.C., Gopal, P., Lim, S., Wei, X., Chandramohan, A., Mangadu, R., Smith, J., Ng, S., Gindy, M., Phan, U., et al. (2022). Targeted degradation of PCNA outperforms stoichiometric inhibition to result in programed cell death. Cell Chem. Biol. *29*, 1601–1615.e7. https://doi.org/10.1016/j.chembiol.2022.10.005.
87. Sosna, J., Voigt, S., Mathieu, S., Kabelitz, D., Trad, A., Janssen, O., Meyer-Schwesinger, C., Schütze, S., and Adam, D. (2013). The proteases HtrA2/Omi and UCH-L1 regulate TNF-induced necroptosis. Cell Commun. Signal. *11*, 76. https://doi.org/10.1186/1478-811X-11-76.
88. Giuliano, C.J., Lin, A., Girish, V., and Sheltzer, J.M. (2019). Generating Single Cell–Derived Knockout Clones in Mammalian Cells with CRISPR/Cas9. Curr. Protoc. Mol. Biol. *128*, e100. https://doi.org/10.1002/cpmb.100.
89. Platt, R.J., Chen, S., Zhou, Y., Yim, M.J., Swiech, L., Kempton, H.R., Dahlman, J.E., Parnas, O., Eisenhaure, T.M., Jovanovic, M., et al. (2014). CRISPR-Cas9 Knockin Mice for Genome Editing and Cancer Modeling. Cell *159*, 440–455. https://doi.org/10.1016/j.cell.2014.09.014.
90. Dobin, A., Davis, C.A., Schlesinger, F., Drenkow, J., Zaleski, C., Jha, S., Batut, P., Chaisson, M., and Gingeras, T.R. (2013). STAR: ultrafast universal RNA-seq aligner. Bioinformatics *29*, 15–21. https://doi.org/10.1093/bioinformatics/bts635.
91. Liao, Y., Smyth, G.K., and Shi, W. (2014). featureCounts: an efficient general purpose program for assigning sequence reads to genomic features. Bioinformatics *30*, 923–930. https://doi.org/10.1093/bioinformatics/btt656.
92. Love, M.I., Huber, W., and Anders, S. (2014). Moderated estimation of fold change and dispersion for RNA-seq data with DESeq2. Genome Biol. *15*, 550. https://doi.org/10.1186/s13059-014-0550-8.
93. Durinck, S., Spellman, P.T., Birney, E., and Huber, W. (2009). Mapping identifiers for the integration of genomic datasets with the R/Bioconductor package biomaRt. Nat. Protoc. *4*, 1184–1191. https://doi.org/10.1038/nprot.2009.97.
94. Yu, G., Wang, L.-G., Han, Y., and He, Q.-Y. (2012). clusterProfiler: an R Package for Comparing Biological Themes Among Gene Clusters. OMICS *16*, 284–287. https://doi.org/10.1089/omi.2011.0118.
95. Link, A.J., Vink, M.K.S., and Tirrell, D.A. (2007). Preparation of the functionalizable methionine surrogate azidohomoalanine via copper-catalyzed diazo transfer. Nat. Protoc. *2*, 1879–1883. https://doi.org/10.1038/nprot.2007.268.
96. Dieterich, D.C., Link, A.J., Graumann, J., Tirrell, D.A., and Schuman, E.M. (2006). Selective identification of newly synthesized proteins in mammalian cells using bioorthogonal noncanonical amino acid tagging (BONCAT). Proc. Natl. Acad. Sci. USA *103*, 9482–9487. https://doi.org/10.1073/pnas.0601637103.
97. Wang, Z., Fu, W., Huo, M., He, B., Liu, Y., Tian, L., Li, W., Zhou, Z., Wang, B., Xia, J., et al. (2021). Spatial-resolved metabolomics reveals tissue-specific metabolic reprogramming in diabetic nephropathy by using mass spectrometry imaging. Acta Pharm. Sin. B *11*, 3665–3677. https://doi.org/10.1016/j.apsb.2021.05.013.
98. Romanelli, E., Merkler, D., Mezydlo, A., Weil, M.-T., Weber, M.S., Nikić, I., Potz, S., Meinl, E., Matznick, F.E.H., Kreutzfeldt, M., et al. (2016). Myelinosome formation represents an early stage of oligodendrocyte damage in multiple sclerosis and its animal model. Nat. Commun. *7*, 13275. https://doi.org/10.1038/ncomms13275.
99. Chan, K.Y., Jang, M.J., Yoo, B.B., Greenbaum, A., Ravi, N., Wu, W.-L., Sánchez-Guardado, L., Lois, C., Mazmanian, S.K., Deverman, B.E., et al. (2017). Engineered AAVs for efficient noninvasive gene delivery to the central and peripheral nervous systems. Nat. Neurosci. *20*, 1172–1179. https://doi.org/10.1038/nn.4593.
100. Engler, J.B. (2025). Tidyplots empowers life scientists with easy code-based data visualization. Imeta *4*, e70018. https://doi.org/10.1002/imt2.70018.

STAR★METHODS

KEY RESOURCES TABLE

REAGENT or RESOURCE	SOURCE	IDENTIFIER
Antibodies		
4-hydroxy-2-nonenal	Abcam	ab46545, RRID: AB_722490
ACSL4	Santa Cruz	sc-365230, RRID: AB_10843105
Acti-Stain	Cytoskeleton	PHGD1
BD Horizon™ Fixable Viability Stain 700	BD Bioscience	564997, RRID: AB_2869637
CC1	Merck	OP80, RRID: AB_2057371
CD4 BV711	BioLegend	100447, RRID: AB_2564586
CD8α BV711	BioLegend	100748, RRID: AB_2562100
CD8α BV785	BioLegend	100750, RRID: AB_2562610
CD11b BUV395	BD Bioscience	563553, RRID: AB_2738276
CD11c PE/Cy7	BioLegend	117318, RRID: AB_493568
CD19 BUV661	BD Bioscience	612971, RRID: AB_2870243
CD31	BioLegend	102502, RRID: AB_312909
CD45 APC/Cy7	BioLegend	103116, RRID: AB_312981
CD45 FITC	BioLegend	103108, RRID: AB_312973
CD68 BV785	BioLegend	137035, RRID: AB_2860684
CD80 FITC	BioLegend	104706, RRID: AB_313126
CD86 BUV496	BD Bioscience	750437, RRID: AB_2874600
CD163 PE/Cy7	BioLegend	155319, RRID: AB_2890710
CDH1	Merck	MABT1323, RRID: NA
CDK5	Cell Signaling	2506, RRID: NA
CX3CR1 PB	BioLegend	149038, RRID: AB_2632857
F4/80 BV421	BioLegend	123137, RRID: AB_2563102
FSP1	Santa Cruz	sc-377120, RRID: AB_2893240
GAPDH	Cell Signaling	2118, RRID: AB_561053
GFAP	Millipore	AB5541, RRID: AB_177521
GFP	Abcam	ab13970, RRID: AB_300798
GPX4	Abcam	ab125066, RRID: AB_10973901
HuC/D	Invitrogen	A-21271, RRID: AB_221448
IBA1	Synaptic Systems	234308, RRID: AB_2924932
Ig chicken AF 488	Jackson Immuno	703-545-155, RRID: AB_2340375
Ig chicken AF 647	Jackson Immuno	703-606-155, RRID: AB_2340380
Ig chicken Cy3	Abcam	ab97145, RRID: AB_10679516
Ig mouse AF 647	Jackson Immuno	715-605-151, RRID: AB_2340863
Ig mouse AF 405	Abcam	ab175658, AB_2687445
Ig rabbit AF 488	Abcam	ab150073, RRID: AB_2636877
Ig rabbit AF 555	Abcam	ab150074, RRID: AB_2636997
Ig rabbit AF 647	Abcam	ab150075, RRID: AB_2752244
Ig mouse HRP	LI-COR	926-80010, RRID: AB_2721263
Ig rabbit HRP	LI-COR	926-80011, RRID: AB_2721264
IFN-γ BV785	BioLegend	505837, RRID: AB_11219004
IL17 APC	BioLegend	506916, RRID: AB_536017
iNOS	Abcam	ab115819, RRID: AB_10898933
I-A/I-E BUV805	BD Bioscience	748844, RRID: AB_2873247

(*Continued on next page*)

Continued

REAGENT or RESOURCE	SOURCE	IDENTIFIER
Ly6C PE	BioLegend	128008, RRID: AB_1186132
Ly6G PerCP-Cy5.5	BioLegend	127616, RRID: AB_1877271
MAP2	Abcam	ab5392, RRID: AB_2138153
MHC I PE	BioLegend	107601, RRID: AB_313316
NeuN	Abcam	EPR12763, RRID: AB_2732785
NeuN	Merck	ABN90, RRID: AB_11205592
NG2	Thermo Fisher Scientific	MA5-24247, RRID: AB_2606388
NK1.1 APC	BioLegend	108710, RRID: AB_313396
P2RY12 PE	BioLegend	848004, RRID: AB_2721644
PFKFB3	Abcam	Ab181861, RRID: AB_3095816
pSTAT1	Cell Signaling	9167, RRID: AB_561284
STAT1	Cell Signaling	9172, RRID: AB_2198300
Ubiquitin linkage specific K48	Abcam	Ab140601, RRID: AB_2783797
PSMA2	Cell Signaling	2455, RRID: AB_2171400
PSMB5	Thermo Fisher Scientific	PA1-977, RRID: AB_2172052
PSMB5	Abcam	Ab3330; RRID: AB_303709
PSMB8	Abcam	Ab3329, RRID: AB_303708
PSMB8	proteintech	66759-1, RRID: AB_2282105
RFP	Thermo Fisher Scientific	R10367, RRID: AB_2315269
TCRβ BUV737	BD Bioscience	612821, RRID: AB_2870145
TREM2	R&D Systems	FAB17291A, RRID: AB_884527
Vinculin	Merck	V9131, RRID: AB_477629
Zombie Green	BioLegend	423112
Zombie Yellow	BioLegend	423104
Biological samples		
Brain biopsies from healthy individuals and pwMS.	Brain biopsies at the University Medical Center Hamburg-Eppendorf	N/A
Postmortem brain autopsies from healthy individuals and pwMS.	UK Biobank	https://www.ukbiobank.ac.uk/
Chemicals, peptides, and recombinant proteins		
2-Desoxy-D-Glucose	Merck	D8375
CDK5 inhibitor 20-223	MedChemExpress	HY-123772
Co-enzyme Q10	Merck	07386
Ferrostatin-1	MedChemExpress	HY-100579
Glutamate	Merck	106445
GM-CSF	Thermo Fisher Scientific	300-03
IL-1β	InvivoGen	rcyc-hil1b
IL-17	InvivoGen	rcyc-htnfa
Interferon-α	Miltenyi Biotec	130-134-235
Interferon-γ	Thermo Fisher Scientific	315-05
Liproxstatin-1	MedChemExpress	HY-12726
MG-132 (Z-Leu-Leu-Leu-al)	Biotechne	6033
Oligomycin	Merck	495455
ONX-0914 (PR-957)	MedChemExpress	HY-13207
Pfk-158	MedChemExpress	HY-12203
Roscovitine	MedChemExpress	HY-30237
Rotenone	Merck	R8875
RSL-3	Merck	SML2234
TNFα	InvivoGen	rcyc-htnfa

(*Continued on next page*)

Continued

REAGENT or RESOURCE	SOURCE	IDENTIFIER
Critical commercial assays		
CellROX green reagent	Thermo Fisher Scientific	C10444
CellTiterGlo	Promega	G7570
Glucose-Glo	Promega	J6021
GSH-Glo	Promega	V6911
Image-iT	Thermo Fisher Scientific	C10445
Lactate-Glo	Promega	J5021
Lenti-X concentrator	Takara	631232
NADPH/NADPH-Glo	Promega	G9081
RealTime-Glo	Promega	G9711
Seahorse XF Glycolytic Rate Assay Kit	Agilent	103344-100
Seahorse XF Cell Mito Stress test Kit	Agilent	103015-100
Suc-LLVY-AMC substrate	Bachem	#4011369
Deposited data		
Raw and analyzed data	This paper	GSE279705
Raw and analyzed data	This paper	GSE279706
Raw and analyzed data	This paper	GSE279707
Experimental models: Cell lines		
Hybridoma cells	Sosna et al.[87]	N/A
Primary neuronal cortical cultures	This paper	N/A
Experimental models: Organisms/strains		
Biozzi ABH	Envigo	RRID: IMSR_JAX:027904
C57BL/6J WT	The Jackson Laboratory	RRID: IMSR_JAX:000664
LSL-R26-MetRS*	The Jackson Laboratory	RRID: IMSR_JAX:028071
Psmb8-flox	Elke Krüger, University of Greifswald	N/A
Rosa26-LSL-Cas9	The Jackson Laboratory	RRID: IMSR_JAX:026175
SJL/JRj	Janvier Labs	RRID:IMSR_JAX:000686
Snap25-Cre	The Jackson Laboratory	RRID: IMSR_JAX:023525
Oligonucleotides		
mmPfkfb3_guide1_fwd_BsmBI	CACCGAGCCCCACCATCACAATCA	This paper
mmPfkfb3_guide1_rev_BsmBI	aaacTGATTGTGATGGTGGGGCTC	This paper
mmPfkfb3_guide2_fwd_BsmBI	CACCGTGGAGATGTAAGTCTTACCC	This paper
mmPfkfb3_guide2_rev_BsmBI	aaacGGGTAAGACTTACATCTCCAC	This paper
mmPfkfb3_guide3_fwd_BsmBI	CACCGTGTGGGAGAGTATCGGCGTG	This paper
mmPfkfb3_guide3_rev_BsmBI	aaacCACGCCGATACTCTCCCACAC	This paper
mmPfkfb3_guide4_fwd_BsmBI	CACCGtggcttcctcattgtcaggg	This paper
mmPfkfb3_guide4_rev_BsmBI	aaaccccctgacaatgaggaagccaC	This paper
mmPfkfb3_guide2_fwd_LguI	accGTGGAGATGTAAGTCTTACCC	This paper
mmPfkfb3_guide2_rev_LguI	aacGGGTAAGACTTACATCTCCAC	This paper
mmPfkfb3_guide3_fwd_LguI	accGTGTGGGAGAGTATCGGCGTG	This paper
mmPfkfb3_guide3_rev_LguI	aacCACGCCGATACTCTCCCACAC	This paper
ntc_guide1_fwd_LguI	accGAAAACGGCTCGATCGGTGAT	This paper
ntc_guide1_rev_LguI	aacATCACCGATCGAGCCGTTTTC	This paper
mmPsmb5_fwd_AgeI	TAGACCGGTATGGCGCTGGCTAGCGTGTTG	This paper
mmPsmb5_rev_XbaI	TAGTCTAGAGGGGACAGATACACTACT GTACTTG	This paper
mmPsmb8_fwd_AgeI	TAGACCGGTATGGCGTTACTGGATCTGTGCG	This paper

(*Continued on next page*)

Continued

REAGENT or RESOURCE	SOURCE	IDENTIFIER
mmPsmb8_rev_XbaI	TAGTCTAGACAGAGCGGCCTCTCCGTACTT	This paper
mmIfng_fwd_AgeI	TAGCGTACGATGAACGCTACACACTGCATCTTGG	This paper
mmIfng_rev_XbaI	TAGTCTAGAGCAGCGACTCCTTTTCCGCTTC	This paper
mmPfkfb3_fwd_AgeI	TAGACCGGTATGCCGTTGGAACTGACCCAGA	This paper
mmPfkfb3_rev_XbaI	TAGTCTAGAGTAAGGAGAAAACTTTGAAAAAATGTGACAG	This paper
mmCdh1_fwd_AgeI	TAGACCGGTATGGGAGCCCGGTGCCGC	This paper
mmCdh1_rev_XbaI	TAGTCTAGAGTCGTCCTCACCACCGCCG	This paper
Recombinant DNA		
pMDLg/pRRE	Addgene	RRID: Addgene_12251
pRSV-Re	Addgene	RRID: Addgene_12253
pMDLg/pRRE	Addgene	RRID: Addgene_12259
mu-IFNg-pCIneo	Addgene	RRID: Addgene_163517
Lenti-Cas9-gRNA-GFP	Giuliano et al.[88]	RRID: Addgene_124770
AAV:ITR-U6-sgRNA(backbone)-hSyn-Cre-2A-EGFP-KASH-WPRE-shortPA-ITR	Platt et al.[89]	RRID: Addgene_60231
L21-hSyn-mScarlet	This paper	N/A
L21-hSyn-EGFP	This paper	N/A
L21-CMV-mmIfng-P2a-mScarlet	This paper	N/A
L21-hSyn-mmCdh1-P2a-mScarlet	This paper	N/A
L21-hSyn-mmIfng-P2a-EGFP	This paper	N/A
L21-hSyn-mmPfkfb3-P2a-mScarlet	This paper	N/A
L21-hSyn-mmPsmb5-P2a-mScarlet	This paper	N/A
L21-hSyn-mmPsmb5-P2a-EGFP	This paper	N/A
L21-hSyn-mmPsmb8-P2a-mScarlet	This paper	N/A
L21-hSyn-mmPsmb8-P2a-EGFP	This paper	N/A
AAV:ITR-U6-ntc-hSyn-Cre-2A-EGFP-KASH-WPRE-shortPA-ITR	This paper	N/A
AAV:ITR-U6-Pfkfb3-g1-hSyn-Cre-2A-EGFP-KASH-WPRE-shortPA-ITR	This paper	N/A
AAV:ITR-U6-Pfkfb3-g2-hSyn-Cre-2A-EGFP-KASH-WPRE-shortPA-ITR	This paper	N/A
Software and algorithms		
R	https://www.r-project.org/	https://www.r-project.org/
STAR	Dobin et al.[90]	https://github.com/alexdobin/STAR
featureCounts	Liao et al.[91]	https://subread.sourceforge.net/
DESeq2	Love et al.[92]	https://doi.org/10.18129/B9.bioc.DESeq2
biomaRT	Durinck et al.[93]	https://doi.org/10.18129/B9.bioc.biomaRt
clusterProfiler	Yu et al.[94]	https://doi.org/10.18129/B9.bioc.clusterProfiler
Proteome Discoverer 2.4	Thermo Fisher Scientific	N/A

EXPERIMENTAL MODEL AND STUDY PARTICIPANT DETAILS

Human subjects

Specimens used for histopathology were obtained from brain biopsies or postmortem autopsies of individuals with MS-typical changes, as described by board-certified neuropathologists. These individuals had an MS diagnosis determined by board-certified neurologists. The specimens were anonymized (cohort characteristics are provided in Table S1). The use of patient specimens for research after anonymization was in accordance with local ethical standards and regulations at the University Medical Center Hamburg-Eppendorf. As human tissue could no longer be traced back to an individual, the analyses did not constitute a "research project on humans" within the meaning of § 9 para. 2 of the Hamburg Chamber of Commerce Act for the Health Professions and, therefore, did not require consultation in accordance with § 15 para. 1 of the Professional Code of Conduct for Physicians in Hamburg.

Animals

All mice (C57BL/6J WT from The Jackson Laboratory, SJL/JRj WT from Janvier Labs, C57BL/6J *Snap25-Cre* × *Psmb8*$^{flox/flox}$,[29] C57BL/6J *Snap25-Cre* × LSL-R26-MetRS*,[37] C57BL/6J Rosa26-LSL-Cas9,[89] Biozzi ABH from Envigo) were housed under specific pathogen-free conditions in the central animal facilities of the University Medical Center Hamburg-Eppendorf (UKE) and the University Hospital of the LMU Munich. Adult mice (6–20 weeks old) of both sexes were used, and all experiments mice were sex- and age-matched. We did not observe sex-specific differences in any of the experiments; therefore, data from both sexes were reported together. All animal care and experimental procedures were conducted according with institutional guidelines and met the requirements of the German legal authorities. Ethical approvals were obtained from the State Authorities of Hamburg and Bavaria, Germany (approval No. 41/22).

Cells

Mouse primary neurons

For primary cortical cultures, we euthanized pregnant C57BL/6J, or LSL-Cas9 mice. We isolated the cortex at the embryonic day 15.5, dissociated, and plated cells at a density of 6 × 10^4 cells per 1 cm^2 on poly-D-lysine-coated wells (5 μM; Sigma-Aldrich). Unless otherwise stated, cells were maintained in PNGM (Lonza) at 37°C, 5% CO_2, and 98% relative humidity. Cultures were used for experiments after 14-23 days in vitro (d.i.v.). If indicated, we applied 100 ng mL^{-1} IFNγ, IL-17, TNFα, GM-CSF, IL-1β at 11-14 d.i.v for 3 or 7 consecutive days. Subsequent stimulations were performed at 14-17 d.i.v. as described in the respective figure legends (all compounds and respective concentrations are provided in the section "Compounds and chemicals").

Rat hybridoma cells

Rat hybridoma cells[87] were cultured under non-permissive conditions [37°C, 5% CO_2, RPMI 1640 Medium, GlutaMAX Supplement (Thermo Fisher Scientific, #61870044) with 10% fetal calf serum (Thermo Fisher Scientific, #10500-064), 1% penicillin and streptomycin (Thermo Fisher Scientific, #15070063), 1 mM Na-Pyruvate (Thermo Fisher Scientific, #11360-039), 50 μM beta-mercaptoethanol (Thermo Fisher Scientific, #31350-010)] in uncoated, vented cell culture flasks for suspension cells (Sarstedt). Cell pellets were collected and lysed as controls for immunoblots as they expressed all 6 catalytic active beta-subunits of the proteasome.

METHOD DETAILS

Vector construction

Mouse *Psmb5*, *Psmb8*, *Pfkfb3*, and *Cdh1* were amplified from lymph node cDNA using the respective primers that are provided in the key resources table. The hybridization temperature was 65°C. Mouse *Ifng* was amplified from the publicly available mu-IFNg-pCIneo (mu-IFNg-pCIneo was a gift from Thomas Weber (Addgene plasmid #163517; http://n2t.net/addgene:163517; RRID:Addgene_163517)) using the respective primers that are provided in the key resources table. The hybridization temperature was 65°C. PCR amplification products were digested with the restriction enzymes AgeI and XbaI for 16 hours at 37°C and were ligated into a customized lentiviral backbone with a human synapsin (hSyn) promoter (*Psmb5, Psmb8, Pfkfb3*) for neuron-specific expression or a CMV promoter (*Ifng*) for ubiquitous expression. The expression plasmid also contained either mScarlet or EGFP after a P2a domain to assess transduction efficacy. For inducing CRISPR knockouts of *Pfkfb3* (*mmPfkfb3* oligo pairs 1–4) in neuronal cultures, we first annealed forward and reverse oligos, which were then digested with BsmBI for 6 hours on 37°C and subsequently ligated into either Lenti-Cas9-gRNA-GFP (Lenti-Cas9-gRNA-GFP was a gift from Jason Sheltzer, Addgene plasmid #124770; http://n2t.net/addgene:124770; RRID:Addgene_124770) or a customized lentiviral backbone based on lentiGuide Puro (lentiGuide-Puro was a gift from Feng Zhang, Addgene plasmid #52963). This backbone consists of Cre recombinase under the control of the hSyn promoter and a guideRNA cassette under the control of a human U6 promoter. The Lenti-Cas9-*Pfkfb3*-GFP constructs were transfected (see below for detailed description) in N2a cells to confirm the knockouts on protein levels. For inducing CRISPR knockouts of *Pfkfb3* (*mmPfkfb3* oligo pairs 2-3) in LSL-Cas9 mice, forward and reverse oligos were first annealed and digested with LguI for 6 hours at 37°C, then ligated either in the AAV:ITR-U6-sgRNA(backbone)-hSyn-Cre-2A-EGFP-KASH-WPRE-shortPA-ITR. AAV:ITR-U6-sgRNA(backbone)-hSyn-Cre-2A-EGFP-KASH-WPRE-shortPA-ITR was a gift from Feng Zhang (Addgene plasmid #60231; http://n2t.net/addgene:60231; RRID:Addgene_60231). A non-targeted control (ntc) was ligated into the same vector as a control. All final products were confirmed via Sanger sequencing. For all lentiviral overexpression experiments, lentiviral mScarlet or EGFP overexpression constructs were used as controls.

Lentiviral production and transduction

To produce lentiviruses, we first transfected HEK293T cells with 10 μg expression plasmid, 10 μg pMDLg/pRRE, 5 μg pRSV-Re, 2 μg pMD2.G. The pMDLg/pRRE plasmid was a gift from Didier Trono (Addgene #12251; http://n2t.net/addgene:12251; RRID: Addgene_12251), as were pRSV-Rev (Addgene #12253; http://n2t.net/addgene:12253; RRID: Addgene_12253) and pMD2.G (Addgene #12259; http://n2t.net/addgene:12259; RRID: Addgene_12259). Briefly, HEK293T cells were seeded with at 80% confluency in DMEM with glutamine and high glucose (Thermo Fisher Scientific, cat. no. 10569010). The following day, the plasmids were mixed in 1× HEPES buffered saline (HBS) and 125 mM $CaCl_2$ and were applied to the HEK293T cells for 6 hours. Afterwards, the medium was replaced, and 48 hours later, the supernatant was filtered through a 0.45 μm PES filter. Subsequently, we used the Lenti-X Concentrator (Takara, cat. no. 631232) according to the manufacturer's protocol to generate 20× concentrated lentiviruses in PBS. They were snap frozen, stored at –80°C, and used only after maximal one freeze-thaw cycle. Neurons were transduced at 7 d.i.v. with an 80-90% transduction efficacy (Figure S12A), visually confirmed by expression of a fluorescent protein. Control neurons were transduced an mScarlet-carrying lentivirus. The functionality of *Ifng* expression was confirmed by the increased expression of the type II interferon downstream mediator, signal transducer and activator of transcription 1 (STAT1), along with its activated phosphorylated form (Figures S12B and S12C).

Neuronal proteome analysis in LSL-R26-MetRS* animals

LSL-R26-MetRS* mice[37] were crossed with *Snap25*-Cre mice to enable neuron-specific proteome tagging during acute EAE. LSL-R26-MetRS* littermates lacking Cre-recombinase served as controls. To label the nascent neuronal proteome, EAE animals and healthy controls were treated with the non-canonical amino acid azidonorleucine (ANL)[95] at a dose of 2 μmol g^{-1} body weight per day by intraperitoneal injections. In EAE animals, ANL treatment was administered from day 8 to day 14 post-immunization, targeting the acute stage of the disease. Animals were sacrificed at day 15 post-immunization, and spinal cord tissue was harvested for bioorthogonal non-canonical amino-acid tagging (BONCAT).[96] For the enrichment of ANL-labelled proteins, the Click-iT® Protein Enrichment Kit (Invitrogen, cat. no. C10416) was used according to the manufacturer's instructions. In brief, spinal cord lysates were incubated with an alkyne agarose resin and a copper-based catalyst to covalently capture ANL-labelled proteins on the resin. After overnight incubation, stringent washes were performed to remove non-specifically bound proteins. On-resin tryptic digestion was then conducted to release ANL-labeled peptides, which were subsequently desalted and concentrated for mass spectrometry analysis.

For mass spectroscopy, peptides were resolved in 3% acetonitrile/0.2% TFA, and a 100 ng peptide mix from each sample was used for LC-MS/MS analysis. The analyses were conducted on a Dionex UltiMate 3000 n-RSLC system (Thermo Fisher Scientific), connected to an Orbitrap Fusion™ Tribrid™ mass spectrometer (Thermo Fisher Scientific). Resolved peptides were loaded onto a C18 precolumn (3 μm RP18 beads, Acclaim, 0.075 × 20 mm), washed for 3 minutes at a flow rate of 6 μL min^{-1}, and separated on a 2 μm Pharmafluidics C18 analytical column at a flow rate of 300 nL min^{-1} via a linear 60-minute gradient from 97% MS buffer A (0.1% FA) to 32% MS buffer B (0.1% FA, 80% ACN), followed by a 30-minute gradient from 32% MS buffer B to 62% MS buffer B. The LC system was controlled using the Thermo Fisher Scientific SII software embedded in the Xcalibur software suite (version 4.3.73.11, Thermo Fisher Scientific). The effluent was electro-sprayed using a stainless-steel emitter (Thermo Fisher Scientific). The mass spectrometer was operated in the "top speed" mode via the Xcalibur software, enabling the automatic selection of as many doubly and triply charged peptides as possible within a 3-second time window, followed by their fragmentation. Peptide fragmentation was performed using higher-energy collisional dissociation (HCD), and the fragments were analyzed in the ion trap (HCD/IT). MS/MS raw data files were processed via Proteome Discoverer 2.4, with searches conducted against the murine UniProtKB/SwissProt protein database (release 2020_01) via the Sequest HT search machine. The following search parameters were applied: enzyme, trypsin; maximum missed cleavages, 1; fixed modification, carbamidomethylation (C); variable modification, oxidation (M); peptide tolerance, 7 ppm; MS/MS tolerance, 0.4 Da. The FDR was set to 1%.

For statistical analysis, missing normalized protein abundance values, representing levels below the detection limit, were replaced with zeros. Differences between experimental groups were assessed by protein-wise Mann-Whitney U test without correction for multiple-comparison. The *clusterProfiler* package[94] was used to calculate and visualize biological process gene ontology terms. Proteins significantly more abundant in Cre recombinase-expressing mice ("immunoprecipitation") compared Cre recombinase-negative control mice ("input") were included in the analysis.

Generation of mouse neuronal cultures with conditional knockouts

To generate *Pfkfb3*-cKO neurons, neuronal cultures from LSL-Cas9 mice were transduced at 7 d.i.v. with lentiviruses contained Cre recombinase under the control of a human synapsin (hSyn) promoter, along with the respective guide RNAs (see above for detailed description). For each gene, 4 guides were used to create pooled lentiviruses. Transduction efficacy was estimated visually at 80-90% (Figure S12D), as all LSL-Cas9 cells transduced with a Cre recombinase expressed EGFP. Neurons transduced with the same vectors containing non-targeted control gRNAs or gRNAs against LacZ served as controls. *Psmb8*-KO neurons were generated by transducing primary neurons from homozygous *Psmb8*-flox mice with a Cre recombinase-carrying AAV-PHP.eB after 7 d.i.v., using a multiplicity of infection (MOI) of 20,000 yielding a transduction efficacy of 80-90% (Figure S12E). AAV and lentiviral transductions did not elicit a type II interferon response themselves in our neuronal cell culture model (Figures S12F and S12G).

Compounds and chemicals

Compounds were added to primary neurons at the indicated time points specified in the respective figure legends. For cell viability assays following glutamate or RSL3 exposure, the compounds were added 5 hours before the stressors. For immunocytochemistry, compounds were added 30 minutes before the stressor application. For assessing cell death in PSMB5- or PSMB8-overexpressing neurons 14 days post- transfection, compounds were applied every other day. When indicated, 100 ng mL^{-1} IFNγ, IL-17, TNFα, GM-CSF, IL-1β were applied for 72 hours or 7 consecutive days. Unless otherwise stated, the following concentrations were used: 2 mM 2-Desoxy-D-Glucose; 50 nM CDK5 inhibitor 20-223; 6 μM coenzyme Q10; 10 μM ferrostatin-1; 50 μM glutamate; 100 ng mL^{-1} IFNγ; 1 μM liproxstatin-1; 1 μM MG-132; 10 μM oligomycin; 500 nM Pfk-158; 1 μM roscovitine; 0.5 μM rotenone; 6 μM RSL3.

Proteasome activity

β-subunit-specific proteasomal activity assay

To visualize the β-subunit-specific proteasomal activities of the 20S core particle, primary culture neurons were lysed with TSDG buffer (10 mM Tris pH 7.5, 10 mM NaCl, 25 mM KCl, 1 mM $MgCl_2$, 0.1 mM EDTA, 1 mM DTT, 2 mM ATP) *via* eight freeze-thaw cycles using a dry ice and ethanol bath to freeze and warm water to thaw the samples. After centrifugation for 10 minutes at 16,000 g at 4°C, concentration of soluble proteins in the supernatant was measured using ROTIQuant universal (Carl Roth, #0120.1) according to the manufacturer's instructions. 8 μg of protein was filled up with TSDG buffer and mixed with 0.5 μM Cy5-epoxomicin in a reaction volume of 20 μL. Cy5-epoxomicin (pan-proteasomal activity-based probe EMA475) assesses activity of all proteolytic β-subunits and does not differentiate between β5c and β5i activity due to very similar molecular weight of both β-subunits). The reaction mixture was incubated for 1 hour at 37°C. As an assay control rat hybridoma cells (which are abundant in constitutive 20S as well as immuno 20S proteolytic β-subunits) were incubated with or without 5 μM epoxomicin for 1 hour, 37°C prior to the incubation with activity-based probes. Samples were denatured in reducing solubilization buffer (50 mM Tris-HCl pH 6.8, 2% SDS, 100 mM DTT, 10% glycerol, 0.05% bromophenol blue; final concentrations) for 10 minutes at 70°C, samples were separated on a 12.5% Tris-Glycine gel in a Tris-glycine migration buffer. The activity was visualized on a Fusion FX7EDGE V0.7 Imager (Vilber Lourmat) using the appropriate filters (for Cy5: light capsule C640 and Filter F710). Following fluorescent visualization, activity gels were blotted onto PVDF membranes and further processed for conventional immunoblotting to proteasomal subunits and loading controls.

Proteasome complex activities

For further evaluation of chymotrypsin-like activity, after native lysis by freeze-thaw and protein quantification determination as described above, 8 μg of total protein from primary neuronal cell lysates were mixed with clear native loading buffer (50 mM Bis-Tris, pH 6.5, 50 mM NaCl, 10% glycerol, 0.05% bromophenol blue; final concentrations) and resolved by native PAGE using vertical native gels (Serva #43250.01) and clear native running buffer (50 mM BisTris, 50 mM Tricin, 0.4 mM ATP, 2 mM MgCl2, 0.5 mM DTT) without boiling the samples. After electrophoresis gels were incubated with 100 μM Suc-LLVY-AMC substrate (Bachem #4011369) in activity buffer (20 mM Tris base, pH 7.5, 5 mM $MgCl_2$, 2 mM ATP) for 20 minutes at 37°C. The chymotrypsin-like activity of proteasomal complexes could be visualized by measuring fluorescence applying a Capsule 365nm and F-450 interference filter using a FUSION FX07 (Vilber).

Immunoblot reprobes of activity gels

Following activity readout, protein transfer was performed in transfer buffer (0.25 M Tris base, 1.92 M glycine, 20% MeOH in H_2O) in a TransBlot Turbo System (BioRad). After the transfer, all proteins were visualized by ponceau staining. PVDF membranes (Millipore) were blocked (3% non-fat milk) prior to incubation with primary antibodies diluted in Superblock reagent (Thermo Fisher Scientific) or non-fat milk. Primary antibodies used were PSMB5 (1:1000), PSMB8 (1:1000). PSMA2 (1:1000). Binding was detected by incubation with HRP-coupled secondary antibodies (1:10,000-1:20,000, 3% nonfat milk). Furthermore, actin levels determined by conventional IB of the respective lysates were performed to indicate that the protein concentrations have been correctly adjusted. Protein expression was visualized with ECL SuperSignal (Thermo Fisher Scientific) according to manufacturer's instructions on a FUSION FX07 (Vilber). Activity gels and corresponding immunoblots were analyzed using software from FIJI. β-actin or Ponceau stainings of the same membrane are shown and were used as loading control and for densitometric normalization. Bands of the same membrane are shown, fine dashed black lines indicate, where bands were not adjacent to another on the membrane. Whole immunoblot membranes are provided in Data S1.

IFNγ ELISA

IFNγ levels were measured using a commercial enzyme-linked immunosorbent assay kit (ELISA MAX™ Deluxe Set Mouse IFN-γ, BioLegend), following the manufacturer's protocol. Briefly, 96-well ELISA plates were coated with Mouse IFNγ ELISA MAX™ Capture Antibody and incubated overnight at 4°C. The following day, the plates were washed with Wash Buffer (PBS 0.05% Tween-20), and non-specific binding sites were blocked with Assay Diluent A for 1 hour at room temperature (RT). Samples diluted 1:100 in Assay Diluent A and serial diluted IFNγ standards were added to the wells (100 μl per well) and incubated for 2 hours at RT in the dark on a plate shaker. After washing, 100 μl of Mouse IFNγ ELISA MAX™ Detection Antibody were added to each well and incubated for 1 hour at RT. Plates were washed again, followed by the addition of 100 μl Avidin-HRP solution, which incubated for 30 minutes at RT. After a final wash, 100 µl of Substrate Solution F were added and incubated in the dark for 10 minutes. The reaction was stopped by adding 100 µl of H_2SO_4. Absorbance was measured at 450 nm and 570 nm using a plate reader (Tecan). The absorbance at 570 nm served as reference wavelength subtracted from the absorbance at 450 nm.

Cell viability assays

To measure glutamate- and RSL3-induced cell death, we mixed RealTime-Glo (Promega, cat. no. G9711) MT cell viability substrate and NanoLuc Enzyme and added it to neuronal cultures, incubated them for 5 hours to equilibrate the luminescence signal before treatments were applied (details on compounds and concentrations are provided in the section ‘‘Compounds and chemicals’’). Toxicity was estimated after the application of 50 µM glutamate or 6 µM RSL3. We recorded luminescence using a Spark 10M multimode microplate reader (Tecan) at 37°C and 5% CO_2, every 30 min, over 20-24 hours. We used at least four technical replicates per condition. For analysis, every well's data point was normalized to its last value before the stressor was applied and subsequently normalized to the mean of the control wells at every time point, controlling for well-to-well seeding variability. We performed statistical analysis by comparing the endpoint data. To assess glutamate induced cell death after *Psmb5* and *Psmb8* overexpression, we analyzed cultures 7-10 days post-lentiviral transfection where no toxicity was observed by the overexpression itself (Figure S12H). To assess cell death after *Psmb5* and *Psmb8* overexpression, we counted the number of dead cells, identified by morphology and condensed nuclei, 21 days post-lentiviral transfection (in total 28 d.i.v.; Figure S12H). As previously shown,[14] we applied 5 µM DAPI to the cultures for 10 minutes before they were fixed with 4% PFA. Since DAPI does not cross the intact cell membrane, DAPI uptake measures cell membrane permeability in the setting of cell death. After fixation, we additionally stained MAP2, a structural marker of neuronal dendrites. Cells with a DAPI MFI higher than the average DAPI MFI plus 2.5 × standard deviation of all control replicates were regarded as dead cells. Additionally, we visually assessed dendritic blebbing as an additional biomarker for neuronal death. The experimenters were blinded for the image acquisition and analysis. We acquired 4 images with a ×10 magnification using a Zeiss LSM 900 Airyscan 2 confocal microscope that were stitched together and counted as field of view. When indicated, cultures were treated with compounds every other day for 10 days before the readout.

Estimation of mitochondrial and glycolytic respiration

We used an adapted assay to measure mitochondrial and glycolytic respiration. We measured ATP levels using the CellTiter-Glo Luminescent Cell Viability Assay (Promega, cat. G7570), performed according to manufacturer's protocol. We recorded luminescence with a Spark 10M multimode microplate reader (Tecan). Per plate, we measured ATP levels in neurons without stimulation, stimulation with 10 µM oligomycin and 0.5 µM rotenone, or stimulation with 10 µM oligomycin, 0.5 µM rotenone and 5 mM 2-DG. Mitochondrial respiration was defined as the difference between baseline ATP levels and ATP levels after respiratory chain blockade. Glycolytic respiration (referred to as ‘‘glycolytic index’’) was defined as difference between ATP levels after respiratory chain blockade and ATP levels after respiratory chain and glycolysis blockade. If indicated, we added 500 nM Pfk-158 instead of 2-DG to calculate the ‘‘PFKFB3 index’’. At least four technical replicates were used per condition, which were averaged per biological replicate for statistical analysis.

Seahorse assay

To study neuronal metabolism, we performed Seahorse assays using the XFe96 Extracellular Flux Analyzer (Agilent). Hippocampal neurons were seeded at a density of 50,000 cells per well in XFe96 Cell Culture Microplates (Agilent, cat. no. 103793-100) and maintained for 12–17 days in vitro (d.i.v.). Overexpression or treatment conditions were applied as indicated in the corresponding figure. One day before the assay, XFe96 FluxPak sensor cartridges (Agilent, cat. no. 103793-100) were hydrated in 200 µL XF Calibrant (Agilent, cat. no. 103575-100) and incubated overnight in a CO_2-free incubator. On the day of the assay, fresh assay medium was prepared using Seahorse XF DMEM (Agilent, cat. no. 103575-100) supplemented with glucose (25 mM), pyruvate (1 mM), and L-glutamine (2 mM). One hour before measurement, neuronal culture medium was replaced with assay medium, and plates were incubated in a CO_2-free incubator. For metabolic assessment, we performed the Seahorse XF Cell Mito Stress Test (Agilent, cat. no. 103015-100) according to the manufacturer's instructions, using final concentrations of 2 µM oligomycin, 1 µM FCCP, and 0.5 µM rotenone/antimycin A. This assay allows the quantification of the oxygen consumption rate and the extracellular acidification rate and thereby quantifies the mitochondrial respiration and indirectly the glycolytic respiration. Additionally, we performed the Seahorse XF Glycolytic Rate Assay (Agilent, cat. no. 103344-100) with final concentrations of 0.5 µM rotenone/antimycin A and 20 mM 2-DG. The glycolytic rate assay allows the direct estimation of glycolysis by quantifying the glycolysis-dependent proton efflux rate. We performed the following analyses for the Mito Stress Test: OCR at baseline, ATP-linked respiration (OCR baseline – OCR after oligomycin), maximal respiration (OCR after FCCP – OCR after rotenone and antimycin A), glycolytic acidification at baseline (ECAR / OCR ratio at baseline), glycolytic acidification after inhibition of mitochondrial respiration (ECAR after oligomycin / ECAR at baseline). We performed the following analyses for the Glycolytic Rate Assay: baseline glycolysis (GlycoPER at baseline), compensatory glycolysis (GlycoPER after rotenone and antimycin A – GlycoPER after 2-DG), percentage of GlycoPER of total PER.

GSH estimation

GSH-Glo assay (Promega) was performed as per the manufacturer's instructions. Primary cortical neurons were cultured in a white 96-well plate and transduced with the respective lentiviruses at 7 d.i.v as described above. If indicated in the respective figures, additional treatments were applied every other day starting from 10 d.i.v. Cells were washed with preconditioned neuronal medium, and GSH-Glo reagent was added to the wells for 30 minutes at room temperature, followed by the addition of luciferin detection reagent. After 15 minutes, luminescence was detected using a Spark 10M multimode microplate reader (Tecan). At least 4 technical replicates per condition for measuring GSSG and total glutathione (GSH).

Lactate estimation

Lactate levels were estimated using the Lactate-Glo (Promega), following the manufacturer's instruction. Neurons were cultured and stimulated as described for the GSH estimation. Luminescence was detected using a Spark 10M multimode microplate reader (Tecan). At least 4 technical replicates per condition were used.

Glucose-6-phosphate dehydrogenase (G6PD) activity estimation

G6PD activity was estimated using the Glucose-Glo (Promega) according to the manufacturer's instruction. Neurons were cultured and stimulated as described for the GSH estimation. Luminescence was detected using a Spark 10M multimode microplate reader (Tecan). At least 4 technical replicates per condition were used.

Nicotinamide adenine dinucleotide phosphate (NADPH) estimation

NAPDH levels were measured using the NADPH-Glo (Promega) according to the manufacturer's instruction. Neurons were cultured and stimulated as described for the GSH estimation. Luminescence was detected using a Spark 10M multimode microplate reader (Tecan), with at least 4 technical replicates per condition.

MALDI mass spectrometry imaging

Mice were intracardially perfused with ice-cold PBS for 1 minute and 4% PFA for 4 minutes. Spinal cords were removed, post-fixed in 4% PFA for 1 hour, incubated in 30% sucrose for 2 days and subsequently stored at -80°C. The fixed spinal cord samples were cut into 8 μm coronal sections using a cryotome (Leica CM2050 S) and mounted on conductive indium tin oxide (ITO) slides (Part No.:237001, Bruker Daltonik GmbH, Bremen, Germany). The matrix solution of 1,5-diaminonaphthalin hydrochloride was prepared as previously published.[97] The matrix solution was applied using a SunCollect MALDI Sprayer (SunChrom Wissenschaftliche Geräte GmbH, Friedrichsdorf, Germany). The matrix solution was sprayed at 15 μL min^{-1} for the first layer, 20 μL min^{-1} for the second layer and for the following eight layers at 25 μL min^{-1}. The distance from the sprayer nozzle to the sample was maintained at 40 mm. For the MALDI-MSI measurements, a MALDI-TOF/TOF instrument (rapifleX, Bruker Daltonics GmbH & Co. KG, Bremen, Germany) was used. The laser was set to a repetition rate of 5,000 Hz. Mass spectra were recorded using 800 laser shots per each pixel in negative ion mode. The mass range was set to m/z 80–1,200. The laser focusing size and spatial resolution were set to 20 μm. Prior to data acquisition, mass calibration was performed using an external standard (LightSPLASH, Avanti Polar Lipids, Alabama, United States). Data were acquired using flexControl 4.0 and flexImaging 5.0 (Bruker Daltonics GmbH & Co. KG). Ion images were acquired and evaluated using SCiLS Lab Version 2024a Pro (Bruker Daltonics GmbH & Co. KG). The following negative mode masses were used: fructose-1/2,6-bisphosphate – m/z 338.99, glucose – m/z 179.0556, phosphoenolpyruvate – m/z 166.9745, succinate – m/z 117.0187, pyruvate – m/z 87.0082, lactate – m/z 89.0238, fumarate – m/z 115.0031, glutathione – m/z 306.0759, glucose-6-phosphate – m/z 259.0213, malate – m/z 133.006, ribose-5-phosphate – m/z 229.019, 6-phosphogluconate – m/z 275.01, NADPH – m/z 744.091. We quantified the respective average intensities of the ventral horn of the spinal cords where the motoneurons degenerate in EAE. We performed unpaired *t*-tests for statistical comparisons.

Reactive oxygen species (ROS) live cell imaging

Oxidative stress in response to the indicated stressors was detected using CellROX green reagent (Thermo Fisher Scientific). Neuronal cultures were stimulated with 50 μM glutamate for 1 hour. If indicated in the respective figures, additional treatments were applied 30 minutes before glutamate stimulation. CellROX reagent was added to the wells at a final concentration of 5 μM after 30 minutes of glutamate exposure. Hoechst 33342, a cell-permeant nuclear counterstain, was added simultaneously. Cells were washed two times with pre-conditioned medium before image acquisition. Imaging was performed using a Zeiss LSM 900 Airyscan 2 confocal microscope with ×40 magnification. Immunofluorescence of nuclear CellROX dye was quantified using FIJI (ImageJ).

Lipid peroxidation live cell imaging

To detect lipid peroxidation in response to the indicated stressors, boron-dipyrromethene (BODIPY) C11 (Image-iT, Thermo Fisher Scientific) was used. Neuronal cultures were stimulated with 50 μM glutamate or 6 μM RSL3 for 8 hours. If indicated in the respective figures, additional treatments were applied 30 minutes prior the stressors. BODIPY C11 reagent was added to the wells at a final concentration of 20 μM for 1 hour. Hoechst 33342, a cell-permeant nuclear counterstain, was added simultaneously. Cells were washed twice with preconditioned medium before image acquisition. Imaging was performed using a Zeiss LSM 900 Airyscan 2 confocal microscope with ×40 magnification. Immunofluorescence of was quantified using FIJI (ImageJ).

Immunocytochemistry

Neuronal cultures were grown on 12 mm diameter coverslips for immunocytochemistry. They were stimulated with 50 μM glutamate or 6 μM RSL3, or as indicated, treated with additional compounds 30 minutes before adding the stressors (see "Compounds and chemicals" for details). Following stimulation, cells were fixed with 4% paraformaldehyde (PFA) and incubated in 10% normal donkey's serum (NDS) containing 0.1% Triton X-100, followed by immunolabeling. Images were captured using a Zeiss LSM 900 Airyscan 2 confocal microscope. The following antibody concentrations were used: ACSL4 (1:100), Actin-Stain (1:80), CDK5 (1:100), FSP1 (1:100), GFP (1:1000), GPX4 (1:200), NeuN (1:500), PFKFB3 (1:300), RFP (1:1000).

Experimental autoimmune encephalomyelitis (EAE)

Unless stated otherwise, EAE refers to C57BL/6J mice, which were immunized subcutaneously with 200 μg myelin oligodendrocyte glycoprotein (MOG) 35–55 peptide (Schafer-N) in Freund's adjuvant (Difco, cat. no. DF0639-60-6) containing 4 mg ml^{-1} *Mycobacterium tuberculosis* (Difco, cat. no. DF3114-33-8). Additionally, 200 ng pertussis toxin (Calbiochem, cat. no. CAS70323-44-3) was injected intraperitoneally (i.p.) on the day of immunization and again 48 hours later. SJL/JRj mice were subcutaneously immunized with 0.2 mL of an emulsion containing 150 μg proteolipid protein (PLP) peptide 139-151 (HCLGKWLGHPDKF; peptides & elephants) in saline and an equal volume of complete Freund's adjuvant (BD, cat. no. 263910) containing 200 μg *Mycobacterium tuberculosis* H37RA (BD, cat. no. 231141). Clinical relapse was classified as a worsening in disease score by at least 1 point for at least 2 days after previously achieving remission. Samples (IHC) were obtained on day 40 post-immunization. Biozzi ABH mice were immunized with an emulsion containing 50 μg of purified recombinant MOG (N1-125) in complete Freund's adjuvant (containing 5–10 mg mL^{-1} *Mycobacterium tuberculosis* H37RA, Sigma-Aldrich) at day 0 and day 7. On day 0, 1, 7 and 8 following immunization, 50 ng of pertussis toxin was administered intraperitoneally.[98] We scored animals daily for clinical signs using the following system: 0, no clinical deficits; 1, tail weakness; 2, hind limb paresis; 3, partial hind limb paralysis; 3.5, full hind limb paralysis; 4, full hind limb paralysis and fore limb paresis; 5, premorbid or dead. Animals with a clinical score $\geq$ 4 were euthanized according to the local animal welfare regulations. Investigators were blind to the genotype and treatment during EAE experiments. To induce neuron-specific *Pfkfb3* knockouts, LSL-Cas9 mice were retro-orbitally injected with 8×10^{11} AAV-PHP.eB[99] AAV:ITR-U6-Pfkfb3-g1-hSyn-Cre-2A-EGFP-KASH-WPRE-shortPA-ITR and AAV:ITR-U6-Pfkfb3-g2-hSyn-Cre-2A-EGFP-KASH-WPRE-shortPA-ITR or AAV:ITR-U6-ntc-hSyn-Cre-2A-EGFP-KASH-WPRE-shortPA-ITR as controls (100 μL per animal). Thereby, we achieved 70–80% transduction efficacy of spinal cord motoneurons estimated by the GFP signal of transduced cells (representative images for all mice that were used for the statistical analyses of the disease score and subsequent histological analyses are shown in Figure S12I). EAE was induced 3 weeks after AAV injection. For treatment studies, mice were daily injected i.p. with either 10 mg kg^{-1} body weight ONX-0914 (PR-957) or 12 mg kg^{-1} body weight Pfk-158, starting in the acute stage of EAE, 14 days post-immunization. Compounds were dissolved in DMSO and injected in 10% DMSO and 90% PBS. Control animals were injected with the DMSO vehicle in the same ratio. Acute EAE stage refers to the peak disease 15 days post-immunization, and chronic EAE refers to the late-stage of the disease 30 days post-immunization.

RNA sequencing and analysis

RNA sequencing libraries of the neuronal cultures were prepared using the TruSeq stranded mRNA Library Prep Kit (Illumina) according to the manufacturer's manual (document 1000000040498 v00). Libraries were pooled and sequenced on a NovaSeq 6000 sequencer (Illumina), generating 50 bp paired-end reads. RNA sequencing libraries of the sorted nuclei were prepared using the NEBNext Ultra RNA Library Prep Kit (Illumina). Libraries were pooled and sequenced on an HiSeq2000 sequencer (Illumina) generating 50 bp single-end reads. Reads were aligned to the Ensembl mouse reference genome (GRCh39) using STAR v.2.4[90] with default parameters. Overlaps with annotated gene loci were counted using featureCounts v.1.5.1.[91] Differential expression analysis was performed with DESeq2 (v.3.12),[92] with genes showing a false discovery rate (FDR)-adjusted $P < 0.05$ considered differentially expressed. Gene lists were annotated using biomaRt (v.4.0).

Nucleus isolation and flow cytometric sorting

Spinal cords of healthy and acute EAE (15 days post-immunization) mice were collected following PBS perfusion and stored at -80°C. Nuclei were isolated using the Nucleus Isolation Kit (Sigma-Aldrich; catalog no. NUC101) per the manufacturer's protocol. Isolated nuclei were washed and labeled with an antibody directed against NeuN conjugated to Alexa Fluor 647 (Abcam, EPR12763) and propidium iodide (PI) to stain nuclei. $NeuN^{+}PI^{+}$ nuclei were sorted by flow cytometry using a BD FACSAriaTM III Cell sorter (BD Bioscience).

Mouse histopathology

Mouse spinal cord and cortex tissues of SJL/JRj and C57BL/6J were obtained and processed as described previously.[12] Images were acquired using a Zeiss LSM 900 Airyscan 2 laser scanning confocal microscope. The following antibody concentrations were used: 4-HNE (1:100), CC1 (1:200), CD31 (1:200), CDH1 (1:100), CDK5 (1:100), GFAP (1:500), GFP (1:300), IBA1 (1:250), iNOS (1:200), MAP2 (1:500), MHC I (1:100), NG2 (1:200) NeuN (1:300), PFKFB3 (1:200), Ubiquitin (1:200), PSMB5 (1:100), PSMB8 (1:100).

Biozzi mouse tissue was paraffin embedded and 2 μm sections were mounted on Superfrost glass slide. After deparaffination and antigen retrieval (Marmite Pascal Citrate pH 6.0) and to prevent myelin autofluorescence, slides were submerged in a solution of 4.5% H_2O_2 and 20 mM NaOH in PBS under a light emitting diode (LED) for 2 × 45 minutes at room temperature. Slides were then incubated in a blocking solution for one hour at room temperature (MOM, blocking reagent, Vector Laboratories, #MKB-2213) and unspecific binding blocked (PBS/2.5% goat serum) before one hour incubation with a mouse anti-PSMB8 antibody (Proteintech, # 66759-1). To visualize tissue-bound antibody, anti-mouse HRP (Dako, K4003) with amplification (TSA vivid 520, Tocris,7534) was used as secondary system. After denaturation (Discovery Roche, CC2), slides were incubated with Dako REAL peroxidase-blocking solution (Dako, K0672) and unspecific binding blocked (PBS/2.5% goat serum) before one hour incubation with rabbit anti-PFKFB3 antibody (abcam, #ab181861). To visualize the specific signal, anti-rabbit HRP (Dako, K4003) with amplification (TSA vivid 570, Tocris,7535) was used as secondary system. Sections were then incubated with a mouse anti-HuC/D (Invitrogen, #A-21271) one hour at room temperature and specific binding was visualized with a goat anti-mouse IgG2b AlexaFluor 647 conjugated (Life, #A21242). Nuclei were stained with DAPI (Invitrogen, D1306). Slides were mounted in Fluoromount aqueous mounting medium (Sigma-Aldrich, F4680) for acquisition. Stained sections were scanned using the Panoramic 250 FLASH II (3DHISTECH) Whole Slide Scanner at a 0.221 μm/px resolution.

If not otherwise stated, we quantified the neuronal counts and the MFI of target proteins in neurons of the ventral horn outflow tract in the spinal cord. This region was chosen, as it is primarily affected by inflammation and the neuronal loss is mainly responsible for motor impairments in the C57BL/6J EAE model during the late stage of the disease, whereas no loss of dorsal horn neurons is observed in EAE (Figure S12J). To quantify the neuronal MFI, we acquired two images of both spinal cord ventral horns per mouse section. After background subtraction, we used NeuN to generate a neuronal mask and measured the fluorescence intensity of the indicated markers in all neurons (typically 20–40 neurons per ventral horn). These values were averaged per animal and reported as MFI. Furthermore, we quantified the numbers of axons in the dorsal columns, as they are also lost in EAE (Figure S12J). To do this, we acquired two images per mouse and generated a mask to detect the axonal cross-sections. The number of axons was normalized to the area.

Human histopathology

Human brain biopsies used for this study consisted of tissues that could not be utilized for diagnostic purposes (Table S1). We deparaffinized the sections using a standard ethanol and xylol dilution. After rinsing in water, antigen retrieval was performed using a sodium citrate buffer (pH = 6.5). After permeabilization with 0.1% Triton and blocking with 10% normal donkey serum, immunolabeling was conducted with antibodies directed against NeuN (1:100) and PSMB8 (1:100). Images were captured using a Zeiss LSM 900 Airyscan 2 laser scanning confocal microscope. Human postmortem brain tissues were acquired from the UK biobank (Table S1). Postmortem tissue processing followed standard fixation and embedding methods.[9] Briefly, CNS tissue was fixed in 4% formalin, embedded in paraffin, and 2 μm sections were mounted on a glass slide. Sections were deparaffinized, and antigen retrieval (Marmite Pascal Citrate pH 6.0) was performed. To prevent unspecific binding of primary antibodies, sections were incubated with normal goat serum (2.5% in PBS) before 2 hours of incubation with the following primary antibodies: HuC/D (1:100), PFKFB3 (1:100), PSMB8 (proteintech, 1:1000). Nuclei were counterstained with DAPI (Life Technologies, D3571). Stained sections were scanned using a Panoramic 250 FLASH II (3DHISTECH) Whole Slide Scanner at a 0.221 μm px^{-1} resolution. Background subtraction was performed for data analysis with the signal from the white matter.

Transmission electron microscopy

Following PBS perfusion, the spinal cords were removed and fixed in 1% glutaraldehyde and 4% PFA. Tissue was washed in 0.1 M PBS (pH = 7.3) with sucrose twice and kept overnight. Next day, tissue was post-fixed in 1% osmium for 60 minutes, washed twice in 0.05 M maleic acid buffer (pH = 5.2) and embedded in TAAB 812 Epon (TAAB, Berkshire, England) with the Leica EM Tissue Processor (Triolab A/S, Brøndby, Denmark). The program sequence was: uranyl acetate in maleic acid buffer for 60 minutes, maleic acid 5 minutes, maleic acid 2 × 10 minutes, 70% ethanol in 2 × 10 minutes, 86% ethanol 2 × 10 minutes, 96% ethanol 2 × 10 minutes, 99% ethanol 5 min, 99% ethanol 2 × 10 minutes, 100% acetone 3 × 10 minutes and 100% acetone/Epon 1:1 overnight with a cover. Next day, the tissues were kept in Epon 60 minutes, embedded in fresh Epon polymerizing at 60°C for one day. Epon blocks were cut on a Ultramicrotome Leica EM UC6 with a Diatome diamond knife into ~70 nm thick sections. Digital images were made with a Joel JEM-1400Plus transmission electron microscope at original magnifications ×600, ×1,200 and ×10,000. We evaluated the structural integrity of mitochondria and the myelin sheaths in 3 *Psmb8*-cKO and 3 *Pfkfb3*-cKO mice with 3 respective WT mice during peak EAE 15 days post-immunization. Neurons were identified by the presence of synapses, dendrites and axons.

Immunoblot

Spinal cords or cortices of healthy and EAE mice were homogenized using a tissue grinder in 2 mL, radioimmunoprecipitation buffer (50 mM Tris, 150 mM NaCl, 0.5 mM EDTA, 10% SDS, 1% NP-40, 10% sodium deoxycholate, protease and phosphate inhibitor cocktails (cOmplete, Roche)). Samples were incubated at 4°C for 30 minutes on a rotating wheel and then centrifuged for 5 minutes to remove cell debris. Pellets from mouse primary neurons, and N2a cells were processed similarly, but in a volume of 200 μl radioimmunoprecipitation buffer. Protein concentrations were measured using a BCA assay (Pierce BCA Protein Assay Kit, Thermo Fisher Scientific). We loaded 25 μg protein per sample onto SDS-pages (NuPAGE, Thermo Fisher Scientific) and transferred them to polyvinyl fluoride membranes. Blocking was performed using 5% BSA for 1 hour at room temperature. Primary antibodies were incubated overnight at 4°C. Secondary antibodies conjugated with horseradish peroxidase were applied for 1 hour at room temperature, and chemiluminescence was visualized using WesternSure PREMIUM Chemiluminescent Substrate (LI-COR). The following antibody concentrations were used: CDH1 (1:500), PSMB5 (1:500), PSMB8 (1:500), GAPDH (1:1000), vinculin (1:1000), mouse IgG-HRP (1:20,000), rabbit IgG-HRP (1:20,000).

Real-time PCR

We reverse-transcribed RNA to complementary DNA with the RevertAid H Minus First Strand cDNA Synthesis Kit (Thermo Fisher Scientific, Cat. No. K1632) according to the manufacturer's instructions. Samples were measured on a QuantStudio Flex Real-Time PCR System using the following TaqMan Gene Expression Assays (Thermo Fisher Scientific): *Cxcl10* (Mm00445235_m1), *Ifi44* (Mm00505670_m1), *Ifit1* (Mm07295796_m1), *Psmb5* (Mm07296970_g1), *Psmb8* (Mm00440207_m1), *Stat1* (Mm01257286_m1), *Tbp* (Mm01277042_m1).

Immunophenotyping by flow cytometry

Brain and spinal cord tissue were collected after transcardial PBS perfusion and dissociated into single-cell suspensions using 1 mg mL^{-1} collagenase A (Roche) and 0.1 mg mL^{-1} DNase I (Merck) with the gentleMACS Octo Dissociator (Miltenyi Biotec, program: Multi_F). The dissociated tissue was passed through a 70 μm cell strainer, and immune and glia cells were enriched using a discontinuous density gradient. After centrifugation at 2,500 rpm, 4°C for 30 minutes, cells were collected from the interphase between the 30% Percoll and 78% Percoll layer. Nonspecific Fc receptor–mediated antibody binding was blocked by pre-incubation with TruStain FcX anti-mouse CD16/32 antibody (BioLegend) for 10 minutes at 4°C, followed by surface antibody staining in Brilliant Stain Buffer (BD Biosciences) for 30 minutes at 4°C. Dead cells were excluded from analysis using Zombie Green and NIR Fixable Viability Stains (BioLegend). For intracellular CD68 staining, cell suspensions were fixed for 20 minutes at room temperature using Fixation Buffer (BioLegend), then incubated for 20 minutes with anti-CD68 or IFNγ antibodies in Intracellular Staining Permeabilization Wash Buffer (BioLegend). Absolute cell numbers for CD45high leukocytes and CD45med microglia were determined using Precision Count Beads (BioLegend). We obtained data using a BD Symphony A3 flow cytometer (BD Biosciences) and analyzed with FlowJo (BD Biosciences).

QUANTIFICATION AND STATISTICAL ANALYSIS

Details of the statistical analyses used in the bioinformatics analyses are provided in the respective sections of the article. Images were analyzed using FIJI software (NIH), and experimental data were analyzed within the R environment on a macOS. Visualizations were generated with the tidyverse and tidyplots[100] packages. Unless otherwise stated, data are presented as means with individual data points. Differences between two experimental groups were determined using unpaired, two-tailed Student's t-tests or Mann Whitney U tests with FDR-correction for multiple comparisons. Comparisons between more than two experimental groups were conducted using a one-way-ANOVA, with post hoc Tukey's HSD tests performed between the groups if the ANOVA reached significance. Specific statistical tests are provided in the respective figure legends. For EAE experiments, clinical scores were statistically analyzed by applying a Mann-Whitney U-test to the areas under the curve for each animal. Significant results are indicated as follows: $^*P < 0.05$, $^{**}P < 0.01$, $^{***}P < 0.001$, $^{****}P<0.0001$.

Supplemental figures

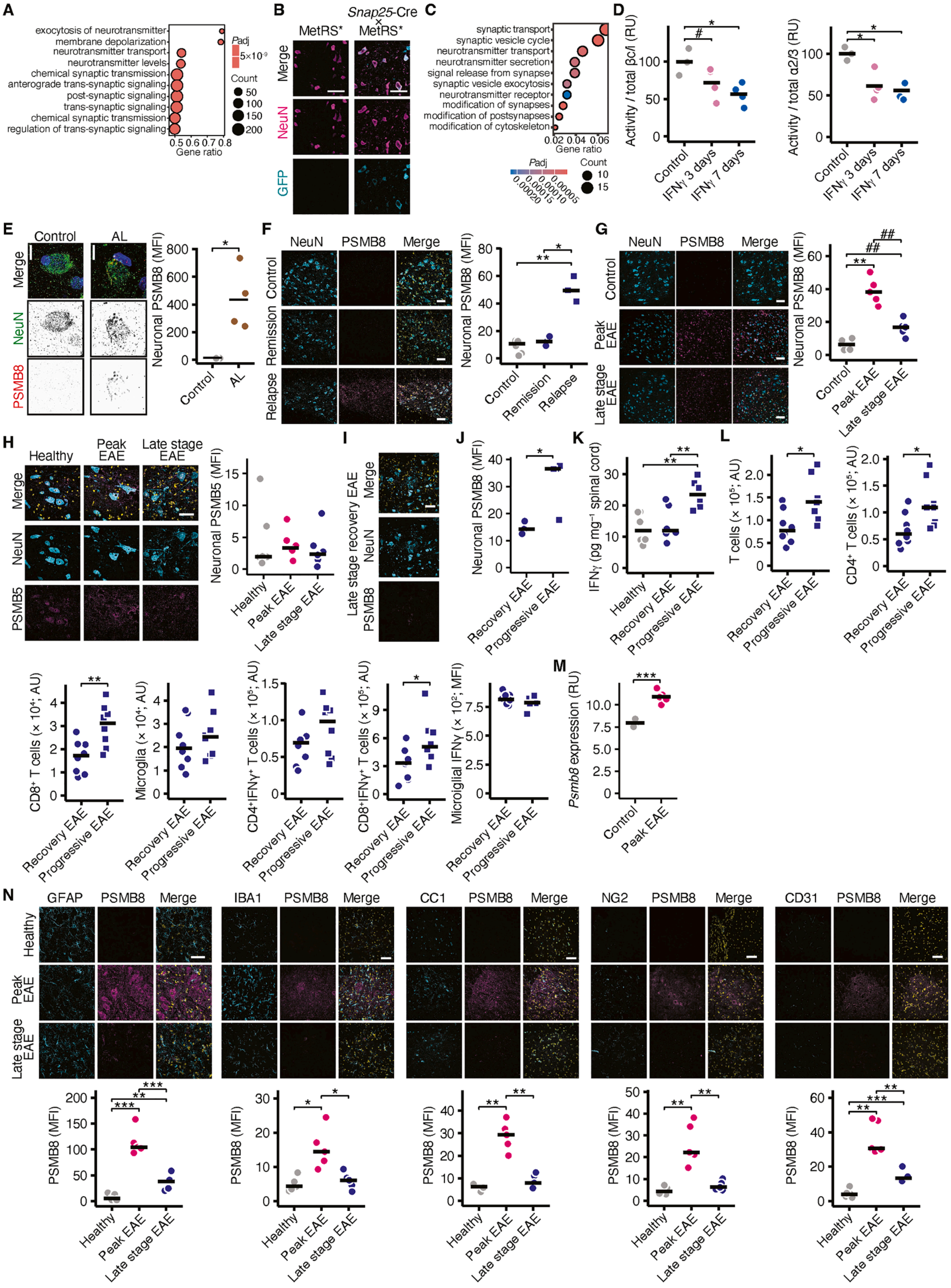

(legend on next page)

Figure S1. PSMB8 and IFNγ are increased in chronic progressive EAE mice, related to Figure 1

(A) Gene Ontology biology process analysis of all genes that were differentially upregulated in neuronal nuclei compared with non-neuronal nuclei of healthy mice ($n = 5$).

(B) Representative images of spinal cords of *LSL-R26-MetRS** and *Snap25*-Cre × *LSL-R26-MetRS** mice. The Cre-recombinase-carrying cells are visualized by GFP expression. Scale bar, 5 μm.

(C) Gene Ontology biological process analysis of proteins that are significantly more abundant in neurons of *Snap25*-Cre × LSL-R26-MetRS* healthy mice in comparison with whole spinal cords of *Snap25*-Cre × LSL-R26-MetRS* healthy mice ($n = 5$).

(D) Analysis of the total PSMB5/PSMB8 activity using the pan-proteasomal activity probe Cy5-epoxomicin in neurons stimulated with 100 ng mL^{-1} IFNγ for 3 or 7 days ($n = 4$). The activity was normalized to either total PSMB5/8 (left) or PSMA2/3 protein levels (right). A one-way ANOVA ($p < 0.05$) with post hoc Tukey's HSD tests was used for statistical comparison. $^{*}p < 0.05$ with correction for multiple comparisons. $^{\#}p < 0.05$ without correction for multiple comparisons.

(E) Neuronal PSMB8 MFI in biopsies from control and active lesions (ALs) of people with relapsing MS ($n = 4$), NeuN marks neurons, and DAPI marks nuclei.

(F) Neuronal PSMB8 MFI in the spinal cord VHOT of healthy SJL mice ($n = 6$) and SJL mice with EAE 40 days p.i. Mice that remitted (final score = 0; $n = 3$) and those with a relapse (final score > 1; $n = 3$) were separately analyzed. Nuclei were visualized with DAPI (yellow). Scale bar, 50 μm. A one-way ANOVA ($p < 0.05$) with post hoc Tukey's HSD tests was used for statistical comparison.

(G) Neuronal PSMB8 MFI in the spinal cord VHOT of healthy Biozzi ABH mice and Biozzi ABH mice subjected to EAE 2 days after disease onset (peak disease) and 20 days after onset of disease progression (late-stage of the disease; $n = 5$). Nuclei were visualized with DAPI (yellow). Scale bar, 50 μm. A one-way ANOVA ($p < 0.05$) with post hoc Tukey's HSD tests was used for statistical comparison. $^{**}p < 0.01$ in Tukey's HSD test, $^{\#\#}p < 0.01$ in unpaired FDR-adjusted t tests.

(H) Neuronal PSMB5 MFI in the VHOT of healthy ($n = 5$), peak EAE (15 days p.i.; $n = 6$), and late-stage EAE mice (30 days p.i.; $n = 7$). Nuclei were visualized with DAPI (yellow). Scale bar, 50 μm. A one-way ANOVA ($p > 0.05$) was used.

(I) Representative image of neuronal PSMB8 in late-stage recovery EAE mice. Nuclei were visualized with DAPI (yellow). Scale bar, 50 μm. NeuN marks neurons.

(J) Quantification of neuronal PSMB8 MFI in late-stage EAE mice (30 days p.i.) that recovered (final clinical EAE score < 2; $n = 3$) and those with progressive disease (final clinical EAE score > 2; $n = 4$).

(K) ELISA measured IFNγ levels (pg mL^{-1}) in spinal cord lysates of healthy mice, late-stage EAE mice (30 days p.i.) that recovered (final clinical EAE score < 2) and those with progressive disease (final clinical EAE score > 2; $n = 6$). A one-way ANOVA ($p < 0.05$) with post hoc Tukey's HSD tests was used for statistical comparison.

(L) Absolute numbers (absolute units [AU]) by flow cytometry of the indicated immune cell populations, $IFN\gamma^{+}$ T cell populations and microglia IFNγ MFI in spinal cords of late-stage EAE mice (30 days p.i.) that recovered (final clinical EAE score < 2) and those with progressive disease (final clinical EAE score > 2; $n = 8$).

(M) Normalized *Psmb8* expression in non-neuronal nuclei of healthy and peak EAE mice (15 days p.i.; $n = 5$), estimated via bulk mRNA sequencing. Differential expression analysis with FDR correction was used for statistical analyses.

(N) PSMB8 MFI in GFAP+ glia cells (astrocytes), IBA1+ glia cells (microglia), CC1+ glia cells ([pre-]myelinating oligodendrocytes), NG2+ glia cells (oligodendrocyte progenitor cells), and CD31+ cells (endothelial cells) in the spinal cord ventral horns of healthy mice ($n = 5$), peak EAE mice (15 days p.i.; $n = 5$), and late-stage EAE mice (30 days p.i.; $n = 6$). Nuclei were visualized with DAPI (yellow). Scale bar, 50 μm. A one-way ANOVA ($p < 0.05$) with post hoc Tukey's HSD tests was used for statistical comparison.

Unless otherwise stated, unpaired t tests with FDR correction for multiple comparisons were used. Individual data points and means are shown. $^{*}p < 0.05$, $^{**}p < 0.01$, $^{***}p < 0.001$, $^{****}p < 0.0001$.

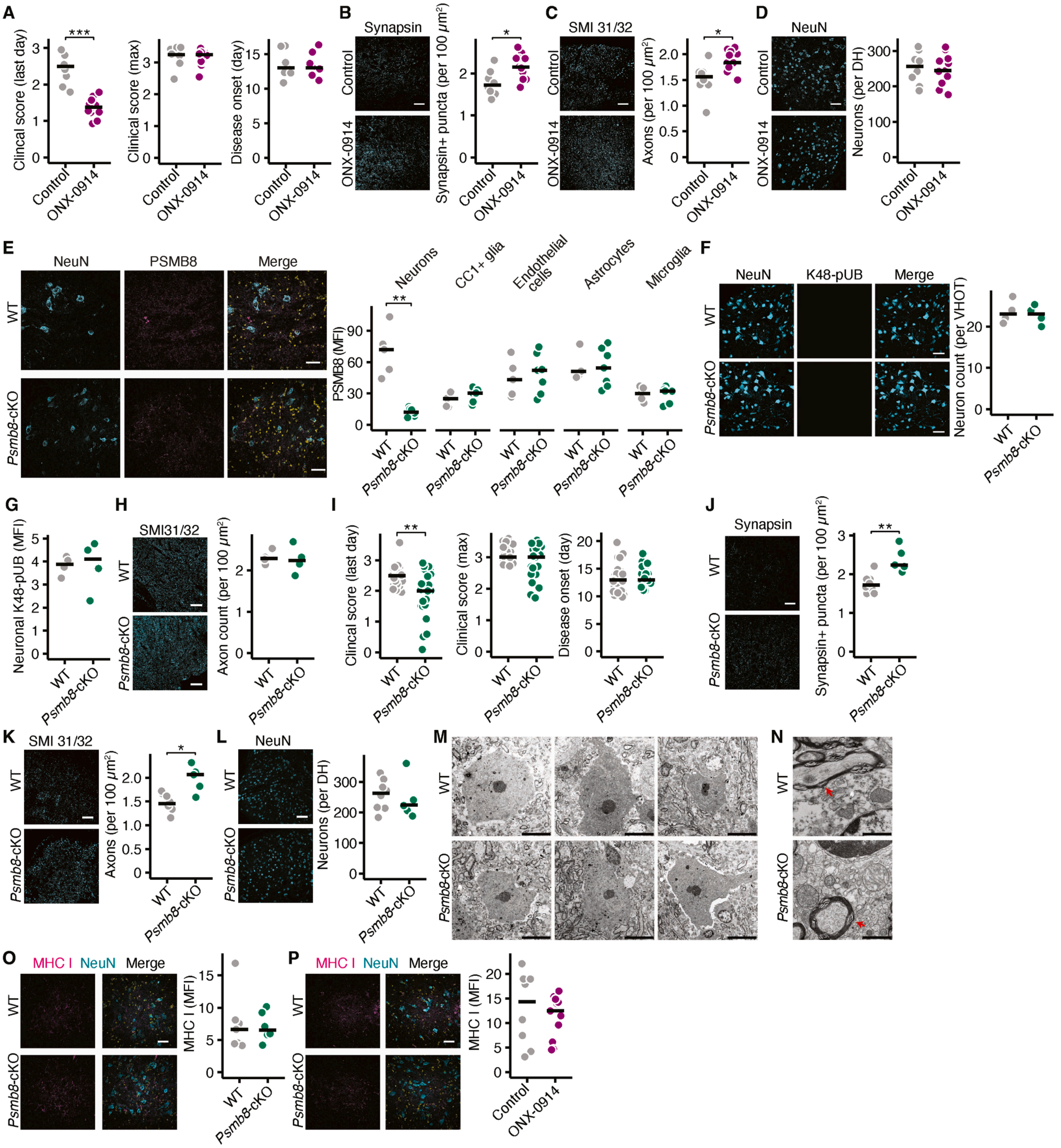

Figure S2. Neuronal *Psmb8*-deletion protects against inflammation-induced axonal degeneration, related to Figure 1

(A) Clinical score on the last day, maximal clinical score, and day of disease onset in EAE mice treated daily with vehicle (*n* = 9) or 10 mg kg^{-1} body weight ONX-0914 (*n* = 12) i.p., starting at the acute EAE stage, 14 days post-immunization. The Mann-Whitney U test was used for statistical comparisons.

(B–D) Synapsin+ puncta per 100 μm^2 (B) in the spinal cord VHOT, axonal counts per 100 μm^2 in the dorsal columns (C), and neuronal counts in the dorsal horns (D) of late-stage EAE mice (30 days p.i.) treated with a vehicle (*n* = 9) or 10 mg kg^{-1} body weight ONX-0914 (*n* = 11). Scale bar, 50 μm.

(E) PSMB8 MFI in neurons, CC1+ (pre-)myelinating oligodendrocytes, endothelial cells, astrocytes, and microglia in the spinal cord VHOT of WT (*n* = 5), and *Psmb8*-cKO mice (*n* = 7) during peak EAE (15 days p.i.). Nuclei were visualized with DAPI (yellow). Scale bar, 50 μm.

(F–H) Neuron count (F), neuronal K48-poly-ubiquitin (K48-pUB; G) levels in spinal cord VHOT neurons, and axonal counts in the dorsal columns (H) of healthy WT (*n* = 4) and *Psmb8*-cKO (*n* = 4) mice. Scale bar, 50 μm.

(legend continued on next page)

(I) Clinical score on the last day, maximal clinical score, and day of disease onset in WT ($n = 34$) and *Psmb8*-cKO ($n = 24$) EAE mice. The Mann-Whitney U test was used for statistical comparisons.

(J–L) Synapsin+ puncta per 100 μm^2 (J) in the spinal cord VHOT, axonal counts per 100 μm^2 in the dorsal columns (K), and neuronal counts in the dorsal horns (L) of WT ($n = 8$) and *Psmb8*-cKO ($n = 5$) late-stage EAE mice (30 days p.i.). Scale bar, 50 μm.

(M and N) Overview (M) transmission electron microscopy images of spinal cord neurons from WT ($n = 3$) and *Psmb8*-cKO mice ($n = 3$) mice during peak EAE (15 days p.i.). Higher magnification of axons with myelin sheaths are shown and highlighted by arrows (N). Scale bar, 10 μm (M) and 1 μm (O).

(O) MHC class I staining (MFI) in spinal cord VHOT neurons of WT ($n = 8$) and *Psmb8*-cKO ($n = 7$) EAE mice during peak EAE (15 days p.i.). Nuclei were visualized with DAPI (yellow). Scale bar, 50 μm.

(P) MHC class I staining (MFI) in spinal cord VHOT neurons of EAE mice that were treated with a vehicle ($n = 9$) or 10 mg kg^{-1} body weight ONX-0914 ($n = 11$) during peak EAE (15 days p.i.). Nuclei were visualized with DAPI (yellow). Scale bar, 50 μm.

Unless otherwise stated, unpaired t tests with FDR correction for multiple comparisons were used, and individual data points and means are shown. *$p < 0.05$, **$p < 0.01$, ***$p < 0.001$.

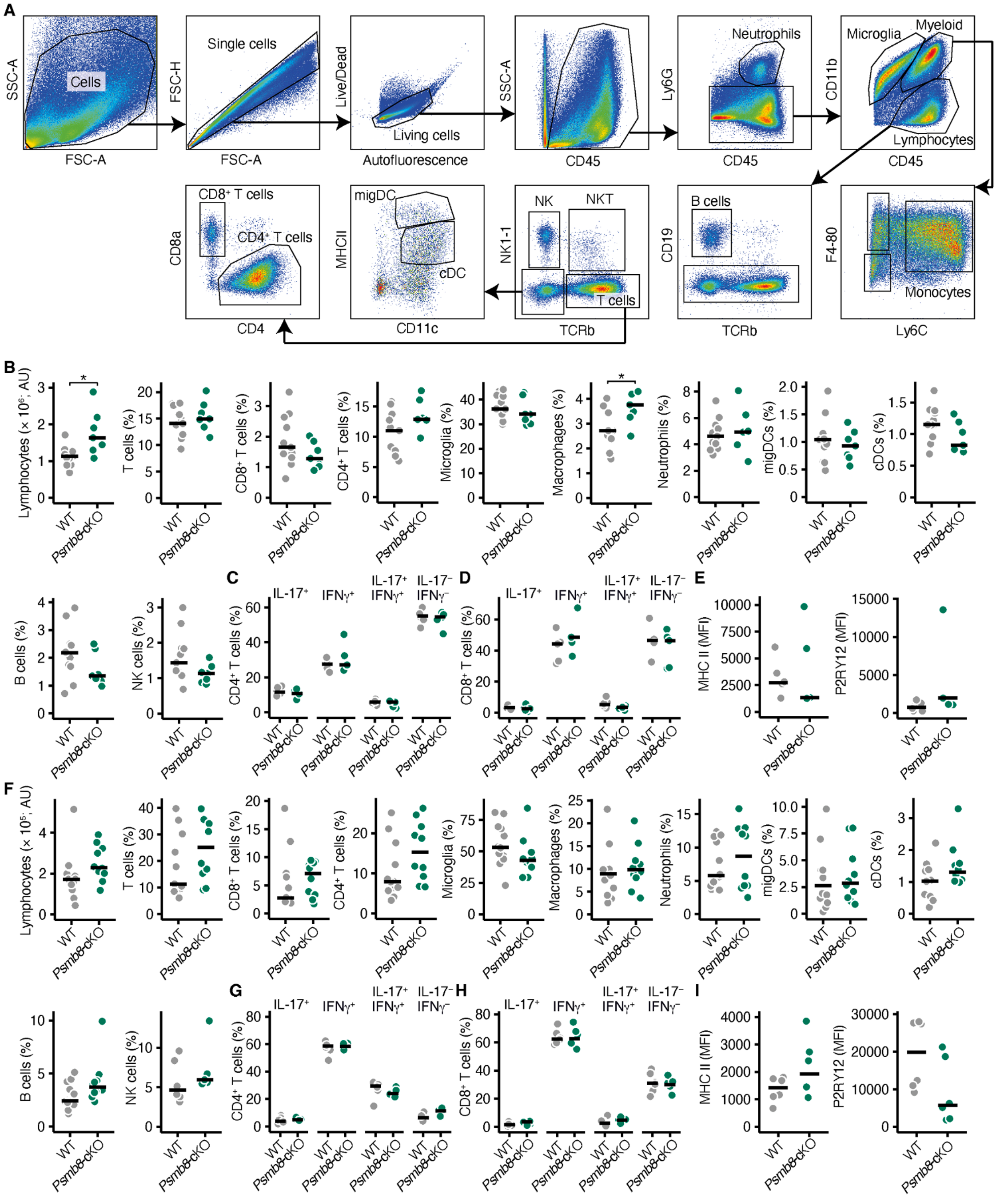

Figure S3. Neuronal PSMB8 does not alter the T cell landscape, related to Figure 1

(A) Representative gating strategy.

(B) Absolute number of CNS-infiltrating lymphocytes and the percentage of indicated immune cell populations among all lymphocytes in WT (*n* = 11) and *Psmb8*-cKO (*n* = 7) peak EAE mice (15 days p.i.).

(C and D) Percentage of IL-17$^+$, IFNγ$^+$, IL-17$^+$IFNγ$^+$, and IL-17$^-$IFNγ$^-$ CD4+ T cells (C) and CD8+ T cells (D) in WT (*n* = 5) and *Psmb8*-cKO (*n* = 6) peak EAE mice (15 days p.i.).

(E) MFI of MHC class II and P2RY12 in microglia of WT (*n* = 5) and *Psmb8*-cKO (*n* = 6) peak EAE mice (15 days p.i.).

(F) Absolute number of CNS-infiltrating lymphocytes and the percentage of indicated immune cell populations among all lymphocytes in WT (*n* = 12 except for natural killer [NK] cells, *n* = 6), and *Psmb8*-cKO (*n* = 10 except for NK cells, *n* = 6) late-stage EAE mice (30 days p.i.).

(G and H) Percentage of IL-17$^+$, IFNγ$^+$, IL-17$^+$IFNγ$^+$, and IL-17$^-$IFNγ$^-$ CD4+ T cells (G) and CD8+ T cells (H) in WT (*n* = 6) and *Psmb8*-cKO (*n* = 6) late-stage EAE mice (30 days p.i.).

(I) MFI of MHC class II and P2RY12 in microglia of WT (*n* = 6) and *Psmb8*-cKO (*n* = 6) late-stage EAE mice (30 days p.i.).

Unless otherwise stated, unpaired t tests with FDR correction for multiple comparisons were used, and individual data points and means are shown. *$p < 0.05$.

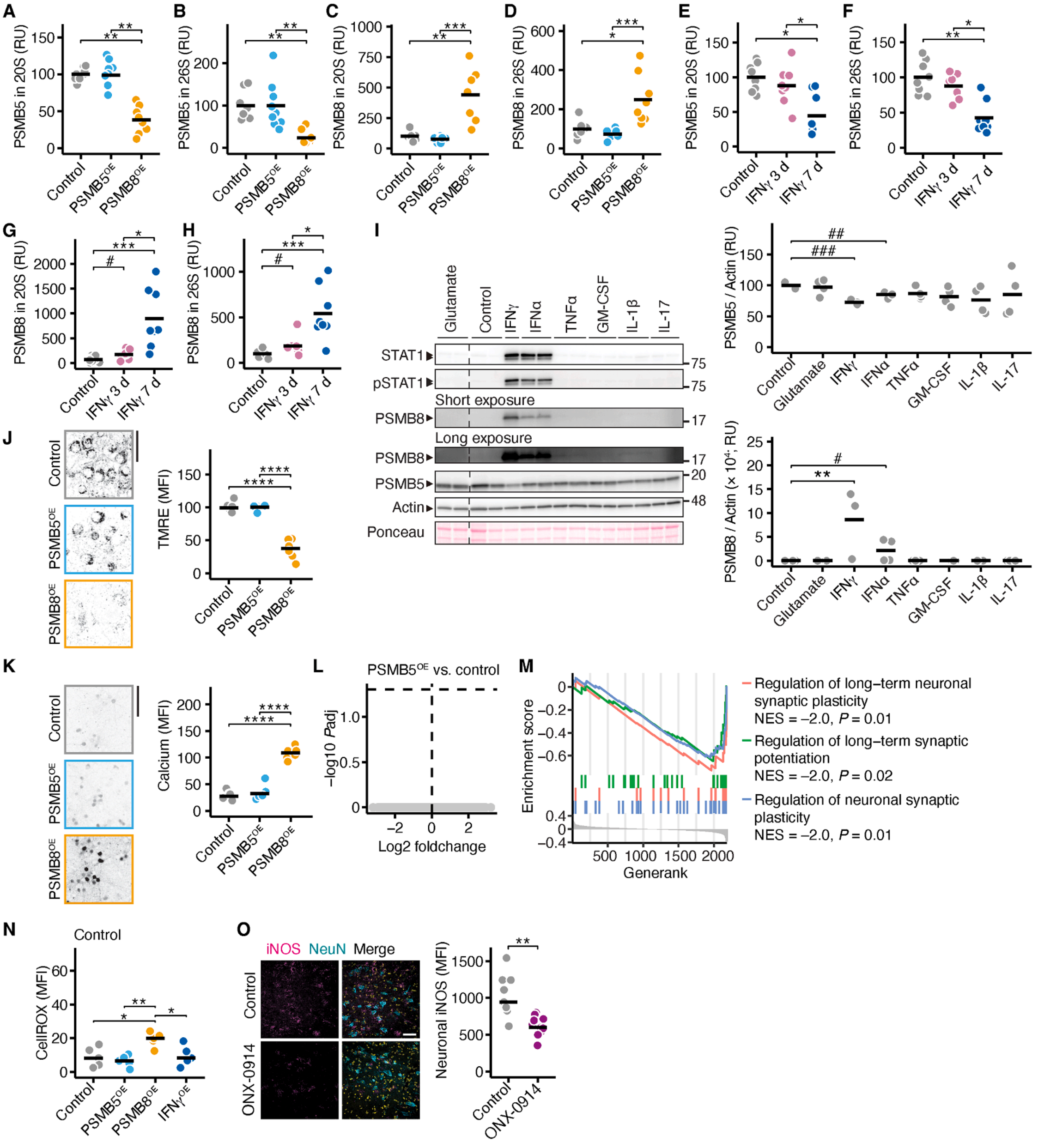

Figure S4. PSMB5 and PSMB8 are incorporated into the proteasome in neurons, related to Figure 2

(A–D) PSMB5 incorporation into the 20S (A), PSMB5 incorporation into the 26S (B), PSMB8 incorporation into the 20S (C), and PSMB8 incorporation into the 26S proteasome (D) in mScarlet control neurons ($n = 8$), PSMB5-overexpressing (PSMB5^{OE}; $n = 8$), or PSMB8-overexpressing (PSMB8^{OE}; $n = 8$) neurons. Representative images are shown in Figure 3A. A one-way ANOVA ($p < 0.05$) with post hoc Tukey's HSD tests was used for statistical comparison, $^{\#}p < 0.05$ in unpaired FDR-adjusted t tests.

(E–H) PSMB5 incorporation into the 20S (E), PSMB5 incorporation into the 26S (F), PSMB8 incorporation into the 20S (G), and PSMB8 incorporation into the 26S proteasome (H) in mScarlet control neurons ($n = 8$), neurons exposed to 100 ng mL^{-1} IFNγ for 3 days ($n = 8$) or 7 days ($n = 8$). Representative images are shown in Figure 3B. A one-way ANOVA ($p < 0.05$) with post hoc Tukey's HSD tests was used for statistical comparison, $^{\#}p < 0.05$ in unpaired FDR-adjusted t tests.

(I) Immunoblot analyses of PSMB5, PSMB8, actin, and Ponceau staining as loading control in neuronal cultures stimulated with 100 ng mL^{-1} IFNγ, IL-17, TNF-α, GM-CSF, and IL-1β for 7 days, or 50 μM glutamate for 4 h ($n = 4$; except for IFNγ, $n = 3$). STAT1 and phospho-STAT1 (pSTAT1) were included as positive controls for the induction of a type I IFN response. Protein levels were normalized to actin for quantification as RUs. A one-way ANOVA was performed with $p > 0.05$ for PSMB5 and $p < 0.05$ for PSMB8. Post hoc Tukey's HSD tests were conducted ($^{**}p < 0.01$) along with pairwise comparisons between control and the different stimulation conditions ($^{\#}p < 0.05$, $^{\#\#}p < 0.01$).

(J and K) Tetramethylrhodamine (TMRE) MFI as a biomarker for mitochondrial viability (J), and cytosolic calcium MFI (K) in mScarlet control, PSMB5^{OE}, and PSMB8^{OE} neurons ($n = 6$). Scale bars, 50 μm (J) and 100 μm (K). A one-way ANOVA ($p < 0.05$) with post hoc Tukey's HSD tests was used for statistical comparison.

(legend continued on next page)

(L) Volcano plot visualization of differential expression analysis in mScarlet control and PSMB5^{OE} neurons. The horizontal dashed line represents an FDR-adjusted *p* value of 0.05 (*n* = 5).

(M) Enrichment analysis of the Gene Ontology terms shown in sequencing data from PSMB8^{OE} and mScarlet control neurons. Adjusted *p* values and normalized enrichment scores (NESs) are shown.

(N) ROS levels in PSMB5^{OE}, PSMB8^{OE}, or IFNγ^{OE} neurons measured by CellROX in untreated (control) neurons (*n* = 5). Representative images are shown in Figure 2I, left column. A one-way ANOVA ($p < 0.05$) with post hoc Tukey's HSD tests was used for statistical comparison.

(O) Quantification of the neuronal iNOS (turquoise) MFI in the spinal cord VHOTs of late-stage EAE mice (30 days p.i.) treated with vehicle (*n* = 9) or 10 mg kg^{-1} body weight ONX-0914 (*n* = 11) i.p. NeuN marks neurons. Nuclei were visualized with DAPI (yellow). Scale bar, 50 μm.

Unless otherwise stated, unpaired t tests with FDR correction for multiple comparisons were used, and individual data points and means are shown. $^{*}p < 0.05$, $^{**}p < 0.01$, $^{***}p < 0.001$, $^{****}p < 0.0001$.

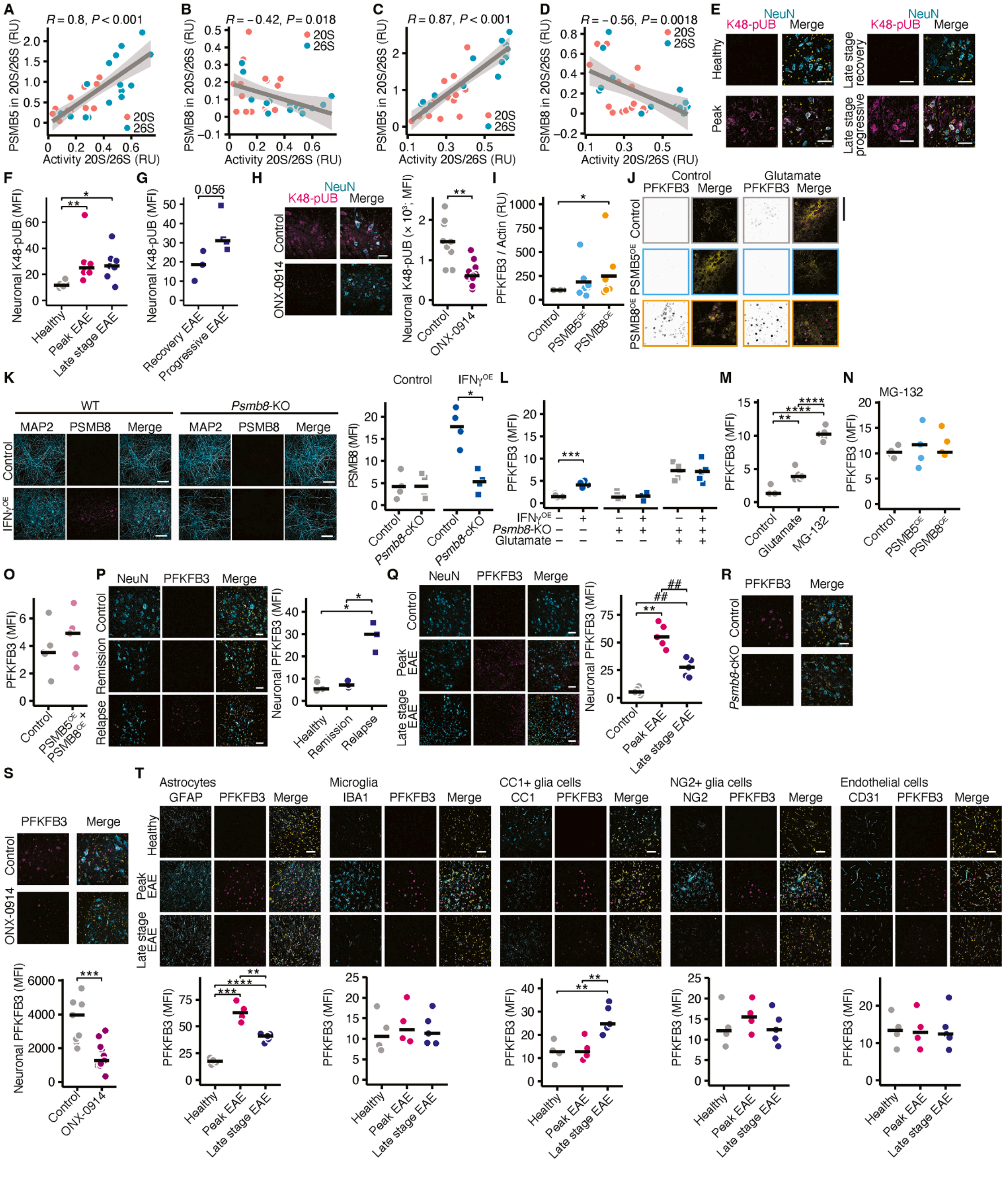

Figure S5. PFKFB3 accumulates in PSMB8-expressing neurons, related to Figure 3

(A and B) Spearman's correlation analysis of the 20S and 26S activity, measured using the β5-specific substrate Suc-LLVY, with PSMB5 (A) or PSMB8 (B) incorporation into the 20S and 26S subunits in neurons that overexpress mScarlet (control), PSMB5 (PSMB5^{OE}), or PSMB8 (PSMB8^{OE}; $n = 5$). The regression line with 95% confidence intervals is shown.

(C and D) Spearman's correlation analysis of 20S and 26S activity, measured using the β5-specific substrate Suc-LLVY, with PSMB5 (C) or PSMB8 (D) incorporation into the 20S and 26S subunits in neurons that overexpress mScarlet control, exposed to 100 ng mL^{-1} IFNγ for 3 or 7 days.

(E–G) K48-poly-ubiquitin (K48-pUB) MFI in NeuN expressing neurons of the spinal cord VHOT in healthy mice ($n = 5$), peak EAE mice (15 days p.i.; $n = 5$), and late-stage EAE mice (30 days p.i.), either pooled ($n = 7$; E and F) or separated by recovery (last score < 2; $n = 3$) or progression (last score > 2; $n = 4$; G). Nuclei were visualized with DAPI (yellow). Scale bar, 50 μm. For (F) a one-way ANOVA ($p < 0.05$) with post hoc Tukey's HSD tests was used for statistical comparison. For (G), an unpaired t test was used.

(H) Neuronal K48-poly-ubiquitin (K48-pUB) MFI in the spinal cord VHOT of late-stage EAE mice (30 days p.i.) treated with vehicle ($n = 9$) or 10 mg kg^{-1} body weight ONX-0914 ($n = 11$) i.p. NeuN stains neurons. Scale bar, 50 μm.

(I) Immunoblot quantification of PFKFB3 in mScarlet control, PSMB5^{OE}, and PSMB8^{OE} neurons ($n = 7$). PFKFB3 levels were normalized to actin, and the data were normalized to the control conditions. A one-way ANOVA ($p < 0.05$) with post hoc Tukey's HSD tests was used for statistical comparison.

(legend continued on next page)

(J) Representative images of PFKFB3 (magenta) protein expression in mScarlet control, PSMB5^{OE}, or PSMB8^{OE} neurons treated with vehicle or 50 μM glutamate for 6 h. The neurons were visualized using actin (yellow). Quantification is shown in Figure 3E. Scale bar, 50 μm.

(K) Representative images of WT and *Psmb8*-KO neuronal cultures that were continuously exposed to IFNγ (IFNγ^{OE}; $n = 4$). Scale bar, 100 μm.

(L) Neuronal PFKB3 MFI in mScarlet control or IFNγ^{OE} WT and *Psmb8*-KO neurons treated with vehicle or 50 μM glutamate for 6 h ($n = 5$).

(M) Neuronal PFKFB3 MFI in neurons treated with 50 μM glutamate for 6 h or 1 μM MG-132 (pan-proteasomal inhibitor) for 24 h ($n = 5$). A one-way ANOVA ($p < 0.05$) with post hoc Tukey's HSD tests were used for statistical comparison.

(N) Comparison of PFKFB3 protein expression in mScarlet control, PSMB5^{OE}, or PSMB8^{OE} neurons treated with 1 μM MG-132 for 24 h ($n = 4$). A one-way ANOVA ($p > 0.05$) was used.

(O) Neuronal PFKFB3 MFI in mScarlet control neurons and neurons that overexpress PSMB5 and PSMB8 simultaneously ($n = 5$).

(P) MFI of neuronal PFKFB3 in the spinal cord VHOT of healthy SJL mice ($n = 6$) and SJL mice with EAE 40 days p.i. with mice that remitted (final score = 0; $n = 3$) or having a relapse (final score > 1; $n = 3$) were separately analyzed. Nuclei were visualized with DAPI (yellow). Scale bar, 50 μm. A one-way ANOVA ($p < 0.05$) with post hoc Tukey's HSD tests was used for statistical comparison.

(Q) Neuronal PFKFB3 MFI in the spinal cord VHOT of healthy Biozzi ABH mice and Biozzi ABH mice subjected to EAE 2 days after disease onset (peak disease) and 20 days after onset of disease progression (late-stage of the disease; $n = 5$). Nuclei were visualized with DAPI (yellow). Scale bar, 50 μm. A one-way ANOVA ($p < 0.05$) with post hoc Tukey's HSD tests was used for statistical comparison. $^{**}p < 0.01$ in Tukey's HSD test, $^{\#\#}p < 0.01$ in unpaired FDR-adjusted t tests.

(R) Representative image of neuronal PFKFB3 staining in the spinal cord VHOT of WT and *Psmb8*-cKO late-stage EAE mice (30 days p.i.). Nuclei were visualized with DAPI (yellow). Scale bar, 50 μm. The quantification is shown in Figure 3H.

(S) MFI of neuronal PFKFB3 in the spinal cord VHOT of late-stage EAE mice (30 days p.i.) treated with a vehicle ($n = 9$) or 10 mg kg^{-1} body weight ONX-0914 ($n = 11$) i.p. Nuclei were visualized with DAPI (yellow). Scale bar, 50 μm.

(T) MFI of PFKFB3 in GFAP+ glia cells (astrocytes), IBA1+ glia cells (microglia), CC1+ glia cells ((pre-)myelinating oligodendrocytes), NG2+ glia cells (oligodendrocyte progenitor cells), and CD31+ cells (endothelial cells) in the spinal cord ventral horns of healthy mice ($n = 5$), peak EAE mice (15 days p.i.; $n = 5$), and late-stage EAE mice (30 days p.i.; $n = 6$). Nuclei were visualized with DAPI (yellow). Scale bar, 50 μm. A one-way ANOVA ($p < 0.05$) with post hoc Tukey's HSD tests was used for statistical comparison.

Unless otherwise stated, unpaired t tests with FDR correction for multiple comparisons were used, and individual data points and means are shown. $^{*}p < 0.05$, $^{**}p < 0.01$, $^{***}p < 0.001$, $^{****}p < 0.0001$.

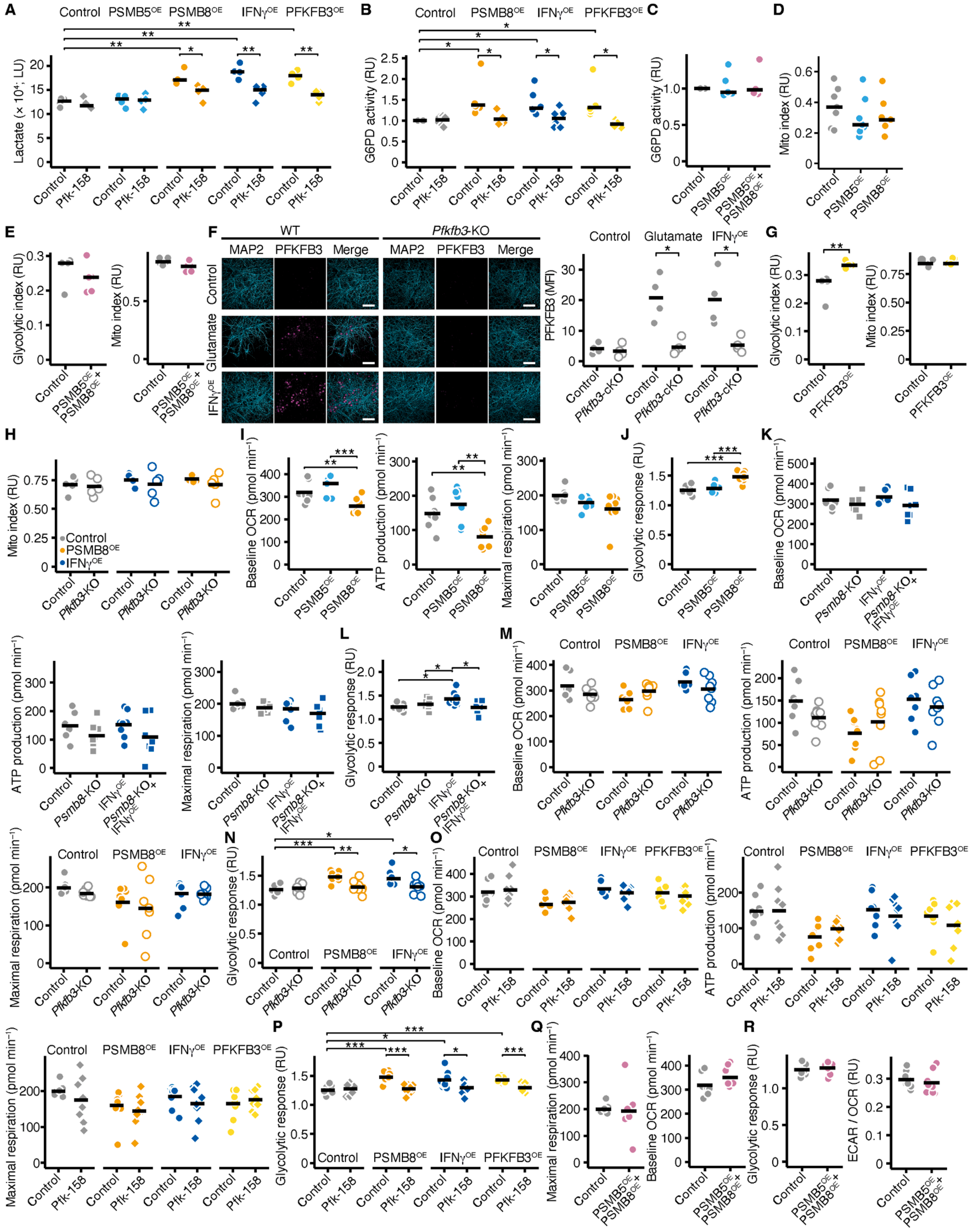

Figure S6. PSMB8 expression increases glycolysis, related to Figure 4

(A) Lactate (LU) in the supernatant of mScarlet control, PSMB5^{OE}, PSMB8^{OE}, PFKFB3-overexpressing neurons (PFFKB3^{OE}), or neurons continuously exposed to IFNγ for 7 days (IFNγ^{OE}) and were treated every other day with 500 nM Pfk-158 (*n* = 4).

(B and C) Glucose-6-phosphate-dehydrogenase (G6PD) activity (RU) in mScarlet control, PSMB5^{OE}, PSMB8^{OE}, PFFKB3^{OE} or neurons continuously exposed to IFNγ for 7 days (IFNγ^{OE}) and were treated every other day with 500 nM Pfk-158 (B; *n* = 6), or neurons overexpressing PSMB5 and PSMB8 simultaneously (C; *n* = 5). Data were normalized to unstimulated mScarlet control neurons. Mann-Whitney U test was used for statistical comparisons.

(D) Mitochondrial ATP production (Mito index) in RU in neurons overexpressing mScarlet control, PSMB5 and PSMB8 (*n* = 7).

(E) Glycolytic (glycolytic index) and mitochondrial (Mito index) ATP production in RU in neurons overexpressing mScarlet control, or PSMB5 and PSMB8 simultaneously (*n* = 5).

(legend continued on next page)

(F) PFKFB3 MFI in WT and *Pfkfb3*-KO neuronal cultures that were exposed to vehicle, 50 μM glutamate for 4 h or continuously exposed to IFNγ for 7 days (IFNγ^{OE}; n = 4). Scale bar, 100 μm.

(G) Glycolytic (glycolytic index) and mitochondrial (Mito index) ATP production in RU in neurons overexpressing mScarlet control, or PFKFB3 (n = 5).

(H) Mitochondrial (Mito index) ATP production in RU in WT and *Pfkfb3*-cKO control mScarlet, PSMB8^{OE} or IFNγ^{OE} neurons (n = 5).

(I) Baseline OCR, ATP production, and maximal respiration in pmol min^{-1} of control mScarlet, PSMB5^{OE}, and PSMB8^{OE} neurons (n = 8). A one-way ANOVA ($p < 0.05$) with post hoc Tukey's HSD tests was used for statistical comparison.

(J) The ratio between ECAR after oligomycin and baseline ECAR as a measure of the glycolytic response in RUs of control mScarlet, PSMB5^{OE}, and PSMB8^{OE} neurons (n = 8). A one-way ANOVA ($p < 0.05$) with post hoc Tukey's HSD tests was used for statistical comparison.

(K) Baseline OCR, ATP production, and maximal respiration in pmol min^{-1} of control mScarlet or IFNγ^{OE} WT and *Psmb8*-KO neurons (n = 8). A one-way ANOVA ($p < 0.05$) with post hoc Tukey's HSD tests was used for statistical comparison.

(L) The ratio between the ECAR after oligomycin and baseline ECAR as a measure of the glycolytic response in RUs of control mScarlet or IFNγ^{OE} WT and *Psmb8*-KO neurons (n = 8). A one-way ANOVA ($p < 0.05$) with post hoc Tukey's HSD tests was used for statistical comparison.

(M) Baseline OCR, ATP production, and maximal respiration in pmol min^{-1} of control mScarlet, PSMB8^{OE}, or IFNγ^{OE} WT and *Pfkfb3*-KO neurons (n = 8).

(N) The ratio between ECAR after oligomycin and baseline ECAR as a measure of the glycolytic response in RUs of control mScarlet, PSMB8^{OE}, or IFNγ^{OE} WT and *Pfkfb3*-KO neurons (n = 8).

(O) Baseline OCR, ATP production, and maximal respiration in pmol min^{-1} of control mScarlet, PSMB8^{OE}, PFKFB3^{OE}, or IFNγ^{OE} neurons that were treated with vehicle or 500 nM Pfk-158 every other day (n = 8).

(P) The ratio between ECAR after oligomycin and baseline ECAR as a measure of the glycolytic response in RUs of control mScarlet, PSMB8^{OE}, PFKFB3^{OE}, or IFNγ^{OE} neurons that were treated with vehicle or 500 nM Pfk-158 every other day (n = 8).

(Q) Baseline OCR and maximal respiration in pmol min^{-1} of control neurons that overexpress mScarlet or both PSMB5 and PSMB8 simultaneously (n = 8).

(R) The ratio between ECAR after oligomycin and baseline ECAR as a measure of the glycolytic response in RUs, and the ratio of ECAR to OCR at baseline in RUs for control neurons that overexpress mScarlet or both PSMB5 and PSMB8 simultaneously (n = 8).

Unless otherwise stated, unpaired t tests with FDR correction for multiple comparisons were used, and individual data points and means are shown. *$p < 0.05$, **$p < 0.01$, ***$p < 0.001$.

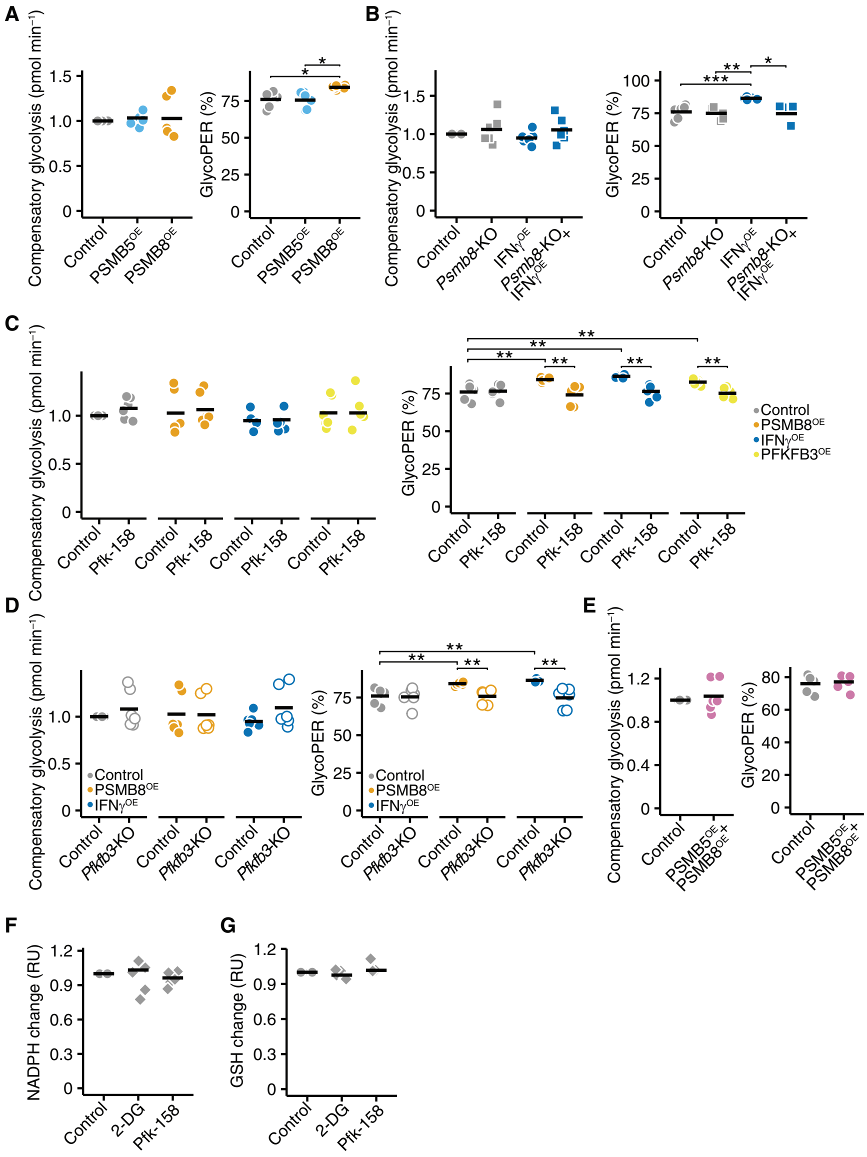

Figure S7. PSMB8 and PFKFB3 inhibition do not change steady-state metabolism, related to Figure 5

(A) Compensatory glycolysis in pmol min^{-1} and the percentage of the glycolytic PER (PER) of total PER (GlycoPER%) in control mScarlet, PSMB5^{OE}, and PSMB8^{OE} neurons ($n = 6$). A one-way ANOVA ($p < 0.05$) with post hoc Tukey's HSD tests was used for statistical comparison.

(B) Compensatory glycolysis in pmol min^{-1} and the percentage of the glycolytic PER (PER) of total PER (GlycoPER%) in control mScarlet or IFNγ^{OE} WT and *Psmb8*-KO neurons ($n = 6$). A one-way ANOVA ($p < 0.05$) with post hoc Tukey's HSD tests was used for statistical comparison.

(C) Compensatory glycolysis in pmol min^{-1} and the percentage of the glycolytic PER (PER) of total PER (GlycoPER%) in control mScarlet, PSMB8^{OE}, PFKFB3^{OE}, or IFNγ^{OE} neurons that were treated with vehicle or 500 nM Pfk-158 every other day ($n = 6$).

(D) Compensatory glycolysis in pmol min^{-1} and the percentage of the glycolytic PER (PER) of total PER (GlycoPER%) in control mScarlet, PSMB8^{OE}, or IFNγ^{OE} WT and *Pfkfb3*-KO neurons ($n = 6$).

(E) Compensatory glycolysis in pmol min^{-1} and the percentage of the glycolytic PER (PER) of total PER (GlycoPER%) in control neurons that overexpress mScarlet or PSMB5 and PSMB8 simultaneously ($n = 6$).

(F) Change in NADPH in RUs in neurons that were treated with vehicle, 2 mM 2-DG or 500 nM Pfk-158 every other day ($n = 6$). The data were normalized to the vehicle-treated controls. A one-way ANOVA ($p > 0.05$) was performed.

(G) Change in GSH in RUs in neurons that were treated with vehicle, 2 mM 2-DG, or 500 nM Pfk-158 every other day ($n = 6$). The data were normalized to the vehicle-treated controls. A one-way ANOVA ($p > 0.05$) was performed.

Unless otherwise stated, unpaired t tests with FDR correction for multiple comparisons were used, and individual data points and means are shown. *$p < 0.05$, **$p < 0.01$, ***$p < 0.001$.

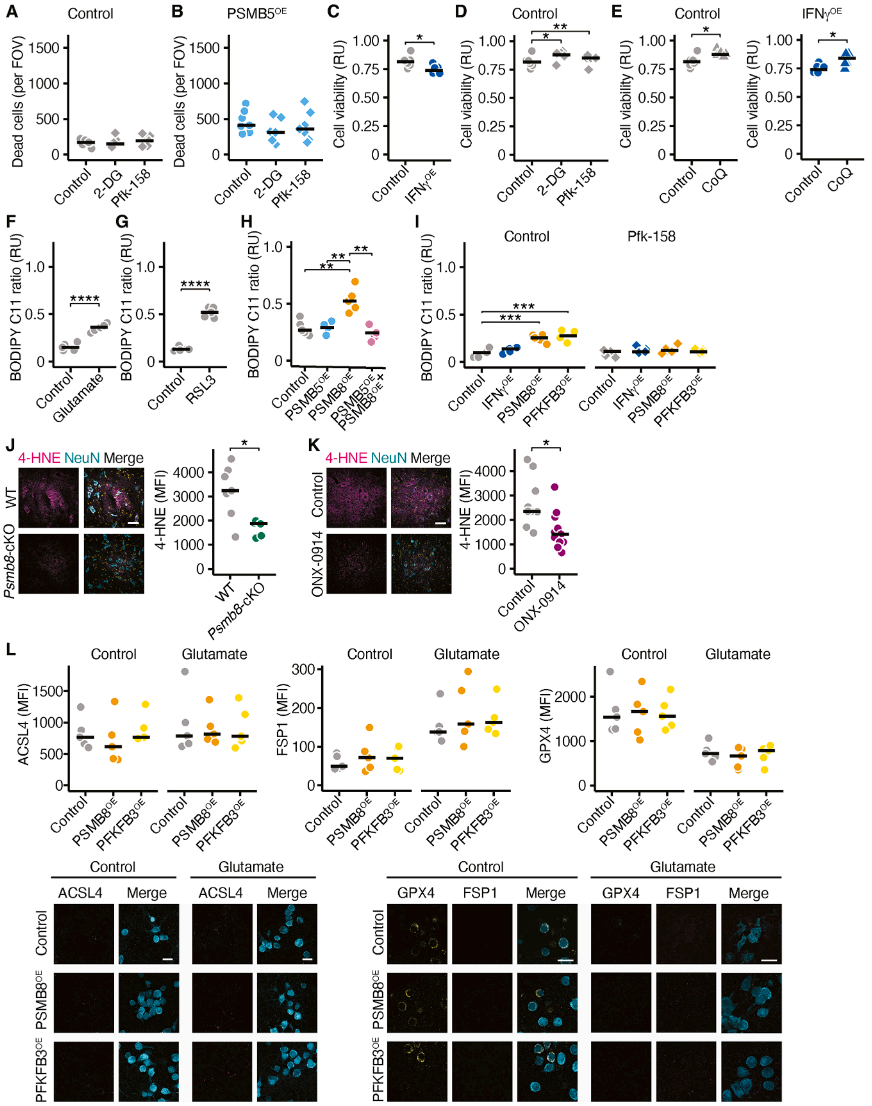

Figure S8. Neuronal *Psmb8* deletion protects from lipid peroxidation in EAE, related to Figure 6

(A and B) Number of dead cells per field of view (FOV) of neuronal mScarlet control (A) and PSMB5-overexpressing (PSMB5^{OE}; B) neurons 14 days post-transfection, treated with vehicle, 2 mM 2-DG, or 500 nM Pfk-158 every other day ($n = 6$). A one-way ANOVA ($p > 0.05$) was used.

(C) Cell viability (RU) of mScarlet control neurons and neurons continuously exposed to IFNγ (IFNγ^{OE}), treated with 50 μM glutamate for 15 h ($n = 6$). Paired t test was performed.

(D) Cell viability of neurons treated with 2 mM 2-DG or 500 nM Pfk-158 and exposed to 50 μM glutamate for 15 h ($n = 6$). Paired t test was performed.

(E) Cell viability of mScarlet control and IFNγ^{OE} neurons treated with 6 μM co-enzyme Q10 (CoQ) and exposed to 50 μM glutamate for 15 h ($n = 6$). Paired t test was performed.

(F and G) Lipid peroxidation quantified by the BODIPY C11 ratio (RU) in neurons exposed to 50 μM glutamate or 6 μM RSL3 for 10 h ($n = 5$).

(H) BODIPY C11 ratio in mScarlet control, PSMB5^{OE}, PSMB8-overexpressing (PSMB8^{OE}) neurons, or neurons that overexpress PSMB5 and PSMB8 simultaneously ($n = 5$). A one-way ANOVA ($p < 0.05$) with post hoc Tukey's HSD tests was used for statistical comparison.

(I) BODIPY C11 ratio in mScarlet control, PSMB5^{OE}, PSMB8^{OE}, and PFKFB3-overexpressing (PFKFB3^{OE}) neurons treated with vehicle (control, round symbols) or 500 nM Pfk-158 (diamond symbols) every other day ($n = 5$). A one-way ANOVA ($p < 0.05$) with post hoc Tukey's HSD tests was used for statistical comparison.

(J) Neuronal 4-HNE MFI in the spinal cord VHOT of WT ($n = 7$) and *Psmsb8*-cKO ($n = 5$) late-stage EAE mice (30 days p.i.). NeuN marks neurons. Scale bar, 50 μm.

(K) Neuronal 4-HNE MFI in the spinal cord VHOT of late-stage EAE mice (30 days p.i.) treated with vehicle ($n = 9$) or 10 mg kg^{-1} body weight ONX-0914 ($n = 11$) i.p. NeuN marks neurons. Scale bar, 50 μm.

(L) Neuronal MFI of ferroptosis regulators ACSL4, FSP1, and GPX4 in PSMB8^{OE} and PFKFB3^{OE} neurons at steady state and 6 h after 50 μM glutamate stimulation ($n = 5$). Scale bar, 20 μm. A one-way ANOVA ($p > 0.05$) was used.

Unless otherwise stated, unpaired t tests with FDR correction for multiple comparisons were used, and individual data points and means are shown. *$p < 0.05$, **$p < 0.01$, ****$p < 0.0001$.

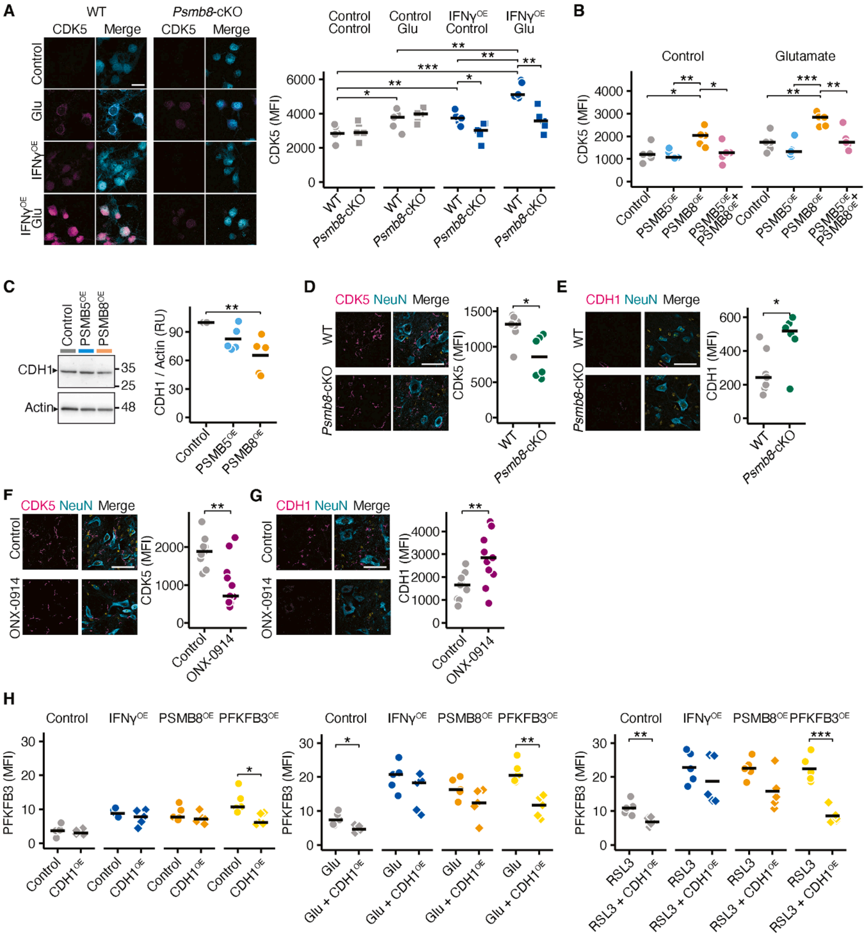

Figure S9. The CDK5/CDH1 axis is modulated by the proteasomal switch in neurons, related to Figure 6

(A) CDK5 MFI in mScarlet control neurons and neurons continuously exposed to IFNγ for 7 days (IFNγ^{OE}) with or without genetic *Psmb8* deletion, treated with either vehicle or 50 μM glutamate for 6 h ($n = 5$). Neurons were visualized by NeuN staining. Scale bar, 20 μm.

(B) CDK5 MFI in mScarlet control, PSMB5-overexpressing (PSMB5^{OE}), PSMB8-overexpressing (PSMB8^{OE}) neurons, or neurons overexpressing both PSMB5 and PSMB8 simultaneously, treated with vehicle or 50 μM glutamate for 6 h ($n = 5$). A one-way ANOVA ($p < 0.05$) with post hoc Tukey's HSD tests was used for statistical comparison.

(C) Representative immunoblot of CDH1 and actin in mScarlet control, PSMB5^{OE}, and PSMB8^{OE} neurons ($n = 5$). Data were normalized to controls. The Mann-Whitney U test was used.

(D) Neuronal CDK5 MFI in the spinal cord VHOT of WT ($n = 7$) and *Psmsb8*-cKO ($n = 6$) late-stage EAE mice (30 days p.i.). NeuN marks neurons. Scale bar, 50 μm.

(E) Neuronal CDH1 MFI in the spinal cord VHOT of WT ($n = 7$) and *Psmsb8*-cKO ($n = 6$) late-stage EAE mice (30 days p.i.). NeuN marks neurons. Scale bar, 50 μm.

(F) Neuronal CDK5 MFI in the spinal cord VHOT of late-stage EAE mice (30 days p.i.) treated with vehicle ($n = 9$) or 10 mg kg^{-1} body weight ONX-0914 ($n = 11$) i.p. NeuN marks neurons. Scale bar, 50 μm.

(G) Neuronal CDH1 MFI in the spinal cord VHOT of late-stage EAE mice (30 days p.i.) treated with vehicle ($n = 9$) or 10 mg kg^{-1} body weight ONX-0914 ($n = 11$) i.p.. NeuN marks neurons. Scale bar, 50 μm.

(H) PFKFB3 MFI in mScarlet control neurons, IFNγ^{OE} neurons, PSMB8^{OE} neurons, and neurons overexpressing PFKFB3 (PFKFB3^{OE}). If indicated, they also overexpressed CDH1 (CDH1^{OE}, diamond symbols) and were exposed to vehicle, 50 μM glutamate, or 6 μM RSL3 for 6 h ($n = 5$).

Unless otherwise stated, unpaired t tests with FDR correction for multiple comparisons were used, and individual data points and means are shown. *$p < 0.05$, **$p < 0.01$, ***$p < 0.001$.

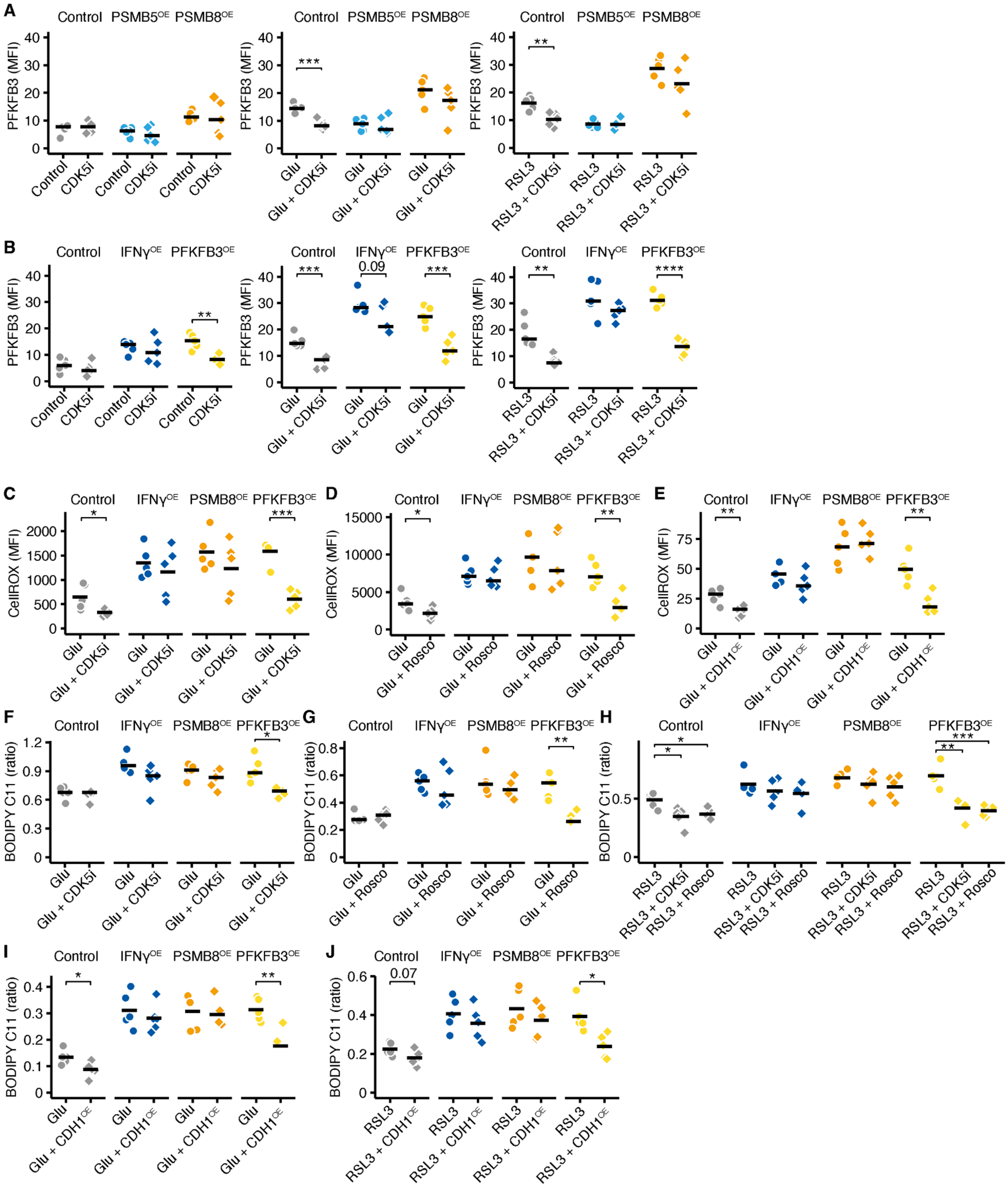

Figure S10. PSMB8-dependent PFKFB3 accumulation is independent of CDK5 and CDH1, related to Figure 6

(A) PFKFB3 MFI in mScarlet control, PSMB5-overexpressing (PSMB5^{OE}) and PSMB8-overexpressing (PSMB8^{OE}) neurons treated with vehicle or 50 nM CDK5 inhibitor 20-223 (CDK5i) and subsequently with either vehicle, 50 μM glutamate, or 6 μM RSL3 for 6 h (*n* = 5).

(B) PFKFB3 MFI in mScarlet control, PFKFB3-overexpressing (PFKFB3^{OE}) neurons, or neurons continuously exposed to IFNγ (IFNγ^{OE}), treated with vehicle or 50 nM CDK5 inhibitor 20-223 (CDK5i) and subsequently with either vehicle, 50 μM glutamate or 6 μM RSL3 for 6 h (*n* = 5).

(C–E) ROS measured by CellROX MFI in mScarlet control, IFNγ^{OE}, PSMB8^{OE}, and PFKFB3^{OE} neurons treated with 50 nM CDK5i (C), 1 μM roscovitine (rosco; D), or additional CDH1 overexpression (E; CDH1^{OE}) and subsequently with either vehicle or 50 μM glutamate for 2 h (*n* = 5).

(F–H) Lipid peroxidation measured by the BODIPY C11 ratio in mScarlet control, IFNγ^{OE}, PSMB8^{OE}, and PFKFB3^{OE} neurons exposed to 50 nM CDK5i and 50 μM glutamate for 8 h (F), 1 μM roscovitine (Rosco) and 50 μM glutamate for 8 h (G), or 6 μM RSL3 for 8 h (H; *n* = 5). For (H) a one-way ANOVA ($p < 0.05$) with post hoc Tukey's HSD tests was used for statistical comparison.

(legend continued on next page)

(I and J) Lipid peroxidation measured by the BODIPY C11 ratio in mScarlet control, IFNγ^{OE}, PSMB8^{OE}, and PFKFB3^{OE} neurons with additional CDH1 overexpression (CDH1^{OE}) and exposed to 50 μM glutamate for 8 h (I) or 6 μM RSL3 for 8 h (J; $n = 5$).

Unless otherwise stated, unpaired t tests with FDR correction for multiple comparisons were used, and individual data points and means are shown. *$p < 0.05$, **$p < 0.01$, ***$p < 0.001$, ****$p < 0.0001$.

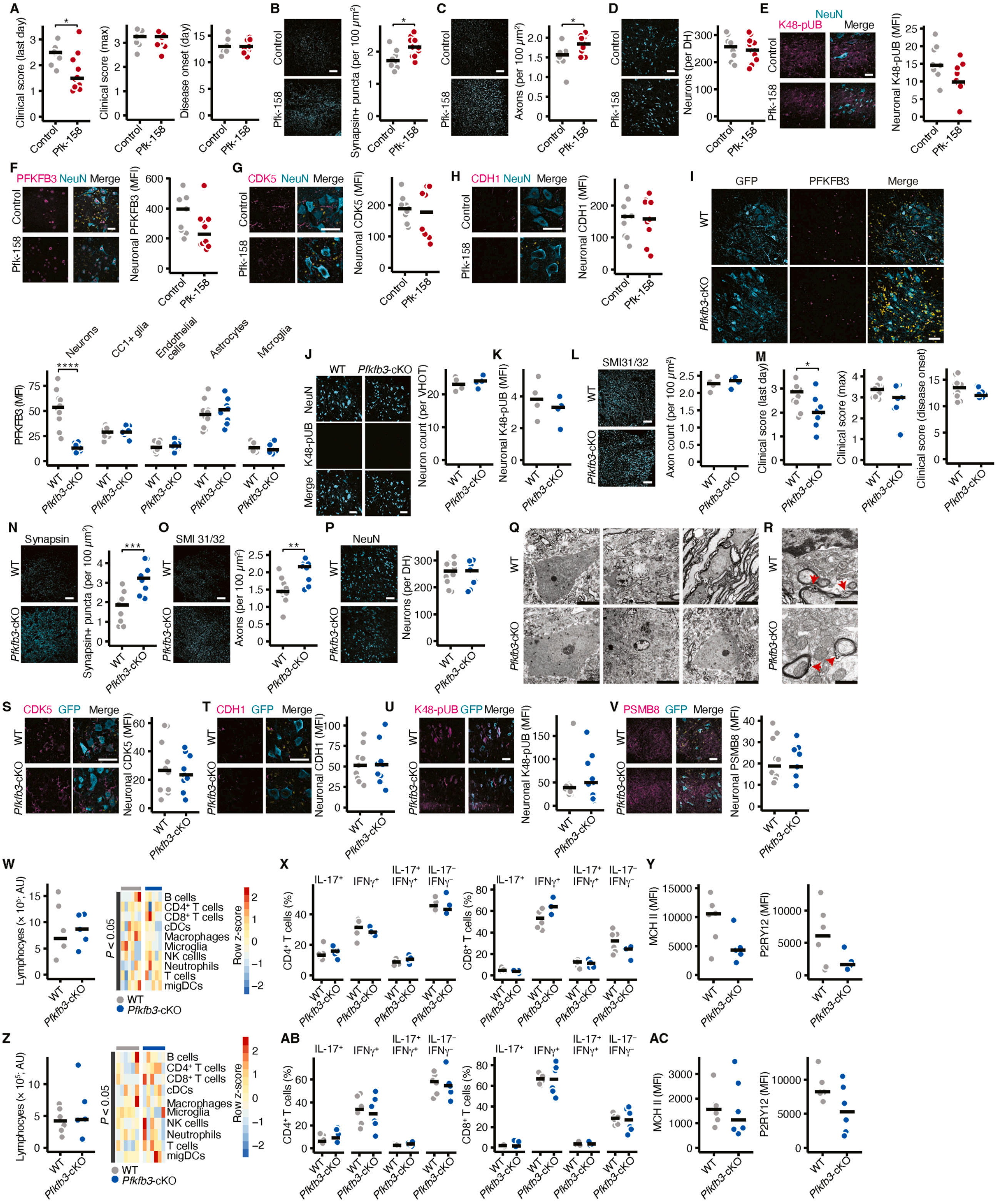

Figure S11. PFKFB3 inhibition does not alter aberrant proteostasis in EAE, related to Figure 7

(A) Clinical score on the last day, maximal disease score, and day of disease onset of EAE mice treated daily with vehicle ($n = 9$) or 12 mg kg^{-1} body weight Pfk-158 ($n = 11$) i.p., starting at the acute EAE stage (14 days p.i.).

(legend continued on next page)

(B–D) Synapsin+ puncta per 100 μm^2 (B) in the spinal cord VHOT, axonal counts per 100 μm^2 in the dorsal columns (C), and neuronal counts in the dorsal horns (D) of late-stage EAE mice (30 days p.i.) treated with vehicle (n = 9) or 12 mg kg^{-1} body weight Pfk-158 (n = 11). Scale bar, 50 μm.

(E–H) Neuronal MFI of K48-poly-ubiquitin (K48-pUB; E), PFKFB3 (F), CDK5 (G), and CDH1 (H) in the spinal cord VHOT of late-stage EAE mice (30 days p.i.) treated with vehicle (n = 9) or 12 mg kg^{-1} body weight Pfk-158 (n = 10) i.p. NeuN marks neurons. Nuclei were visualized with DAPI (yellow). Scale bar, 50 μm.

(I) LSL-Cas9 mice were injected with AAV-PHP.eB expressing a non-targeted control guide or *Pfkfb3*-targeting guides (*Pfkfb3*-cKO) along the Cre recombinase under the control of the neuron-specific human synapsin promoter. MFI of PFKFB3 was measured in neurons, CC1+ (pre-)myelinating oligodendrocytes, endothelial cells, astrocytes, and microglia in the spinal cord VHOT of WT (n = 9), and *Pfkfb3*-cKO mice (n = 8) during late-stage EAE (30 days p.i.). Scale bar, 50 μm. GFP-positive cells carry the Cre recombinase.

(J–L) Neuron count (J), neuronal K48-poly-ubiquitin (K48-pUB; K) levels in spinal cord VHOT neurons, and axonal counts in the dorsal columns (L) of WT (n = 4) and *Pfkfb3*-cKO (n = 4) mice. Scale bar, 50 μm.

(M) Clinical score on the last day, maximal disease score, day of disease onset of WT (n = 10) and *Pfkfb3*-cKO (n = 9) EAE mice.

(N–P) Synapsin+ puncta per 100 μm^2 (N) in the spinal cord VHOT, axonal counts per 100 μm^2 in the dorsal columns (O), and neuronal counts in the dorsal horns (P) of WT (n = 9) and *Pfkfb3*-cKO (n = 9) late-stage EAE mice (30 days p.i.). Scale bar, 50 μm.

(Q and R) Overview (Q) transmission electron microscopy images of spinal cord neurons from WT (n = 3) and *Pfkfb3*-cKO mice (n = 3) mice during peak EAE (15 days p.i.). Higher magnification of axons with myelin sheaths are shown and highlighted by arrows (R). Scale bar, 10 μm (Q) and 1 μm (R).

(S–V) Neuronal MFI of CDK5 (S), CDH1 (T), K48-pUB (U), and PSMB8 (V) in the spinal cord VHOT of WT (n = 10) and *Pfkfb3*-cKO (n = 9) late-stage EAE mice (30 days p.i.). Nuclei were visualized with DAPI (yellow). Scale bar, 50 μm. GFP was visualized to show transduced neurons.

(W) Absolute number of CNS-infiltrating lymphocytes and heatmap representation of the percentage of indicated immune cell populations among all lymphocytes in WT (n = 6) and *Pfkfb3*-cKO (n = 5) peak EAE mice (15 days p.i.).

(X) Percentage of IL-17$^+$, IFNγ$^+$, IL17$^+$IFNγ$^+$, and IL17$^-$IFNγ$^-$ CD4+ T cells and CD8+ T cells in WT (n = 6) and *Pfkfb3*-cKO (n = 5) peak EAE mice (15 days p.i.).

(Y) MFI of MHC class II and P2RY12 in microglia of WT (n = 6) and *Pfkfb3*-cKO (n = 5) peak EAE mice (15 days p.i.).

(Z) Absolute number of CNS-infiltrating lymphocytes and heatmap representation of the percentage of indicated immune cell populations among all lymphocytes in WT (n = 6) and *Pfkfb3*-cKO (n = 6) late-stage EAE mice (30 days p.i.).

(AB) Percentage of IL-17$^+$, IFNγ$^+$, IL17$^+$IFNγ$^+$, and IL17$^-$IFNγ$^-$ CD4+ T cells and CD8+ T cells in WT (n = 6) and *Pfkfb3*-cKO (n = 6) late-stage EAE mice (30 days p.i.).

(AC) MFI of MHC class II and P2RY12 in microglia of WT (n = 6) and *Pfkfb3*-cKO (n = 6) late-stage EAE mice (30 days p.i.).

Unless otherwise stated, unpaired t tests with FDR correction for multiple comparisons were used, and individual data points and means are shown. *p < 0.05, **p < 0.01, ***p < 0.001, ****p < 0.0001.

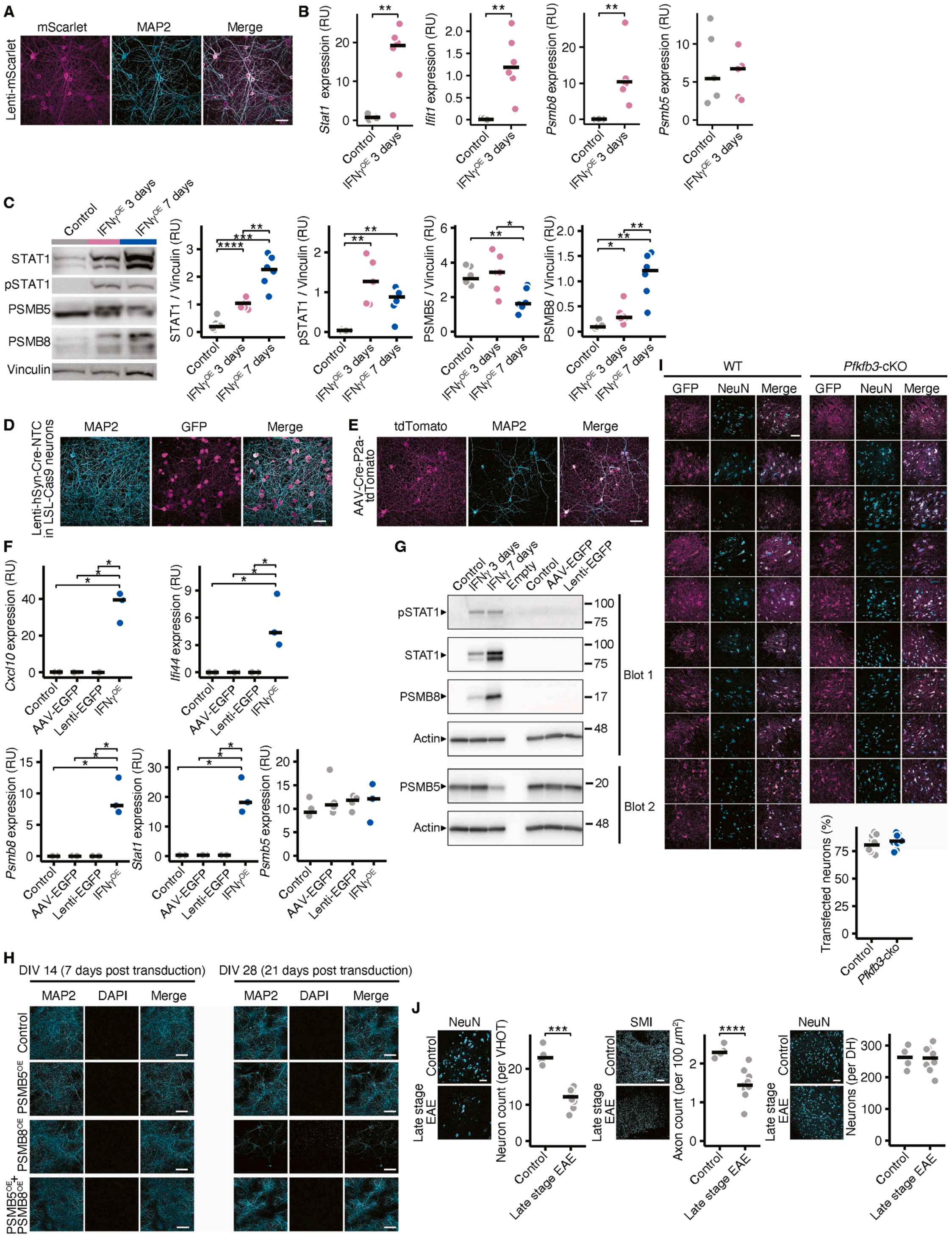

Figure S12. AAV and lentivirus transductions do not elicit a type II IFN response in neuronal cultures, related to Figures 1, 2, 3, 4, 5, 6, 7, and S1–S12

(A) Representative image of neuronal cultures transduced with a lentivirus carrying mScarlet under the control of a human synapsin promoter. MAP2 stains neurons. Scale bar, 50 µm.

(B) mRNA expression of *Stat1*, *Ifit1*, *Psmb8*, and *Psmb5* in control neurons and neurons 3 days after transduction with an IFNγ overexpression construct (*n* = 4).

(C) Immunoblot analyses of STAT1, pSTAT1, PSMB5, and PSMB8 in control neurons and in neurons 3 and 7 days after transduction with an IFNγ overexpression construct (*n* = 6). Vinculin was used as loading control.

(legend continued on next page)

(D) Representative image of neuronal cultures from LSL-Cas9 mice transduced with a lentivirus carrying Cre recombinase under the human synapsin promoter and a non-targeting control (NTC) guide. The GFP signal indicates transduced cells. MAP2 stains neurons. Scale bar, 50 μm.

(E) Representative image of neuronal cultures transduced with an AAV carrying Cre recombinase and tdTomato under the control of a human synapsin promoter. MAP2 stains neurons. Scale bar, 50 μm.

(F) mRNA expression of *Cxcl10*, *Ifi44*, *Psmb8*, *Stat1*, and *Psmb5* in neurons that were untreated or transduced with a lentivirus or AAV carrying mScarlet, as well as in neurons continuously exposed to IFNγ as a positive control ($\mathrm{IFN}\gamma^{\mathrm{OE}}$; $n = 4$). A one-way ANOVA ($p < 0.05$) with post hoc Tukey's HSD tests was used for statistical comparison.

(G) Representative immunoblot of STAT1, pSTAT1, PSMB8, PSMB5, and actin in control neurons and in neurons transduced with an EGFP-carrying AAV or lentivirus, as well as neurons exposed to 100 ng mL^{-1} IFNγ for 3 days or 7 days as a positive control.

(H) Representative images of neurons overexpressing control mScarlet, PSMB5, PSMB8, or simultaneously PSMB5 and PSMB8 for 7 days after transduction (14 days *in vitro*) and for 21 days after transduction (28 days *in vitro*). 5 μM DAPI was applied to the neuronal cultures for 10 min before PFA fixation. MAP2 stains neurons. Scale bar, 100 μm. The quantification is shown in Figure 2C.

(I) Representative images and quantification of the spinal cord ventral horns of all WT ($n = 10$) and *Pfkfb3*-cKO ($n = 9$) mice used for the phenotype EAE analysis shown in Figure 7. Each row represents a mouse. NeuN stains neurons, and GFP expression indicates transduced cells. Scale bar, 50 μm.

(J) Quantification of neuronal cells in the spinal cord VHOTs (A), axonal counts per 100 $\mu\mathrm{m}^2$ in the dorsal columns (B) and neuronal cells in the dorsal horn (C) of healthy ($n = 4$) and late-stage EAE mice (30 days p.i.; $n = 8$). Scale bar, 50 μm.

Unless otherwise stated, unpaired t tests with FDR correction for multiple comparisons were used, and individual data points and means are shown. *$p < 0.05$, **$p < 0.01$, ***$p < 0.001$, ****$p < 0.0001$.